INVESTIGATION OF HIGH-PRESSURE METHANE AND SYNGAS AUTOIGNITION DELAY TIMES

A Dissertation
Presented to
The Academic Faculty

by

Miad Karimi

In Partial Fulfillment
of the Requirements for the Degree
Doctor of Philosophy in the
School of Aerospace Engineering

Georgia Institute of Technology
December 2019

INVESTIGATION OF HIGH-PRESSURE METHANE AND SYNGAS AUTOIGNITION DELAY TIMES

Approved by:

Professor Devesh Ranjan, Advisor
School of Mechanical Engineering
Georgia Institute of Technology

Professor Timothy Lieuwen
School of Aerospace Engineering
Georgia Institute of Technology

Professor Wenting Sun, Advisor
School of Aerospace Engineering
Georgia Institute of Technology

Professor Peter Loutzenhiser
School of Mechanical Engineering
Georgia Institute of Technology

Professor Suresh Menon
School of Aerospace Engineering
Georgia Institute of Technology

Date Approved: August 15, 2019

ACKNOWLEDGEMENTS

I would like to thank the people without whose help this thesis would not have been written. I am very grateful for having the opportunity to learn many things from my dear friends and colleagues Bradley Ochs, Prof. David Scarborough, Chris Ballance, Seth Hutchins, Shane Getchell, Henry Russell, Dr. Farzad Poursadegh, Zefang Liu, Dr. Xiang Gao, and Michael Lynch. Their willingness to help, their generosity and their support throughout these years have been exceptional.

I would like to thank my committee members for their constructive feedbacks during my thesis proposal, which helped me improve my dissertation. I am also very pleased that I had the opportunity to work with Professor Devesh Ranjan and Professor Wenting Sun as my advisors. Their support and availability throughout my graduate studies always encouraged me to advance in my field. I am very thankful for the resources they provided through the years to facilitate my research progress. Lastly, I am honored to have gained their trust to assemble and operate a vigorous and state-of-the-art high-pressure shock tube facility.

I would like to acknowledge my parents, my sister and my lovely fiancé, Irina, for all their supports and patience throughout tough moments of my studies. I appreciate all they did for me and all their emotional support. I would also like to send many thanks to my dear uncle, Prof. Mohsen Karimi, and his family without whom I would not have had the opportunity to pursue my degrees at Georgia Tech.

TABLE OF CONTENTS

LIST OF TABLES

LIST OF FIGURES

SUMMARY

This thesis reports methane (CH_4) and a syngas mixture (H_2/CO=95:5) autoignition delay measurements relevant to operating conditions of supercritical carbon dioxide (sCO_2) power cycle (100 to 300 bar) combustors. To acquire data at these conditions as part of this thesis, a new high-pressure shock tube is designed, fabricated and commissioned. The experiments are conducted for diluted carbon dioxide environments at 100 and 200 bar and at temperatures within the range of approximately 1100–1400 K. To investigate the chemical effect of CO_2 at supercritical conditions, experiments are conducted at similar pressures and temperatures by substituting CO_2 with an inert bath gas, Ar (argon). Obtaining ignition delay times in Ar bath gas allows to systematically study the chemical effect of CO_2 on ignition chemistry.

Methane ignition delay times are compared to several chemical kinetic models, such as Aramco 2.0, FFCM-1, HP-Mech, USC Mech II and GRI 3.0. For the conditions of this study, predictions of the Aramco 2.0 kinetic model show the overall best agreement with experimental measurements. Following the experimental data, brute-force sensitivity analyses and reaction pathway flux analyses are utilized to gain insight into details of the ignition chemistry of the fuels (CH_4 and H_2/CO=95:5). These analyses indicate that methyl (CH_3) recombination to form ethane (C_2H_6) and oxidation of CH_3 to form methoxide (CH_3O) are the most important reactions controlling the ignition behavior of methane at temperatures greater than approximately 1250 K. However, at temperatures below approximately 1250 K, an additional reaction pathway for methyl radicals is found through $CH_3+O_2+M=CH_3O_2+M$, which leads to formation of methyldioxidanyl (CH_3O_2). This

reaction pathway plays a distinct role in dictating the ignition trends at lower temperature conditions. Replacing CO_2 with argon as the bath gas reveals that CO_2 does not have major effects on ignition chemistry of CH_4.

A similar approach is taken to obtain experimental data at 100 bar and 200 bar for a syngas fuel mixture of 95% H_2 (hydrogen) and 5% CO (carbon monoxide) in CO_2 and Ar bath gasses. Aramco 2.0 kinetic model, FFCM-1 kinetic model, HP-Mech and USC Mech II show good agreement with the measured ignition delay times. Detailed sensitivity analyses of these kinetic models highlight the importance of the third-body reaction between hydrogen atoms (H) and oxygen molecules (O_2) through $H+O_2+M=HO_2+M$ to form hydroperoxyl (HO_2). In both cases, irrespective of the diluents, this reaction is the most influential reaction to hinder ignition. Ignition delay times obtained from both mixtures not only show a similar trend, but also the same magnitude when compared to the CO_2 mixture. While this observation may suggest that CO_2 has no chemical effect on ignition chemistry, it is found to play a counterbalancing role on syngas ignition at the elevated pressures and temperatures of this study. CO_2 increases the OH (hydroxyl) radical production by colliding with hydrogen peroxide (H_2O_2) through $H_2O_2+M=OH+OH+M$. However, it reduces OH production through $HO_2+H=OH+OH$ due to a lower amount of H radical production compared to the Ar mixture. Therefore, these two effects cancel out the change of OH productions, and CO_2 does not change the ignition delay time of the syngas mixture considered in this study upon comparison with the mixture with Ar bath gas.

CHAPTER 1. Introduction

1.1 Overview

The United States gets the majority of its total energy from oil, coal, and natural gas, all of which are fossil fuels [1]. While the electricity demand is growing, natural gas remains the main source of power production. Projections for natural gas consumption and production show a dramatic increase: greater than 100 billion cubic feet per day till 2050 [2]. Moreover, on statistical basis, two-third of the total U.S. electricity is generated by combusting fossil fuels where natural gas resources contribute approximately 30% to this amount [3]. Therefore, natural gas-fired gas turbines remain one of the crucial components of future power generation. However, emissions from these combustion processes pose climate and environmental concerns. One of the main concerns is global warming as the excessive greenhouse gas production causes heat to be trapped in the atmosphere due to absorption of infrared radiation by these gasses. Such climate change could influence the ecosystems, agriculture, forest growth and human health [4]. The increasing need for power generation and disproportionate human industrial activities could be named as main contributors to the greenhouse gas production. The U.S. Environmental Protection Agency (EPA) reports that 28% of total emissions is produced by the electric power as shown in Figure 1.1 [3].

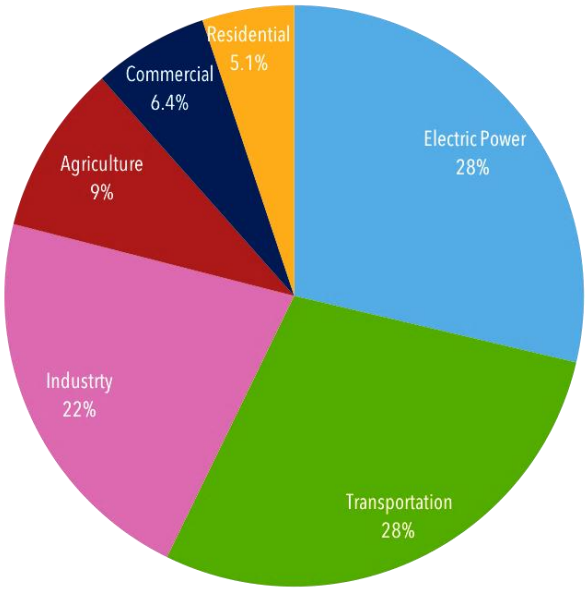

Figure 1.1. The United States emissions divided by sectors [3]

Although carbon dioxide (CO_2), methane (CH_4) and nitrous oxide (N_2O) already exist in the atmosphere, however the industrial activities has largely subsidized to dramatic increase in the concentrations of these species. The formation of carbon dioxide and nitrogen oxides (NO_x) is particularly important as they are principal byproducts of fossil fuel combustion and are considered pollutants. A large amount of CO_2 is produced due to carbon being the main constituents of such fuels (60–90 percent of the total mass [5]). As reported by the EPA, from 1990 to 2017 the total emissions of carbon dioxide has increased by 149.6 million metric tons and in 2017 the majority of the greenhouse gasses was composed of CO_2 as shown in Figure 1.2 [6].

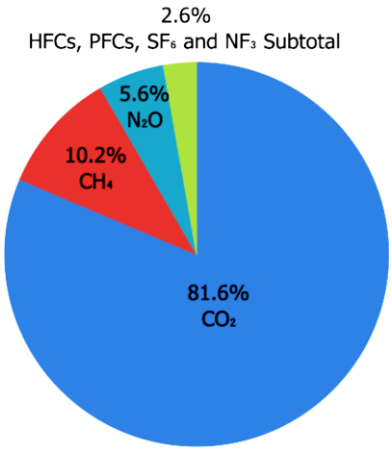

Figure 1.2. The U.S. greenhouse gas emissions (based on million metric tons) [6]

As this number has been rising over decades due to growing demand in electric power, government has passed many strict acts in order to suppress emission levels. Therefore, it is crucial to investigate the possibilities of reducing emissions and reevaluate the conventional ways of electricity generation. Some of the conventional ways for energy generations could be listed as gas turbine cycles (Brayton cycle), steam turbine (Rankine cycles) or a combined cycle which is the combination of these two cycles [7, 8]. The combined cycle power plants have been in operation for more than seven decades and their efficiencies have improved (up to 60%) with advancement in technologies related to material and combustion sciences [7]. The principle of operation of Brayton cycle is fairly simple and could be ideally divided into isobaric and isentropic processes. The isobaric processes occur during the thermal energy addition process through combustion and where heat is rejected; while the isentropic process takes place during the compression and during expansion (output work to generator) [7, 9].

While the gas turbines could run on variety of fuels such as methane, natural gas, biomass gases and diesel fuels [7], the Rankine cycles generate electricity by using natural gas, oil and coal [10]. The working fluid in Rankine cycle is steam or water where the superheated steam is generated by utilizing a boiler. Ideally, the compressed water from the feed pump isentropically enters the boiler where heat is added and the heated vapor leaved the boiler. The superheated vapor then passes through the turbine and isentropically expanded to generate work.

Although there are advantageous and disadvantages associated with each cycle on its own, the combined Brayton-Rankine cycle (combined cycle power plants) is proven to be a promising proposal. Figure 1.3 shows the schematic of such cycle where nearly 40% of the total power is generated by the gas turbine (Brayton cycle) output and approximately 20% of the power is outputted by the steam turbine (Rankine cycle) output [7]. Having the overall efficiency as high as 60% in power generation, reduced NO_x emission due to steam injection [7, 8] and high availability and reliability rates could be listed as some of the advantageous of this cycle. However, there are still considerable disadvantageous associated with these power cycles. Aside from large infrastructures required for operation, the electricity generated from a natural-gas-fired combined cycle unit for instance, could yield to approximately 60% of CO_2 emissions per kilowatt-hour of electricity [11].

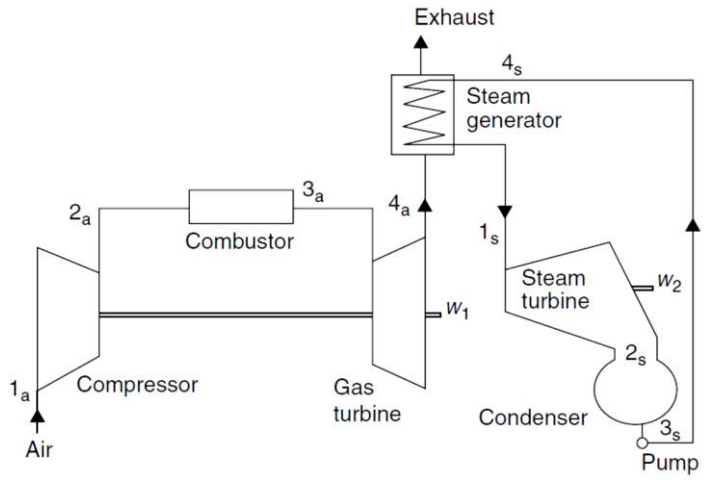

Figure 1.3. Schematic of combined Brayton-Rankine cycle [7]

In recent years several researchers have looked at the alternative ways for combustion process in regards to the electric power generation applications, and even at the possibility of new power cycles. The main targets for investigating the alternative combustion process are reducing NO_x and its surrogates, capturing and storing carbon and possibly scaling down the necessary infrastructures. The Carbon Capture and Storage (CCS) technology is expected to capture up to 90% of the CO_2 produced from fossil fuel combustion in electricity generation [12]. The CCS could be divided into three main categories [12, 13] as shown in Figure 1.4.

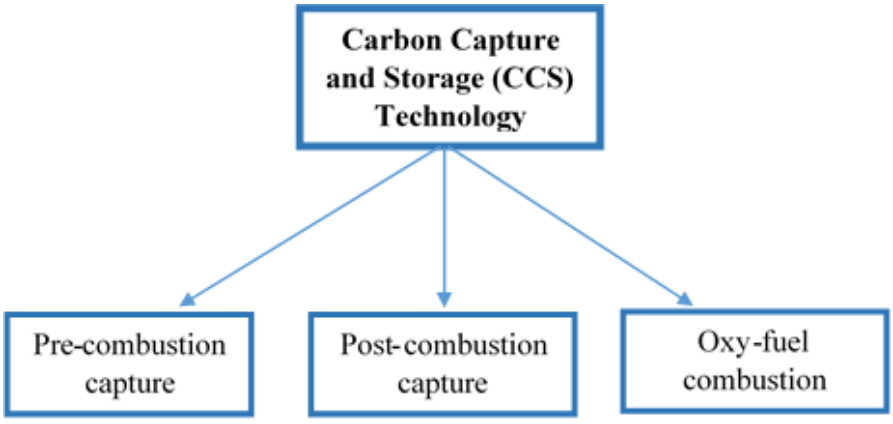

Figure 1.4. Classifications of Carbon Capture and Storage (CCS) technology

In pre-combustion capture technique, the decarbonation of the fuel (gaseous, liquid or solid) occurs through gasification or reformation where the CO_2 and hydrogen (H_2) are separated prior to power and heat generation [12, 13]. Contrary to the pre-combustion process, post-combustion capture technique CO_2 is captured and removed from the exhaust of a combustor prior to its release to atmosphere [13]. This is achieved by having CO_2 absorption in a solvent where it is subsequently released and separated for storage and transportation purposes [12]. In Oxy-fuel combustion technique, the oxygen is separated from air by utilizing an Air Separation Unit (ASU) prior to feeding into the combustor. The advantage of doing so is that the gaseous combustion products are near-pure CO_2 and water (H_2O), therefore the purification of CO_2 is rather simple [12, 13]. The steam generated from oxy-combustion process could be used to derive the turbine for power generation. The CO_2 and H_2O generated by the combustion process could either be recirculated to the combustion cycle for controlling the temperature or they could be captured and stored.

Out of the three techniques mentioned above, the Oxy-fuel combustion has received a substantial attention due to some special properties of CO_2. The abundancy, low cost, stability, non-toxicity and well-known thermodynamics properties of CO_2 could be listed as some of advantageous of using this species [9, 14] in power cycles. Moreover, when compared to air, nitrogen and helium, CO_2 exhibits interesting behavior when used as the working fluid. For instance, near its critical point (304.18 K, 73.80 bar [15]), CO_2 shows a dramatic increase in density and specific heat over a small range of temperature and pressure changes. Figure 1.5 and Figure 1.6 show the variations of density and specific heat at constant pressure of CO_2 over a range of temperature and pressure changes using National Institute of Standards and Technology (NIST) Reference Fluid Thermodynamic

and Transport Properties Database (REFPROP) [15]. The large density change near critical point could translate into less compression work required by compressors to be inputted to the working fluid [14]. However, near the critical point as shown in Figure 1.6, the specific heat of CO_2 reaches its maximum and most of the heat is rejected near 305 K. On the other hand, large variations in specific heat could complicate the recuperator design due to the change in pinch-point location [14]. Consequently, the recuperator size and the overall power cycle efficiency could be negatively affected since a high mass flow rate of cooling water will be required [14, 16] to adjust the temperature properly. Furthermore, combustion process operation near critical point is not ideal since a small change in pressure and temperature could lead to phase change, which causes pressure oscillations and motivate combustion instabilities. The pressure oscillations could also promote thermal fatigue and corrosions of material [17].

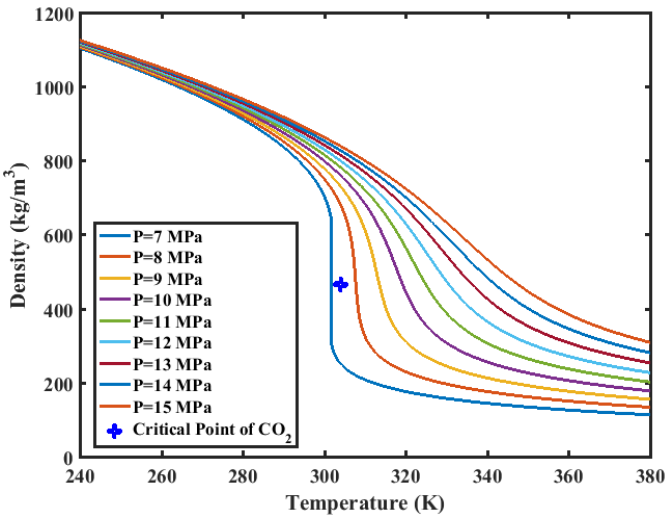

Figure 1.5. Density variation of CO_2 at different temperature and pressure conditions

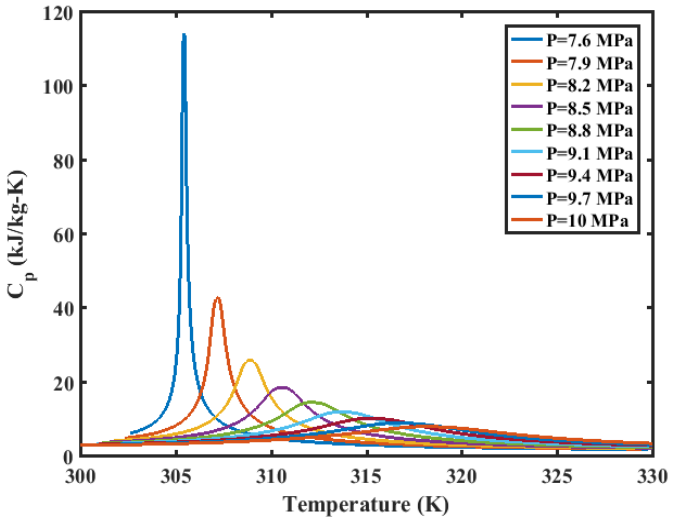

Figure 1.6. Specific heat change at constant pressure of CO_2 at different temperature and pressure conditions

To overcome the issues raised above, a potential solution is for the power cycles to operate above critical point (critical pressure and critical temperature) of CO_2. Such power cycles is known as supercritical CO_2 (sCO_2) power cycle, and it has shown to have high efficiencies and lower the electricity generation cost. At supercritical conditions, the fluid properties lie between those of liquids and gases. At these conditions, the fluid has similar densities to that of liquid while its diffusivities and viscosities are similar to those of gas [18].

Two major sCO_2 power cycles could be listed as indirect (closed) and direct (open) cycles. In indirect sCO_2 power cycle, once the heat is released from the combustor, a Primary Heat Exchanger (PHX) is utilized to transfer the heat to the sCO_2 fluid (the working fluid). Following that is the expansion process, which is done through the turbine. Two recuperators (high-temperature and low-temperature) are implemented in the cycle to extract the heat from the turbine exhaust and is used to pre heat the sCO_2 prior to entering the PHX. To enhance the performance of the recuperators near the critical point of CO_2,

Main Compressor (MC) and Recycle Compressor (RC) are added to the cycle [19]. An alternative to the indirect sCO_2 power cycle is direct-fired sCO_2 power cycle which features thermal efficiencies as high as 50% [16, 19-22] while simultaneously allowing a nearly complete capture for carbon sequestration at elevated pressures. As shown in Figure 1.7, in a direct-fired sCO_2 power cycle, the fuel (typically natural gas or syngas) and oxidizer are separately introduced to the combustor with a high-level of sCO_2 dilution levels. The heat release from the combustion products (primarily H_2O and CO_2) are expanded in the turbine and power is generated. A compact heat exchanger (recuperator) is utilized in the cycle to transfer the heat to the CO_2 prior to its introduction to the combustor inlet. The recuperator also makes the water from combustion exhaust products to be condensed and once a cooler is used, it can be separated from cycle and stored. The remaining portion of the products, which mainly consists of CO_2, could be pressurized by pre-compression (PC) to raise its pressure to the critical pressure and a pump (P) for storage purposes. However, the majority of the sCO_2 is used to recirculate back into the recuperator and the combustor [19].

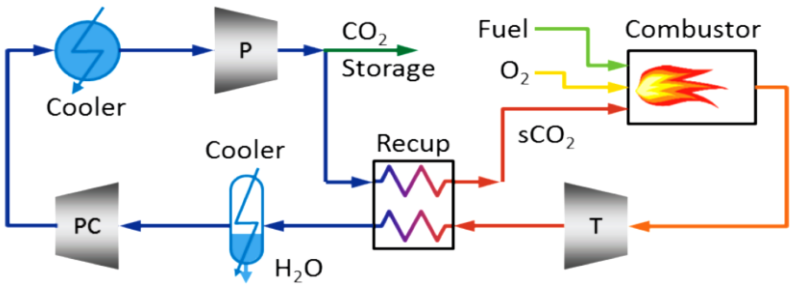

Figure 1.7. Schematic of a direct sCO_2 power cycle [19]

While there are many similarities in the components employed in indirect and direct-fired sCO_2 power cycles, the operation conditions are quite different from one another. For instance, one of the major differences between these two cycles is the turbine inlet temperature. In indirect sCO_2 power cycles, the turbine inlet temperature is limited by the material properties used in the heat exchanger. This limitation is analogues to steam power cycle (Rankine cycle) discussed earlier where researches are still undergoing to develop new materials to increase the turbine inlet temperatures to about 700–760 °C [19]. This value for direct-fired sCO_2 power cycles could be much higher due to the fact that internal combustion is employed in this open cycle. As shown in Figure 1.7, the hot combustion exhaust gas is inputted directly to the turbine where the inlet turbine temperature could be much higher than 700–760 °C. Therefore, cycle efficiencies could be improved substantially compared to the indirect cycle. The oxy-fuel, sCO_2 power cycle leverages Allam cycle [23] for operation to further enhance the design by reducing the apparatus size and operate in a cost-effective manner. In this cycle, nearly 95% of the mass flow in the combustor consists of CO_2 and the rest makes up the fuel and oxidizer [23]. The larger amount of CO_2 in the system could result in retaining great amount of heat in the cycle, which results in lowering the amount of fuel and oxygen required to keep the desired combustion temperature. Consequently, a smaller air separation unit is required, which contributes to making the cycle compact in size [23].

1.2 Problem Statement

In Allam cycle, the turbine pressure ratio is expected to be 8–12 which translate into a turbine exit pressure of 20–30 MPa [19]. Therefore, the direct fired sCO_2 power cycle requires combustors to operate at pressures in the range of 10 to 30 MPa (100–300 bar) and inlet temperature of approximately 900–1500 K [23]. At these severe conditions, existing conceptual combustor design for sCO_2 power cycles relies on autoignition to stabilize flame inside the combustor. Therefore, one of the key requirements in designing such combustors is the comprehensive knowledge of chemical kinetics, in particular ignition delay properties at those conditions.

The prediction of ignition delay times (IDTs) at the conditions relevant to sCO_2 combustion environment could be estimated by performing simulations implemented in chemical kinetic solvers. However, the choice of kinetic model becomes ambiguous and requires further investigations. For example, as shown in Figure 1.8 and Figure 1.9, the deviation in IDT predictions by some of the widely-used kinetic models increases as the pressure increases. GRI 3.0 [24], HP-Mech [25], USC Mech II [26], FFCM-1 kinetic model [27] and Aramco 2.0 mechanism [28-34] are some of the well-known kinetic models currently used for studying detailed combustion chemical kinetics of methane, natural gas and syngas. However, as shown below, the prediction of IDTs by these mechanisms for these fuels under high-CO_2 dilution levels diverge as the pressure increases to 300 bar. In some cases, the discrepancies in IDTs predicted among these kinetic models could be as high as a factor of 2. Therefore, further investigations are required to validate these chemical kinetic models.

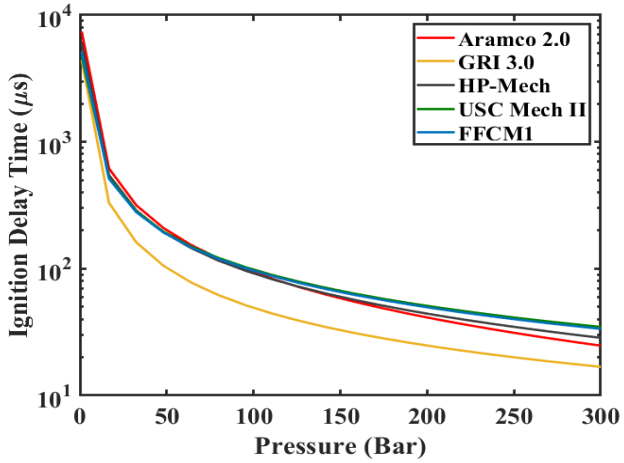

Figure 1.8. Ignition delay time predictions for $CH_4/O_2/CO_2$=9.5/19/71.5 at 1400 K from 1 bar to 300 bar

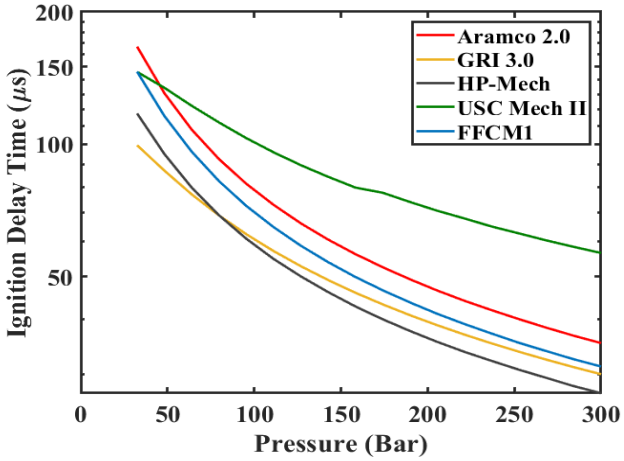

Figure 1.9. Ignition delay time predictions for $H_2/CO/O_2/CO_2$ =14.8/14.8/14.8/55.6 at 1200 K from 30 bar to 300 bar

1.3 Objectives and Structure of the Thesis

The goals of the dissertation are fourfold: 1) Develop a shock tube, 2) Collect data for methane and syngas at high-pressure conditions, 3) Understand the role of diluent gas, and 4) Work toward validation of the chemical kinetic models. To accomplish these goals, a high-pressure shock tube with unique design features is assembled and operated at

pressures as high as 200 bar. The experimental data are then compared with the simulation results using the mechanisms mentioned in section 1.2. Since these mechanisms are different in details, the second step towards validation is taken by analyzing the mechanisms themselves through sensitivity and reaction pathway analyses in order to identify key reactions in controlling ignition delay times and the most dominant pathways.

The autoignition chemistry is mainly a function of pressure, temperature and bath gas. To study the effect of pressure, experiments are conducted at 100 and 200 bar (relevant to sCO_2 combustion environment) with CO_2 dilution levels as high as 95.5% over a temperature range of 1100–1400 K. On the other hand, the chemical effect of CO_2 at supercritical conditions on methane and the syngas mixture combustion could be studied by replacing this bath gas with an inert gas. For this purpose, similar experiments at 100 and 200 bar and a temperature range of 1100–1400 K are conducted in an argon bath gas. Provided the experimental conditions will be compared with simulations over the range of known temperatures, the effect of pressure and bath gas could be studied independently. The sensitivity and reaction pathway analyses are also performed in a similar manner. The results obtained from such analyses and experimental work provide answers to inquiries raised from sCO_2 oxy-combustion community and pave the path for future chemical kinetics modeling developers in this field.

The structure of this thesis is as follows. Chapter 2 presents an extensive literature review on ignition delay time measurements of methane and syngas at various pressures and temperature conditions under different diluents (bath gases). Key findings from these studies, which are relevant to the current work are summarized in this chapter. Chapter 3 presents the experimental approach with highlighting key features of the facility. Chapter

4 and Chapter 5 introduce experimental and simulation results for methane and a syngas mixture of H_2/CO=95:5, respectively. Finally, the conclusions and future works are presented in Chapter 6.

CHAPTER 2. Literature Review

2.1 Methane Ignition Delay Time Measurements

As the main component of natural gas and one of the most widely distributed fuels, methane (CH_4) ignition chemistry and its combustion behaviors under various conditions have been studied extensively. The ignition delay times (IDTs) of methane in various mixtures have been studied thoroughly over the past several decades under different conditions. The majority of studies involve investigating parameters such as temperature, pressure, equivalence ratio, dilution gas and composition that could potentially have impacts on combustion chemistry. Early studies are mainly focused on developing chemical kinetic mechanisms that could explain the ignition behavior of methane at low pressures (up to 15 atm) and temperatures as high as approximately 2,000 K in inert bath gasses (such as argon or nitrogen). In many of the early works, series of elementary reactions that could potentially explain and predict ignition delay times are introduced along with proposed rate coefficients of each. While these studies provide the building blocks and first attempts towards understanding the ignition chemistry, in later works the conditions such as temperature and pressure range were extended to wider ranges. Moreover, new key reactions were found and included in methane chemical kinetic mechanisms.

In this section of the thesis, a comprehensive literature review along with the key findings associated with each study are presented. It should be noted that in many of these works, shock tubes are used to measure IDTs, calculate reaction rate coefficients and obtain species time histories. The principle of operations of shock tubes are discussed in the next

chapter of this thesis along with advantageous and disadvantageous associated with them. For the purpose of this chapter, however, it is important to note that shock tubes have been implemented and validated in studying autoignition delays for a variety of fuels in the past [28, 35-46].

The very first study on methane oxidation and pyrolysis in a shock tube was done in 1959 by Skinner and Ruehrwein [47] in temperature range of 1200–1800 K and a pressure range of 3–10 atm in an argon bath. In this study, based on comparison in enthalpy of reaction (ΔH), it was concluded that the chain initiation step is through oxidation ($CH_4+O_2 \rightarrow CH_3+HO_2$) rather than a pyrolysis reaction ($CH_4 \rightarrow CH_3+H$). It was also suggested that for low temperature experiments, the initial stage of oxidation is through: $4CH_4+O_2 \rightarrow 2C_2H_6+2H_2O$ since almost equal amounts of water (H_2O) and ethane (C_2H_6) were observed in the main products. One of the main conclusions from this work was that due to lack of kinetic data on chain branching reactions, the precise meaning of ignition delay time remained unknown.

In 1963, Asaba *et al.* [48] conducted experiments of methane-oxygen mixtures in air and argon dilutions under lean and rich conditions for a temperature range of 800–2200 K and a pressure range of 7–10 atm. In this study, it was shown that the oxygen atom produced by: $CH_2O+O_2 \rightarrow HCO_2H+O$ could react with methane such as in $O+CH_4 \rightarrow CH_2+H_2O$ where this reaction occurs in both lean and rich mixtures. Following this reaction, there were two scenarios where differentiated the ignition chemistry of methane in rich versus lean conditions. In the rich mixtures the chain termination reaction: $CH_2+CH_4+M \rightarrow C_2H_6+M$ took place while in lean mixtures chain branching reaction $CH_2+O_2 \rightarrow HCO+OH$ occurred. Based on these observations, it was suggested that as the

concentration of methane increases, oxygen atoms were deactivated in terms of their reaction with methane even though oxygen atoms were important in chain branching reactions. Following Asaba *et al.* [48], in 1964, Miyama and Takeyama [49] conducted similar experiments in highly diluted argon bath for a temperature range of 1050–2100 K and a pressure range of 3–9 atm. However, in this study, it was concluded that the rate-determining step of methane oxidation under lean conditions was $CH_2+O_2 \rightarrow HCO+OH$. While this conclusion is different from Asaba *et al.* [48], Miyama and Takeyama [49] speculated that the difference between dilution levels and different temperature ranges of the experimental conditions were the reasons for this discrepancy.

The induction time (ignition delay time) of methane at lower pressure ranges and various temperature ranges studied in later years [43, 50-55] and various suggestions were given in reactions most important for ignition events. Seery and Browman [50] studied the oxidation of methane behind reflected shock waves in a temperature range of 1350–1900 K and a pressure range of 1.5–4 atm in equivalence ratios (Φ) of 0.2, 0.5, 1, 2 and 5 in argon bath gas. Different from previous studies, this work utilized chemiluminescent emissions and absorption of OH radical during the ignition period. The induction times were shown to be strongly dependent on the rate coefficient (k) of reaction $CH_4+M \rightarrow CH_3+H+M$. Methyl radical ($CH_3$) oxidation was found to be important through $CH_3+O_2 \rightarrow HCO+H_2O$. Somewhat similar conclusions were made by Lifshitz *et al.* [43] where two predominant initiation reactions in controlling ignition delay times were introduced as $CH_4 \rightarrow CH_3+H$ and $CH_3+O_2 \rightarrow CH_2O+OH$. In this study, the ignition delay times of methane were measured in a shock tube for a temperature range of 1500–2150 K and a pressure range of 2–10 atm and Φ of 0.5, 1 and 2.

Three comprehensive studies and early attempts in developing comprehensive methane oxidation mechanism were done by Frenklach *et al.* [56], Spadaccini and Colket [54] and Treviño and Méndez [53]. In a study done by Spadaccini and Colket [54], methane ignition delay times were obtained in a temperature range of 1300–2000 K and a pressure range of 3–15 atm with an equivalence ratios of 0.45–1.25 in argon bath for chemical kinetics analyses. Through their analyses, methyl radical (CH_3) recombination was found to be an important radical sink. The ignition delay time calculated in this work was found to be very sensitive to rate constants of reactions involving hydroperoxyl (HO_2) and hydrogen peroxide (H_2O_2) formations. Consistent with the results obtained by Frenklach *et al.* [56], reactions $CH_4(+M)\rightarrow CH_3+H(+M)$ and $CH_4+O_2\rightarrow CH_3+HO_2$ were found to contribute to the initial radical buildup in initiating ignition process. However, these two reactions seemed to have sensitivities in ignition delay time. This observation was evident by investigating the production rate of radicals involved in methane oxidation at 1500 K and 2.46 atm as shown in Figure 2.1. The strong endothermicity of these two reactions and production of relatively low reactive radicals (CH_3 and HO_2) were pointed out as the reasons for such observations.

Frenklach *et al.* [56] in 1992 attempted to develop a single physically-justifiable mechanism that would predict all existing experimental data. A method of systematic optimization was used to determine optimum set of parameters for a methane combustion mechanism. As a result of this work, a series of 149 trial reactions were proposed. While the methodology presented in this work did not yield to a unique solution, several issues were highlighted in addressing this issue. They concluded that higher accuracies in the following parameters are required: i) The rate coefficients of several reactions involving

self-addition of methyl radicals, ii) The rate coefficients for methyl oxidation by O_2, OH, O and iii) The collision efficiencies of water in some reactions.

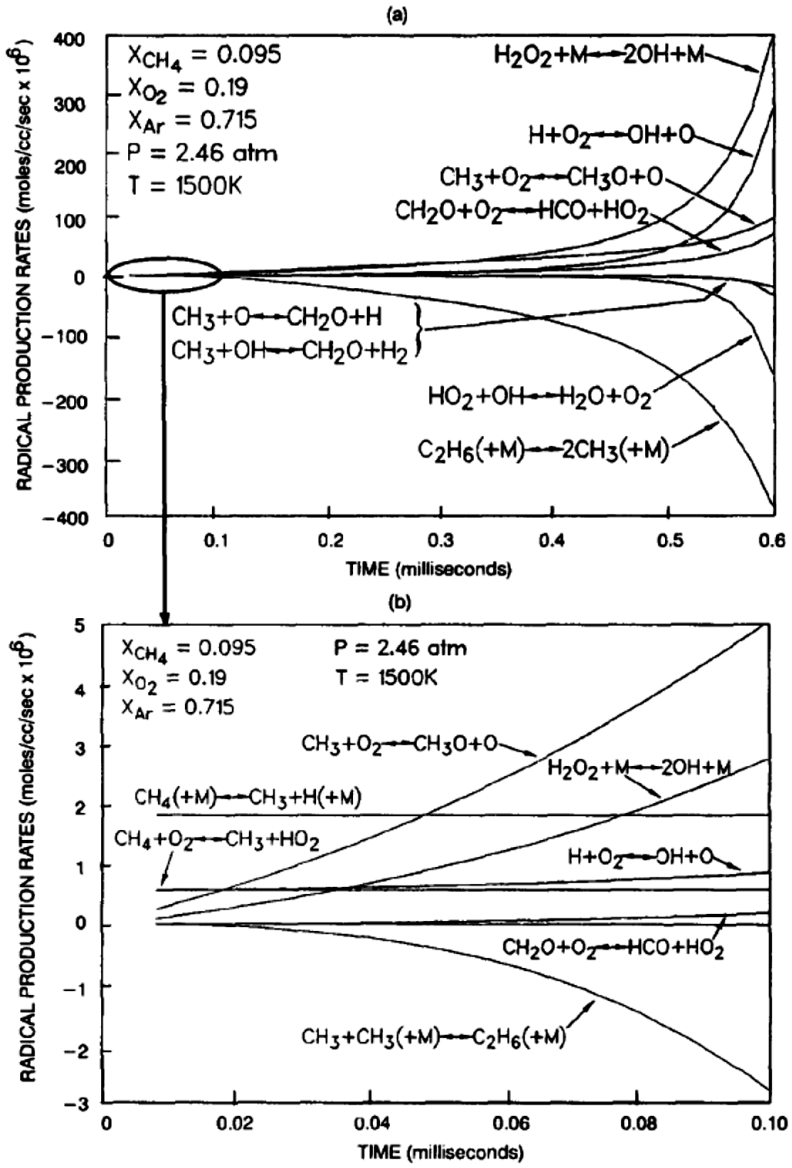

Figure 2.1. Radical formation during methane autoignition [54]

Treviño and Méndez [53] studied the transient process leading to ignition for stoichiometric methane/air mixtures at atmospheric pressure condition and a temperature range of 1000–1800 K using numerical techniques for solving stiff differential equations.

A minimum of six global steps were obtained as a result of appropriate reduced kinetic mechanism which involved mainly the reactions containing CO, C_2H_6, C_2H_4, C_2H_2, H_2, H_2O and very small amount of CO_2. The chain initiating reactions $CH_4 \rightarrow CH_3+H$ and $CH_4+H \rightarrow H_2+CH_3$ were identified to be important at the beginning of the ignition process. Furthermore, the radicals CH_3 and CH_2O were found to reach a steady state conditions at much earlier times prior to ignition.

The effects of dilution gas on ignition delay times of methane at low pressures were studied early on by Grillo and Slack [51] in 1976 and Zellner *et al.* [52] in 1983. Grillo and Slack [51] investigated the ignition effect of nitrogen (N_2) addition up to 15.2% in methane/oxygen/argon mixtures in the temperature range of 1640–2150 K and in a pressure range of 1–6 atm for equivalence ratios of 1 and 2. The ignition delay times obtained in mixtures studied in this work overlapped substantially, suggesting that replacing argon by nitrogen has little or no effect in that regards. Zellner *et al.* [52] studied a similar phenomenon by in 2% CH_4 mixture at 3.3 atm, however the temperature range in this study was approximately in a range of 1400–1800 K. It was found that the ignition delay time is shortened by a factor of roughly 1.6 when synthetic air (O_2/Ar=20/80) was replaced by raw laboratory air. The authors concluded that the vibrational nonequilibrium of N_2 has an effect on ignition delay time, which is caused by the translational temperature being higher than the equilibrium temperature of the gas. They added N_2 (v=0) +M ↔ N_2 (vibrationally equilibrated) +M to the kinetic model to account for the vibrational relaxation effect of N_2.

Methane IDT measurements in argon and nitrogen bath gasses are not limited to low pressures. Many studies have been focused on obtaining high-pressure ignition delay times of methane at various temperature ranges in shock tubes or rapid compression

machines (RCMs) [46, 57-62]. Huang *et al.* [58] studied CH_4/air mixtures with equivalence ratios of 0.7, 1 and 1.3 at temperatures 1000–1350 K and a pressure range of 16–40 atm. Through sensitivity and reaction flow analyses, they reported reactions $CH_3+O_2 \leftrightarrow CH_3O_2$ and $CH_3O_2+CH_3 \leftrightarrow 2CH_3O$ could promote ignition at lower temperature conditions. Furthermore, Reaction $CH_3+CH_3+M \leftrightarrow C_2H_6+M$ was found to be the main ignition inhibitor reaction at 1250 K where 36% of methyl radicals were reported to be consumed by this reaction.

Similar conclusions regarding the recombination reaction of CH_3 have been reached by El Merhubi *et al.* [60] and Burke *et al.* [59]. El Merhubi *et al.* [60] conducted experiments in a high-pressure shock tube at 10, 20 and 40 bar and a temperature range of 1400–2000 K with equivalence ratios of 0.5, 1 and 2 in argon bath. The recombination reaction of CH_3 radicals to form C_2H_6 was found to be less important in hindering ignition for lean mixtures due to the reduced concentrations of methyl radicals. Aramco Mech 1.3 [29], GRI 3.0 [24] and USC Mech II [26] were used to compare the ignition delay times obtained experimentally and good agreements were observed. Moreover, sensitivity analyses using these mechanisms showed that the competition between reactions $H+O_2=O+OH$ and $CH_4+H=CH_3+H_2$ in H atom abstraction was very important in controlling ignition chemistry. Burke *et al.* [59] obtained ignition delay time measurements of methane in a wide range of temperatures (600–1600 K) and pressures (7–41 atm) from a RCM and a high-pressure shock tube with equivalence ratios of 0.3, 0.5, 1 and 2 in air mixtures. The results of brute-force sensitivity analyses at pressure of 10 atm at 1056 K and 1470 K and at pressure of 25 atm at 993 K and 1436 K showed that methyl radical recombination to form ethane was the most inhibiting ignition reaction. At high

temperatures for both the pressure conditions, reaction $H+O_2 \leftrightarrow O+OH$ was identified as the most promoting ignition reaction. However, at both pressure conditions, reaction $CH_3O_2+CH_3 \leftrightarrow CH_3O+CH_3O$ was identified as the most ignition promoting reaction. Furthermore, as the pressure increased, their analysis showed rate constant of reaction CH_3+O_2 (+M) $\leftrightarrow$ CH_3O_2 (+M), which favored the formation of CH_3O_2, was pressure dependent and increased with pressure.

The IDT measurements of methane are not limited to low pressures in nitrogen or argon diluents. Petersen *et al.* [46] studied methane oxidation behind reflected shock waves in argon/nitrogen mixtures over a stoichiometry range of 0.5–4.0, a temperature range of 1410–2040 K and a pressure range of 9–480 atm. The IDTs were compared to the GRI 1.2 kinetic model [63], and good agreement between experiments and simulation was observed. The sensitivity analysis showed that as the pressure increased, while the major formation pathway of CH_3 remained unchanged, its removal pathway altered. $CH_3+HO_2=CH_3O+OH$, and $CH_3+CH_3+M=C_2H_6+M$ became increasingly important in controlling ignition with the increase of pressure over the dominant pathway $CH_3+O_2=CH_3O+O$ at low pressure conditions. In a later study, Petersen *et al.* [62] conducted shock tube ignition delay measurements of CH_4, O_2 and argon mixtures at equivalence ratios of 0.4 and 3.0, a temperature range of 1040–1500 K and a pressure range of 40–260 atm. The experimental data reasonably matched the predictions made by a modified version of GRI 1.2 [63] at most conditions. Predictions from this kinetic model still showed large deviations at higher pressures and lower temperatures, especially with high fuel concentrations. It was also pointed out that reactions $CH_3+CH_3O_2=2CH_3O$ and $H_2O_2+M=2OH+M$ were the dominant ignition promoters at high pressure and low

temperature conditions. Similar to the previous study, the primary inhibitor reaction to ignition was found to be $CH_3+CH_3+M=C_2H_6+M$ at all conditions.

Zhukov *et al.* [64] measured IDT of methane-air mixtures behind reflected shock waves at Φ of 0.5 for a temperature range of 1200–1700 K and a pressure range of 3 to 450 atm. Reasonable agreement between the experimental results and GRI 3.0 [24] were obtained for a wide range of pressures. Sensitivity analysis using GRI 3.0 [24] revealed that for pressures of 5 and 500 atm, reaction $CH_3+CH_3+M=C_2H_6+M$ was most important in hindering ignition, while reactions $HO_2+CH_3=OH+CH_3O$ and $H+O_2=O+OH$ were most influential in enhancing ignition.

The majority of ignition delay time (IDT) measurements were obtained in argon/nitrogen baths, with very few studies involving measurements in CO_2 baths. Pryor *et al.* [65] measured the IDTs of a stoichiometric mixture of methane, argon, carbon dioxide and oxygen for temperatures of 1650–2040 K, and pressures between 0.6 and 1.2 atm. The IDT was measured using three different techniques: broadband chemiluminescent emission, CH_4 concentration using a distributed feedback interband cascade laser, and pressure recorded by a dynamic pressure transducer. All three methods were then compared to results from high-speed camera images from an axial cross-section of the shock tube during combustion. The results showed that shock bifurcation can introduce large uncertainties in calculating IDTs. It was also shown that for mixtures with high CO_2 content, Aramco Mech 1.3 [29] and GRI 3.0 [24] were able to predict the ignition delay times as shown in Figure 2.2.

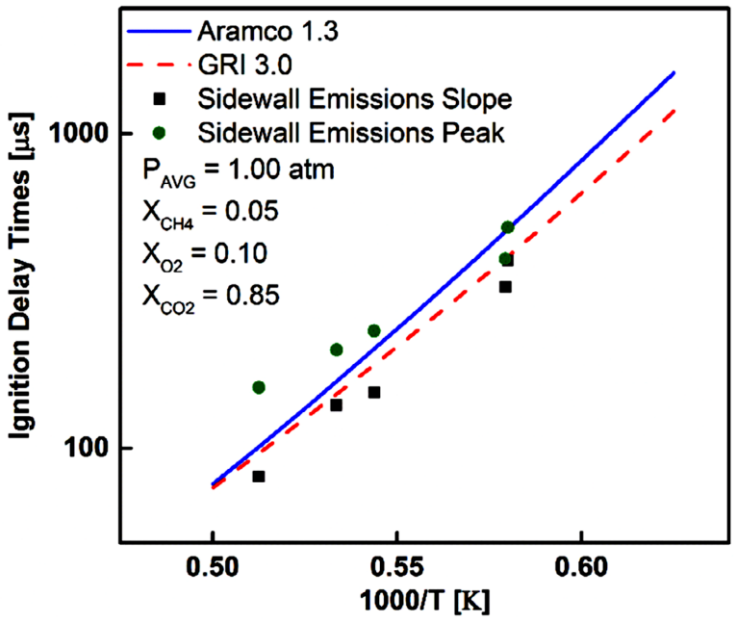

Figure 2.2. Ignition delay times for methane with carbon dioxide dilution [65]

Pryor *et al.* [66] and Zeng *et al.* [67] studied the ignition delay time measurements of methane in various dilution levels of CO_2 in argon and nitrogen baths, respectively. Pryor *et al.* [66] conducted experiments in stoichiometric methane mixtures for dilution levels of 30%, 60% and 85% CO_2 at temperatures between 1300 K and 2000 K and pressures between 6 and 31 atm. It was shown from this study that GRI 3.0 [24] and Aramco Mech 1.3 [29] performed well in predicting IDTs when compared to the experimental data. It was concluded from this study that CO_2 slowed the overall reaction rate due to its competition for H radicals with O_2 through $H+O_2 \leftrightarrow O+OH$ and $CO+OH \leftrightarrow CO_2+H$, which consequently its addition increases IDT. Similar conclusions were made by Zeng *et al.* [67] where the experiments were conducted in a pressure range of 1–10 atm and a temperature range of 1300–2100 K for dilution levels of 0%, 20% and 50% for CO_2 and Φ of 0.5, 1 and 2. GRI 3.0 [24] was also found to have good agreements with the experimental data in terms of predicting ignition delay times. Using this

mechanism in performing simulation from this work showed that the third-body efficiency of CO_2 is stronger than N_2.

Koroglu *et al.* [68] also carried out measurements for CH_4, CO_2 and O_2 in argon bath gas for temperatures of 1577–2144 K, a pressure range of 0.53–4.4 atm, Φ of 0.5, 1 and 2, and CO_2 mole fractions of 0%, 30% and 60%. It was found CO_2 addition did not significantly change the IDT, and Aramco Mech 1.3 [29] and GRI 3.0 [24] could reasonably predict the IDTs as shown in Figure 2.3.

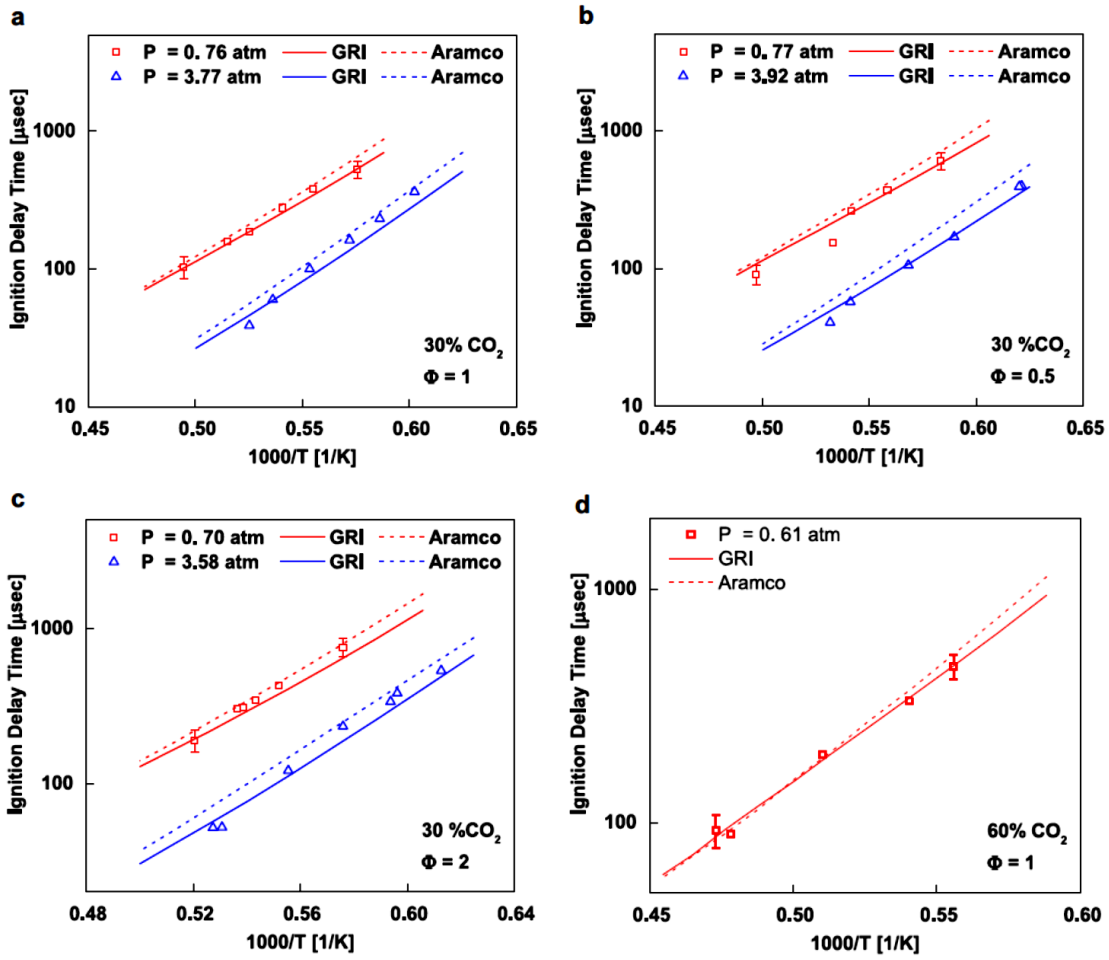

Figure 2.3. Ignition delay time measurements data at various pressures, equivalence ration and CO_2 concentrations [68]

Hargis and Petersen [69] measured IDTs of methane in nitrogen and carbon dioxide for an equivalence ratio of 0.5, a temperature range of 1450–1900 K, and pressures up to 10 atm. In their work, endwall emission and pressure measurements were used to capture the ignition event because shock bifurcation was minimized at the endwall. This study presented the first set of data obtained in a shock tube equipped with simultaneous sidewall and enwall pressure and emission measurements as shown in Figure 2.4(b). This feature was shown to be important when the traces were compared with the ones obtained in nitrogen bath gas as shown in Figure 2.4 (a). Modifying the third-body collision efficiency of CO_2 was studied and no significant effect on ignition delay time was noticed. It was also suggested that CO_2 plays no significant chemical role during ignition, and Aramco Mech 1.3 [29] simulations showed good agreement with the experimental results [69]. Main conclusions from this work were that CO_2 did not react chemically and it had little third-body efficiencies effect on ignition. These observations were confirmed by comparing the IDTs obtained in CO_2 baths versus N_2 baths (baseline mixture) as shown in Figure 2.5. In this figure, CO_2 is shown to slightly lengthen the IDTs, which was attributed to thermal effect of CO_2 such as absorbing energy release during reactions.

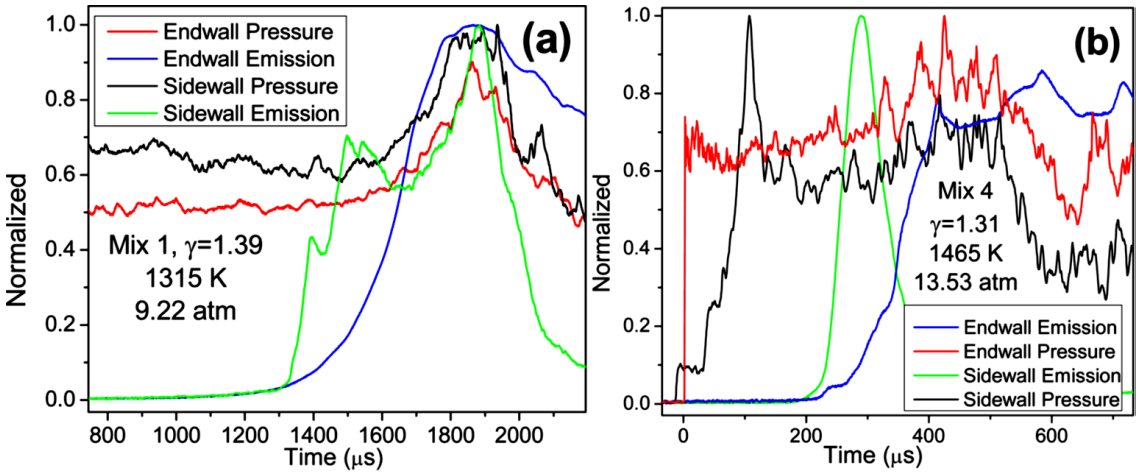

Figure 2.4. Endwall and sidewall pressure and emission traces for a) mixture 1 ($CH_4/O_2/N_2$=5/20/75) and b) Mixture 4 ($CH_4/O_2/CO_2$=5/20/75) [69]

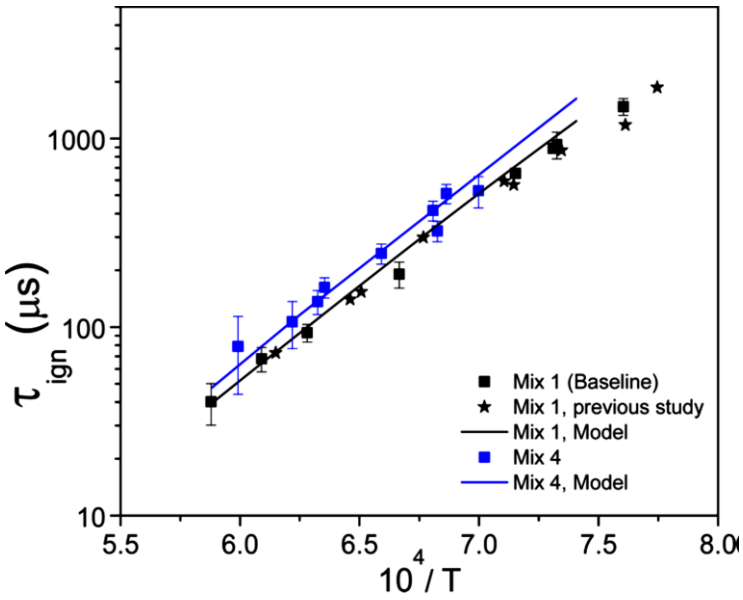

Figure 2.5. Ignition delay times for mixture 1 ($CH_4/O_2/N_2$=5/20/75) and Mixture 4 ($CH_4/O_2/CO_2$=5/20/75) at 10 atm [69]

Earlier this year, Shao *et al.* [70] reported IDT measurements of methane and hydrogen in highly diluted carbon dioxide mixtures up to 300 atm for a temperature range of 1045–1578 K. Only sidewall diagnostics and pressure measurements were utilized to obtain data in this study as shown in Figure 2.6. The IDT data were compared against Aramco 2.0 [28-34] and the FFCM-1 kinetic model [27]. It was found that at pressures

lower than 110 atm, both mechanisms were capable of predicting IDT values, with a deviation less than 20%. However, at higher pressure conditions (near 250 atm), Aramco 2.0 [28-34] outperformed FFCM-1 [27], having a better prediction for the ignition delay times as shown in Figure 2.7. Sensitivity analyses done in that study showed that CH_3 and HO_2/H_2O_2 related kinetics may significantly affect the ignition event.

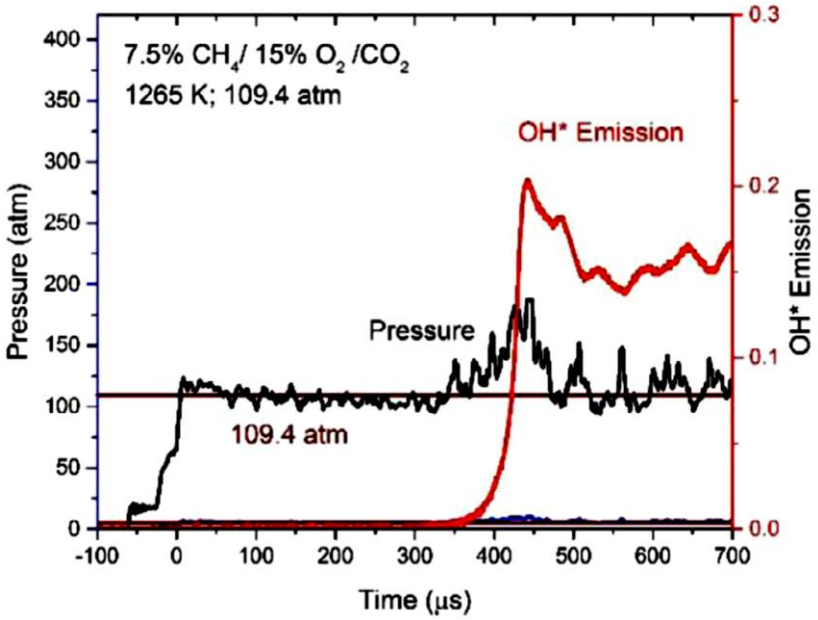

Figure 2.6. An example of IDT measurement for 7.5% CH_4/15% O_2/CO_2 mixture [70]

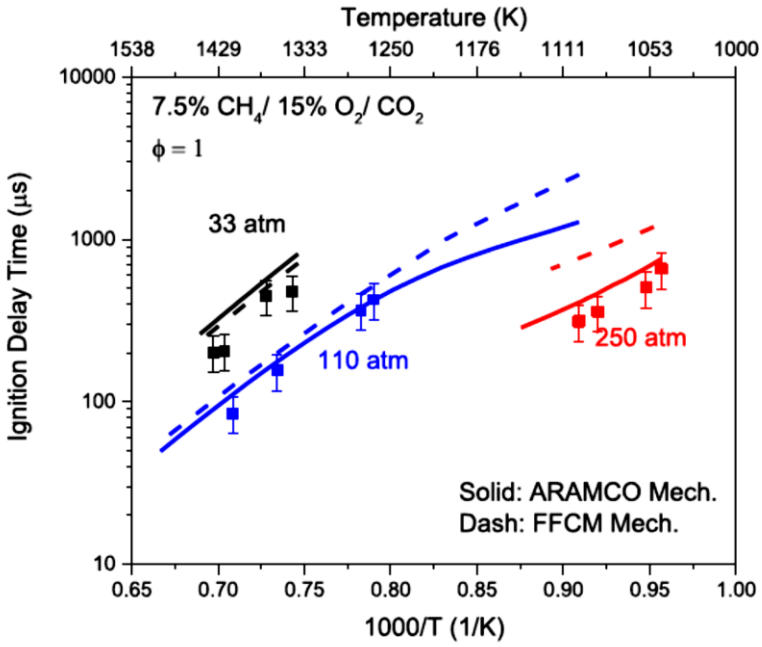

Figure 2.7. IDT measurement for $CH_4/O_2/CO_2$ mixtures at 33, 110 and 250 atm [70]

2.2 Synthetic Gas Ignition Delay Time Measurements

Synthetic gas (syngas) is a potential fuel candidate for sCO_2 oxy-combustion applications and an attractive source of energy. While its energy density is not as high as other abundant sources (such as natural gas or methane), however it can be produced from various sources such as coal and biomass. The main components of syngas are hydrogen (H_2) and carbon monoxide (CO), which could well vary in composition. This variation in composition could change combustion characteristics of this fuel such as flame speed and ignition behavior under different pressure and temperature conditions. Furthermore, the effect of bath gas (such as N_2, Ar, He, H_2O and CO_2) in these combustion properties could be significant. Therefore, investigating the chemical effect of the bath gas for this fuel at various pressure and temperature conditions is critical.

Numerous studies have been done towards understanding carbon monoxide and hydrogen oxidation independently. While syngas on its own could be treated as a fuel, the oxidation process of carbon monoxide and hydrogen are different on their own. Early attempts in exploring the oxidation of dry CO started in 1960s [71, 72]. Sulzmann *et al.* [71] conducted experiments behind shock waves in argon-diluted mixtures of CO and O_2 for a temperature range of 1500–3000 K and a pressure range of 0.5–1.5 atm in argon bath (70% to 85% dilution levels). At temperatures above 2400 K, the reactions attributing to ignition were identified as $CO+O_2 \rightarrow CO_2+O$, (M+), $CO+O \rightarrow (M+)\ CO_2^*$ and $CO_2^*+O_2 \rightarrow CO_2+2O$. It was also found that the addition of 0.1% H_2 in the mixture, decreased the ignition delay time at temperatures below 2400 K. However, at temperatures above this value, the presence of hydrogenase species did not affect the ignition delay times. In a later study from the same group, Myers *et al.*[72] studied the influence of hydrogen addition on ignition delay time of CO in a shock-heated mixture for a temperature range of 1500–3300 K and a pressure range of 0.4–1.6 atm. The mixtures of interest in this study were consisted of 0.01%–0.13% H_2, 10%–20% CO and 5%–20% O_2 in argon bath gas. Seven reactions were proposed to explain the oxidation of CO, given small amounts of H_2 were present in the mixture. These reactions were $CO+O_2 \rightarrow CO_2+O$, $O+H_2 \rightarrow OH+H$, $H+O_2 \rightarrow OH+O$, $CO+OH \rightarrow CO_2+H$, $(M+)\ CO+O \rightarrow (M+)\ CO_2^*$, $CO_2^*+O_2 \rightarrow CO_2+2O$, and $H_2+OH \rightarrow H_2O+H$. A similar conclusion as their previous study was made where the ignition time decreased by increasing the amount of hydrogen present in the mixture. However, at temperatures above 2400 K, the effect of adding 0.011% H_2 to the mixture on ignition became negligible.

Experimental attempts in understanding syngas oxidation have been the goal of many studies up to date. Early studies [73, 74] focused on exploring ignition characteristics of hydrogen and carbon monoxide in argon bath at low pressures and high temperatures. In a study done by Gardiner *et al.* [73], mixtures $H_2/O_2/Ar=1:5:94$ and $H_2/O_2/CO/Ar=1:5:3:91$ were heated in incident shock waves for a temperature range of 1400–2500 K and a pressure range of 0.15–0.3 atm. They reported a significant decrease in ignition delay times when carbon monoxide was added to the mixture. This ignition acceleration behavior was attributed to reactions $CO+OH=CO_2+H$ and $H_2+OH=H_2O+H$. Low-pressure experimental efforts continued to measure reaction rates of key reactions important to syngas oxidation. For example, in the study done by Dean *et al.* [74], emission signals obtained behind reflected shock waves for $H_2/O_2/CO/Ar$ mixtures at a pressure range of 1.2–8.3 bar and a temperature range of 2000–2850 K. The emission signals were then related to the absolute concentration of oxygen atoms and carbon dioxide. The data helped to modify the reaction rates for reactions $OH+CO\rightarrow CO_2+H$ and $O+H_2\rightarrow OH+H$ to a much higher values than expected by low temperature data extrapolation.

More detailed analyses on ignition chemistry of syngas were conducted at wider pressure and temperature ranges and also various levels of carbon monoxide concentrations. One of the most comprehensive studies in this regard was done by Kalitan *et al.* [75] where shock tube experiments were conducted at a temperature range of 890–1300 K, pressure regimes of 1, 2.5 and 15 atm and for CO/H_2 compositions of 5–80% H_2 in air. The experimental data were compared with ignition delay time predictions from five mechanisms (Davis *et al*. [76], Saxena and Williams [77], Li *et al.* [78], Sun *et al.* [79] and GRI 3.0 [24]) and excellent agreements were observed at high temperatures and low

pressures with some of the mechanisms. However, discrepancies as high as a factor of 5 were determined at high pressures and low temperatures. GRI 3.0 [24] was found to have the worst performance amongst all mechanisms in modeling CO/H_2 oxidation. This study showed that regardless of the mixture composition, pressure and temperature, reaction $H+O_2=O+OH$ was one of the most important reactions in enhancing ignition. At high pressures and lower temperatures, reactions $H+O_2+M=HO_2+M$, $CO+O+M=CO_2+M$ and $CO+HO_2=CO_2+OH$ were found to be the most influential in governing ignition behavior as shown in Figure 2.8. Particularly, reaction $H+O_2+M=HO_2+M$ was found to be extremely important in hindering syngas ignition. Reaction $OH+OH+M=H_2O_2+M$ showed an interesting behavior in the sensitivity analysis. This reaction showed to hinder ignition at 2.4 atm while at 14.9 atm it was shown to have a great impact on accelerating ignition.

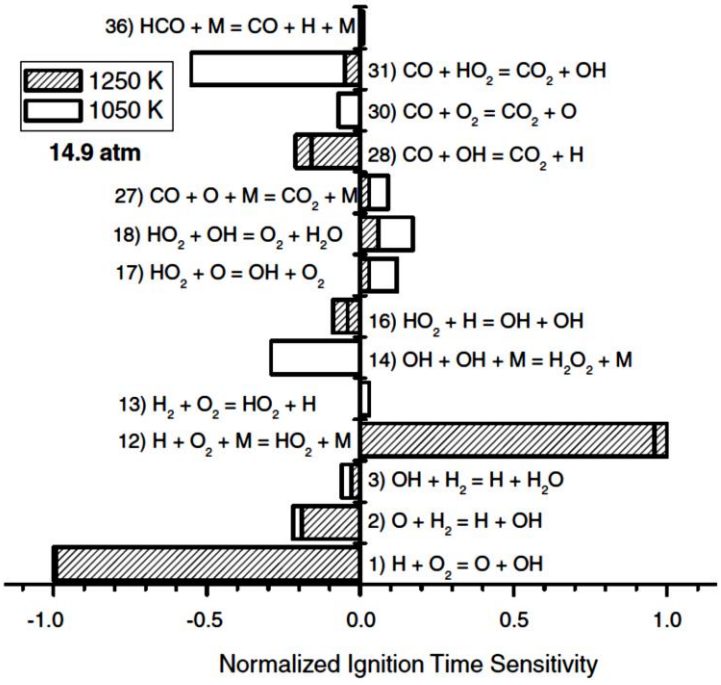

Figure 2.8. Ignition delay time sensitivity for 90% CO and 10% H_2 for 1250 K and 1050 K at 14.9 atm [75]

In a similar study, Herzler and Naumann [80] conducted experiments in a high-pressure shock tube at pressures of approximately 16 bar and temperatures between 1020–1260 K for lean mixture (Φ=0.5) of H_2/CO fuel blends (50%/50% and 5%/95%) in argon bath gas. The ignition delay times were compared with the results obtained from four chemical kinetics mechanisms (GRI 3.0 [24], LEEDS1.5 [81], USC Mech II [26] and Li *et al.* [78]) and none of them were able to reproduce the experimental results very well. Furthermore, the 50%/50% of H_2/CO fuel blend ignition delay times were almost identical to the case where only H_2 was present. However, for the 5%/95% of H_2/CO fuel blend, the IDTs were longer, which showed the prohibiting ignition characteristics of CO at large dilution levels. Through sensitivity analysis similar conclusions were obtained as in Kalitan *et al.* [75], where the most sensitive reactions to ignition were identified as $H+O_2=O+OH$ and $H+O_2+M=HO_2+M$. Other important reactions in governing ignition delay time were found to be $CO+OH=CO_2+H$, $CO+HO_2=CO_2+OH$, $O+H_2=OH+H$, and H_2O_2 (+M) = 2OH (+M). In another related study done by Mansfield and Wooldridge [82], experiments were conducted in a rapid compression machine for syngas mixture composed of H_2/CO with a molar ratio of 0.7 and Φ=0.1 and Φ=0.5 in air dilution for a pressure range of 3–15 atm and a temperature range of 870–1150 K. Reactions $H+O_2=H+OH$, and $H+O_2$ (+M)=HO_2 (+M) were also found to be very sensitive in OH sensitivity analysis related to ignition delay times in this work. Experiments at similar pressure and temperature conditions were performed by Thi *et al.*[83] for syngas mixtures with argon diluent at Φ=0.3, 1.0 and 1.5, pressures 2, 10, 20 bar and a temperature range of 870–1350 K. Interesting temperature dependencies of equivalence ratios at elevated pressures were observed, where higher equivalence ratios inhibited ignitions at high temperatures while an opposite effect was

observed for intermediate temperature cases. Reaction $H+O_2=O+OH$ was found to be the most dominant reaction in syngas oxidation at all conditions as a results of sensitivity analyses. Furthermore, as the pressure increased, reactions involving HO_2 and H_2O_2 were found to play dominant role in governing ignition delay trends. This study also reported that as the CO mole fraction in the mixture increased, reactions $CO+OH=CO_2+H$ and $CO+HO_2=CO_2+OH$ became increasingly important to ignition delay times.

Over years, experimental efforts in extending the pressure range to study high pressure ignition delay time of syngas mixtures continued in inert bath gases such as nitrogen and argon. Walton *et al*. [84] measured ignition delay time of H_2/CO (0.25 to 4.0 on mole basis) mixtures with equivalence ratios from 0.1 to 1.0 for a pressure range of 7.1 to 26.4 atm and a temperature range of 855 to 1051 K in a rapid compression machine. OH sensitivity analysis using Davis *et al*. [76] mechanism showed that this specie was most sensitive to chain branching reaction $H+O_2=O+OH$, the recombination reaction of $H+O_2$ to from HO_2 and $CO+HO_2=CO_2+OH$. Other studies [85-87] done at a similar pressure range also emphasized the importance of recombination reaction of $H+O_2$ to from HO_2 and the third-body collision effects of various dilution gasses on this reaction. Within a pressure range of 1.59–32.8 atm, Krejci *et al*. [87] measured ignition delay time and extensively studied various CO concentrations effect on syngas ignition. In this work, a high-pressure shock tube was used to obtain IDTs data for H_2/CO compositions of 80/20, 50/50, 40/60, 20/80 and 10/90 by volume for a temperature range of 960–2000 K in argon dilution. It was found that generally, the increase in CO amount could increase the ignition the ignition delay times. However, at pressures higher than 12 atm and low temperatures, the influence of CO in IDTs became indistinguishable as shown in Figure 2.9.

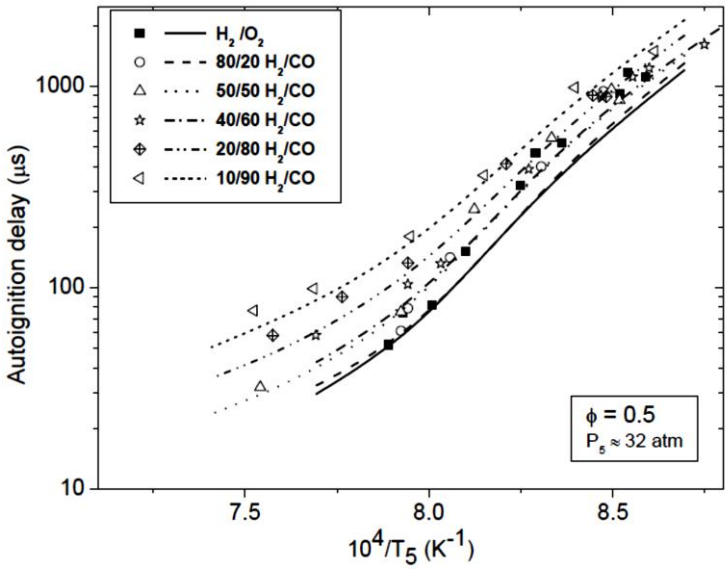

Figure 2.9. Ignition delay time for various mixtures of $H_2/CO/O_2$ in 98% Ar dilution at around 30 atm [87]

Various aspects of syngas ignition have been studied at pressures higher than 30 atm in inert bath gasses. For example, Mittal *et al*. [88], Kéromnès *et al*. [28] and Sivaramakrishnan *et al*. [89] obtained ignition delay times data of H_2/CO mixtures at maximum pressures of approximately 50, 70 and 500 atm, respectively. Mittal *et al*. [88] measured IDTs of H_2/O_2 and $H_2/CO/O_2$ mixtures (Φ=0.36 to Φ=1.6) in a rapid compression machine for a pressure range of 15–50 bar and a temperature range of 950–1100 K in argon and nitrogen bath gases. The experimental data was compared against several chemical kinetics mechanisms (Li *et al.* [78], Davis *et al*. [76] and GRI 3.0 [24]) and all models failed to predict the trend of ignition delays. The hindering effect of CO on ignition was observed to be more noticeable at elevated pressures as shown in Figure 2.10. Furthermore, reactions involving the production and consumption of HO_2 and H_2O_2 found to be important. The most important reactions in that regard were identified through sensitivity analyses and listed as $H+O_2=O+OH$, $H+O_2$ (+M) = HO_2 (+M), $HO_2+HO_2=H_2O_2+O_2$, H_2O_2

(+M)=OH+OH(+M), and H_2O_2+H=HO_2+H_2. Reactions CO+HO_2=CO_2+OH and CO+OH=CO_2+H were identified as the primary reactions for CO consumption as the concentration of this specie increased.

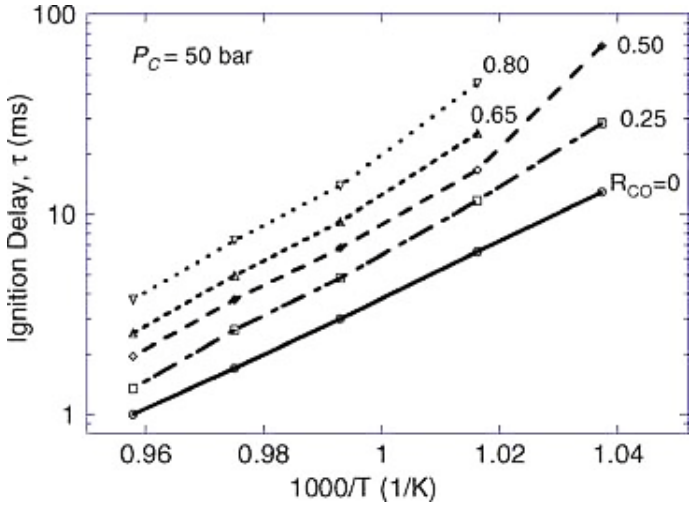

Figure 2.10. Ignition delay time for (H_2+CO)/O_2/N_2/Ar=12.5/6.25/18.125/63.125 at 50 bar [88]

The important role of reactions involving HO_2 and H_2O_2 at elevated pressures has also been pointed out by Kéromnès *et al*. [28] where IDTs were measured using rapid compression machines and a shock tube at pressures from 1–70 bar. Various H_2/CO/O_2/N_2/Ar mixtures were considered with equivalence ratios 0.1 to 4.0 and a wide temperature range of 914–2220 K. For the mixtures studied in this work, it was found that at high-pressure conditions and intermediate temperatures, reactions H_2+HO_2↔H+H_2O_2 and H_2O_2 (+M)↔OH+OH (+M) played key roles in ignition trends as shown in Figure 2.11. Furthermore, the effect of CO concentration was studied and for the concentrations higher than 50%, carbon monoxide showed inhibiting effect on ignition. Four reactions involving carbon monoxide were identified to be important in syngas ignition as in CO+O (+M) ↔CO_2 (+M), CO+O_2↔CO_2+O, CO+OH↔CO_2+H, and CO+HO_2↔CO_2+OH.

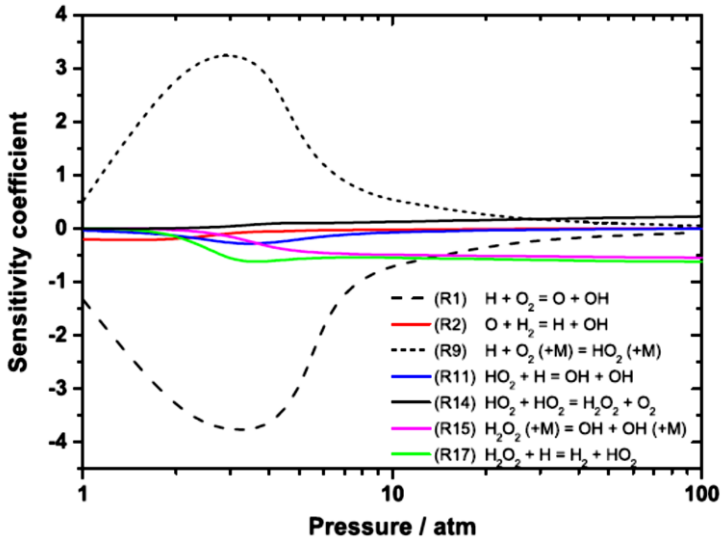

Figure 2.11. Sensitivity analysis of ignition delays for $H_2/O_2/N_2/Ar=1/1/1.88/1.88$ at 1000 K [28]

In a study done by Sivaramakrishnan *et al*. [89] oxidation of dilute CO mixture with 150–200 ppm of H_2 were measured behind reflected shock waves in a temperature range of 1000–1500 K and a pressure range of 21–500 bar for Φ=1.0 and Φ=0.5 mixtures. Some stable species such as CO, O_2 and CO_2 were sampled from the shock tube and analyzed by gas chromatographic and mass spectrometric techniques. The experimental results were compared against the predictions from chemical kinetics models (Davis *et al*. [76] and GRI 3.0 [24]) and it was shown that at lower pressure ranges (24 and 43 bar), well agreements were observed. However, at higher pressures (256 and 450 bar) the models underpredicted the formation of the stable species. CO fractional conversion was measured and shown in Figure 2.12, where a slow rate of CO decay was increased. However, as the pressure raised from 256 to 450 atm, no significant differences in CO conversion was noticed, suggesting a high-pressure limit is attained at 256 atm. Moreover, the CO concentration was shown to be most sensitive through reactions $H+O_2=OH+O$, $H+O_2+M=HO_2+M$, and

$CO+OH=CO_2+H$ under all pressure conditions. The next most important reactions involving CO concentration at 256 and 450 atm were listed as $HO_2+OH=O_2+H_2O$ and $CO+HO_2=CO_2+OH$.

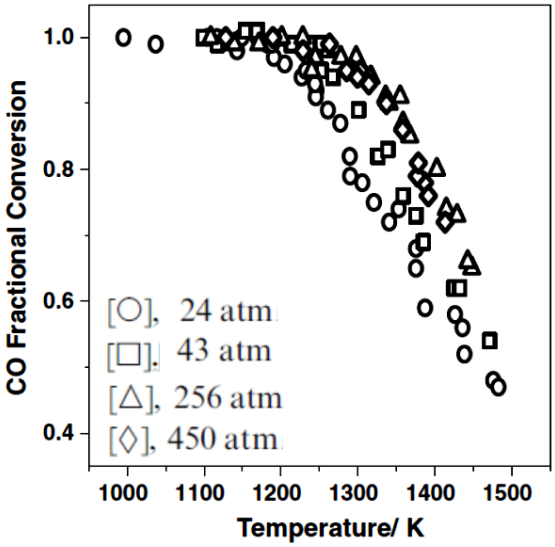

Figure 2.12. CO oxidation data at various pressures and Φ=1.0 [89]

Understanding ignition physics and chemistry are not limited to experimental efforts. Many modeling works have been evolved over years to introduce optimum sets of syngas chemical reactions. The majority of analyses such as sensitivity, reaction pathway and speciation leverage one or few of these models for simulation purposes. Some of the widely-used mechanisms have already been introduced in combination with the experimental results. The performance of these mechanisms under various syngas mixtures, pressures and temperatures have been tested and results are summarized in previous sections. However, there are additional works purely focused on modeling aspects of syngas ignition chemistry [53, 90-96]. Various techniques were used over decades in developing syngas kinetics models. The majority of these studies put emphasize on specific reactions that were most important in syngas ignition, such as $H+O_2=OH+O$,

$H+O_2+M=HO_2+M$, $CO+OH=CO_2+H$, and $CO+O+M=CO_2+M$ across various pressures, temperatures and H_2/CO compositions.

As concluded in most of the literatures on syngas ignition, H_2/O_2 combustion kinetics is essential in developing ignition models for syngas. Under a broad range of pressure, temperature and mixture composition in inert bath gasses, the ignition of syngas mixtures is mainly governed by H_2/O_2 combustion chemistry. Therefore, some studies [97-104] have also been devoted to developing and enhancing the kinetics modeling of such system. Contributions from these works provide valuable insights in explaining phenomena such as ignition delay times, laminar flame speeds and explosion limits of hydrogen and oxygen systems. These information serve as building blocks of developing comprehensive kinetic models necessary for syngas applications. One of the main contributions of these works, as far as kinetics modeling concerns, is obtaining precise reaction rate coefficients of key reactions highlighted earlier in this section.

One of the key reactions in controlling ignition delay times of syngas at elevated pressures is $H+O_2+M=HO_2+M$. This influential reaction was highlighted in many experimental and modeling studies of H_2/O_2 and $H_2/CO/O_2$ mixtures in argon or nitrogen bath gases. Specifically, at elevated pressure conditions this reaction was found to play a key role in dictating the ignition trends. Hence, the rate coefficient of this reaction and the third-body collisional effects at various bath gases were investigated previously in many studies. For example, in some of the early studies from 1977 to 2000 [105-108], the main focus was to study the reaction rate coefficient and obtain third-body collision efficiencies merely in highly-diluted argon and nitrogen baths. Among these studies, only Davidson *et al*. [106] measured rate coefficients at elevated pressures and temperatures. In this study,

UV laser absorption technique was implemented to obtain OH mole fraction profiles behind reflected shock waves at pressures of 50, 68 and 115 atm and temperatures between 1260 and 1375 K. While for M=Ar, the pressure-dependent reaction rate coefficient was found to be consistent with the values from GRI 1.2 [63] kinetic model, in the case of $M=N_2$, a reaction rate coefficient much higher than the one listed in GRI 1.2 [63] was recommended. In a study done in 2008, Fernandes *et al*. [109] extended the high-pressure limit in obtaining the reaction rate coefficients to 950 bar in bath gases Helium (He), Ar and N_2 for a temperature range of 300 to 900 K. In this study, laser flash photolysis was implemented in a high-pressure flow cell and high-pressure reaction rate coefficients were modeled and introduced.

Indeed the reaction rate coefficient and third-body collisional efficiencies for this important reaction ($H+O_2+M=HO_2+M$) have been studied for bath gases other than argon and nitrogen. Additional dilution gases of interest could be named as CO_2, H_2O, He, Neon (Ne), Krypton (Kr), and O_2 [110-112]. Bates *et al*. [111] not only measured the reaction rate of this reaction at elevated pressures (7–152 bar) and elevated temperatures (1050–1250 K) in Ar, N_2 and H_2O, but also reported the collision efficiencies for each bath gases. The collision efficiencies of N_2 and H_2O were reported as 3.3 and 20 respectively, relative to Ar at 1200 K. In a different study, Ashman and Haynes [110] studied the effect of different third bodies such as Ar, N_2, H_2O and CO_2 on the reaction rate coefficient in a laminar flow reactor for a temperature range of 750–900 K. The third-body efficiencies of 10.6, 2.4 and 0.56 (relative to N_2) were determined for H_2O, CO_2 and Ar, respectively.

While the majority of the H_2/O_2 and syngas ignition delay times have been measured under inert bath gas conditions over a wide ranges of pressure, there are very few

studies done in reporting IDTs under highly diluted CO_2 conditions. In all of these studies, only sidewall pressure and emission measurements were reported, despite the presence of large reflected shock bifurcations due to significant shock-boundary layer interactions. In a study done by Vasu *et al.* [113] a syngas/air mixture of H_2=8.91%, O_2=10.25%, CO=11.58%, CO_2=24.44% and N_2=44.83% in a temperature range of 974–1160 K and a pressure range of 1.1–2.6 atm was studied. It was shown that overall GRI 3.0 [24] was able to capture the trend and magnitude of the measured ignition delay times. Sensitivity analyses using GRI 3.0 [24] and Li *et al.* [78] revealed that reactions $H+O_2=O+OH$ and $H+O_2+CO_2=HO_2+CO_2$ were important in ignition delay time as shown in Figure 2.13.

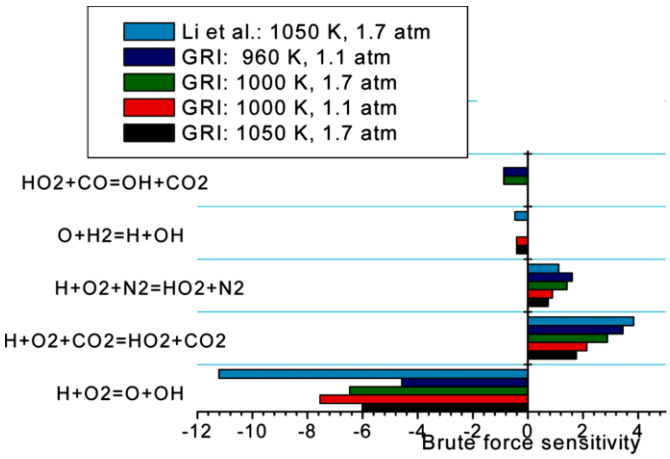

Figure 2.13. Brute force sensitivity analysis for H_2=8.91%, O_2=10.25%, CO=11.58%, CO_2=24.44% and N_2=44.83% mixture [113]

Reaction rate coefficient for reaction $H+O_2+CO_2=HO_2+CO_2$ was also measured near 8 atm and 1300 K in using OH absorption laser technique in a stoichiometric mixture composed of H_2=0.5%, O_2=0.25%, CO_2=30%, and balance argon. Experimentally measured reaction rate coefficient of this reaction was in a good agreement with expressions from GRI 3.0 [24]. OH sensitivity for this mixture is shown in Figure 2.14 and

once again reactions $H+O_2=O+OH$ and $H+O_2+CO_2=HO_2+CO_2$ were found to be very important.

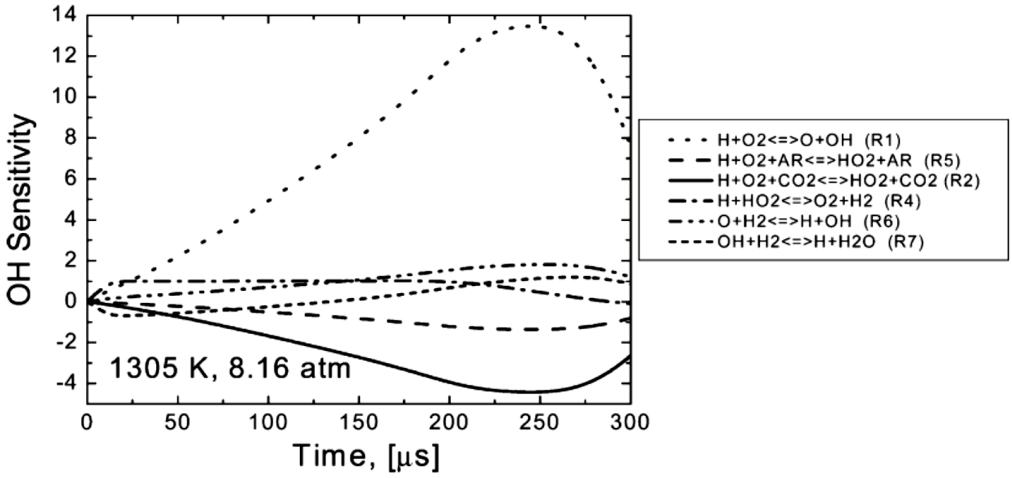

Figure 2.14. OH profile sensitivity to reaction rate coefficients for H_2=0.5%, O_2=0.25%, CO_2=30% and balance argon mixture [113]

In a study done by Barak *et al*. [114] within similar pressure and temperature ranges, syngas mixtures were studied under 60% and 85% CO_2 dilution levels by volume. The focus of this study, however, was to study the effect of equivalence ratio and H_2/CO ratio at a pressure range of 1.61–1.77 atm and a temperature range of 1006–1162 K. For the equivalence ratio increase from 0.33 to 0.5 and 1.0, longer ignition delay times were observed. On the contrary, increasing the H_2/CO ratio resulted in shorter ignition delay times. The IDTs obtained from this study were compared to the predictions from GRI 3.0 [24] and Aramco 2.0 [28-34] and none could capture the ignition delay times accurately as shown in Figure 2.15.

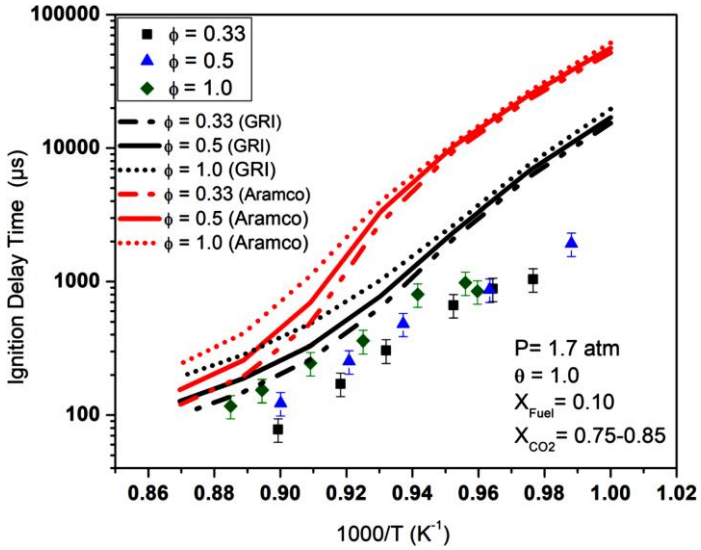

Figure 2.15. Ignition delay times of a syngas mixture at various equivalence ratios and their comparison with two kinetics mechanism [114]

In a very recent study done by Shao *et al.* [70], hydrogen ignition delay times were reported for mixtures $H_2/O_2/CO_2$=0.05:0.1:0.85 (pressure range of 37–40 atm, temperature range of 1170–1270 K) and $H_2/O_2/CO_2$=0.1:0.05:0.85 (pressure range of 103–311 atm, temperature range of 1083–1291 K). The experimental data were compared with Aramco 2.0 [28-34] and FFCM-1 kinetic model [27], where both mechanisms were able to predict the measurements within 20% as could be seen in Figure 2.16. Through OH sensitivity analysis, using FFCM-1 kinetic model [27], reactions involving HO_2 and H_2O_2 were found to be important to ignition delay time. The top eight sensitive reactions in that regard are shown in Figure 2.17 at pressure of 110 atm and temperature of 1200 K.

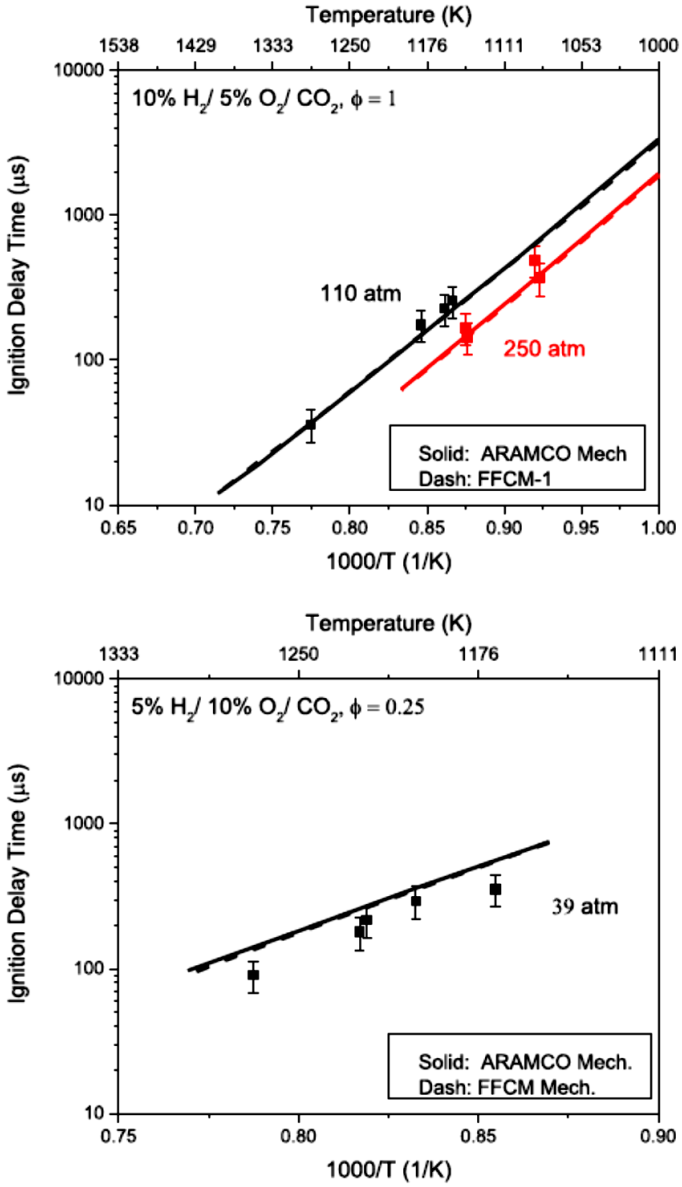

Figure 2.16. Ignition delay times of $H_2/O_2/CO_2$ at 39, 110 and 250 atm [70]

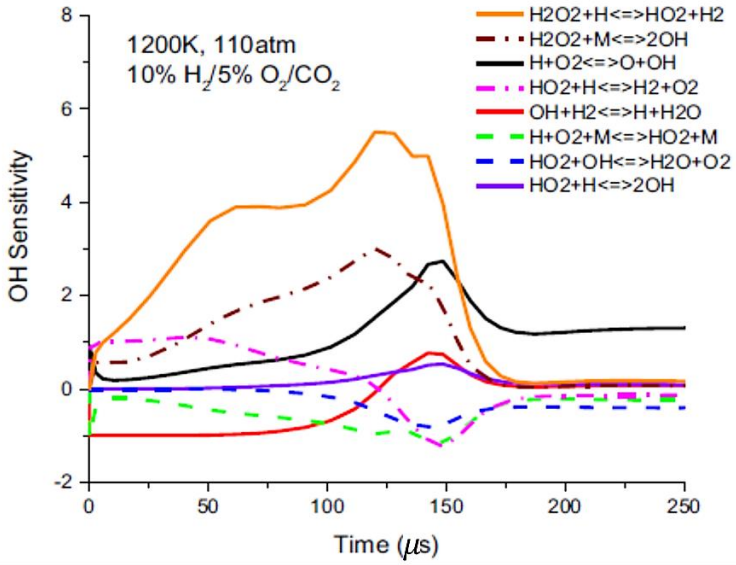

Figure 2.17. OH sensitivity for $H_2/O_2/CO_2$=0.1:0.05:0.85 at 110 atm and 1200 K [70]

2.3 Summary of the Literature Review

The majority of the studies conducted for natural gas (including pure methane) and syngas could be categorized in two groups: 1) Experiments, which are conducted at elevated pressures under large dilution levels of inert gases (mainly argon or nitrogen), and 2) Experiments which are conducted at low pressures, however in highly-diluted carbon dioxide environments. Only in one study, done by Shao *et al.* [70], ignition delay times of methane and hydrogen were obtained at elevated pressures (up to 300 atm) and in carbon dioxide bath gas. Figure 2.18 shows a summary of studies done on natural gas/methane and syngas ignition delay times and a comparison with the operating regime of sCO_2 power cycle combustor.

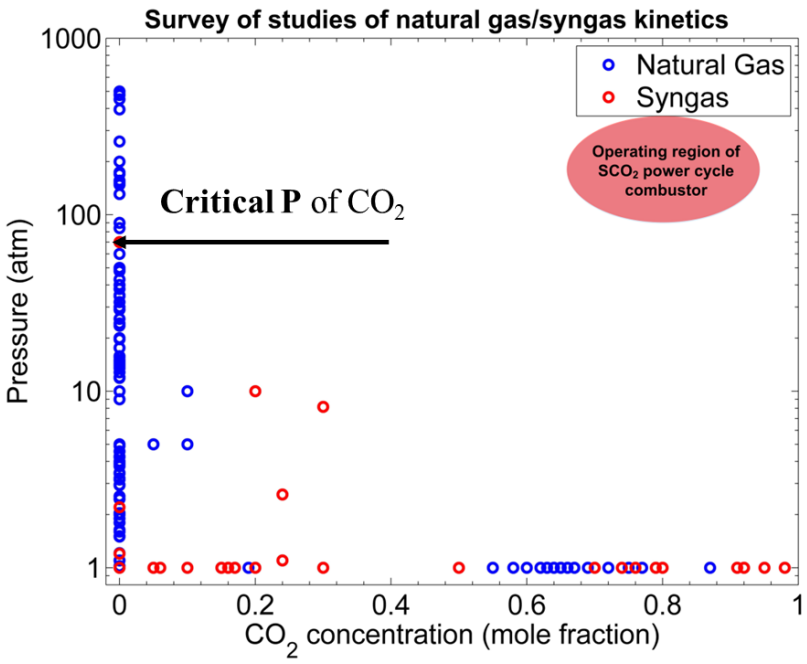

Figure 2.18. Survey of studies of natural gas and syngas and comparison with the operating region of sCO_2 power cycle combustor

CHAPTER 3. Experimental Methods

3.1 Principles of Operation

In this work, a high-pressure shock tube is used to measure autoignition delays. The principles of shock tube operation and their capabilities have been extensively studied in the past [42, 73, 115-127] and only a brief description is presented here. A shock tube, in its simple configuration, is a long tube with sealed ends separated into two sections (low pressure and high pressure section) by a diaphragm. The high-pressure side and low-pressure sections are termed as “Driver section” and “Driven section” respectively. Upon pressurizing the driver section, the diaphragm is ruptured and compression waves are formed. These waves quickly coalesce and form a single shock wave known as “Incident shock”, which travels down the driven section. Once the diaphragm is ruptured a series of expansion waves are also formed and these waves travel towards the end of the driver section. The driven section is filled with the test gas (i.e. the mixture of interest) and as the incident shock passes through the mixture, its temperature and pressure rises. Once the incident shock reaches the endwall of the driven section, the test gas is further compressed and heated and is effectively stagnant [128]. The test gas mixture behind the reflected shock could potentially be treated as a zero-dimensional reactor due to the effective step change in shock conditions (excluding a very thin boundary layer) [128]. The interaction of high pressure gas behind the incident shock wave and the test gas creates a contact surface also known as “Interface”, which travels at a lower speed than the incident shock wave towards the end of driven section.

The available test time in shock tube experiments is determined as the time between the arrival of the reflected shock (at the measuring section) and the arrival of weak waves generated from the interface or from the expansion fans reflecting from driver endwall [128]. The intersection of the reflected shock and the interface, under certain conditions (having different acoustic impedances), generates an expansion wave which propagates towards the hot gas and cools it [118]. A graphical description of shock wave, expansion wave, contact surface, and the test time is provided through *x*-*t* (location versus time) plot. Using the University of Wisconsin Shock Tube Lab (WiSTL) exact Riemann solver capable of generating *x*–*t* plots [129] and in-house MATLAB [130] code developed for solving one-dimensional gas dynamics equations in shock tubes [131], such plots are regenerated for the experimental conditions of the study. The complete *x*-*t* diagram shows the trajectory of the reflected shock and available test time at 100 bar for all mixtures studied here and the results are shown in figures below. Following the convention, P_5 and T_5 denote pressure and temperature in test section after the reflected shock, respectively. As could be observed from these plot, the maximum available test time for mixtures with CO_2 dilutions is 2 milliseconds and for large argon-diluted mixtures is 5 milliseconds. Similar tests times are obtained for experiments at 200 bar.

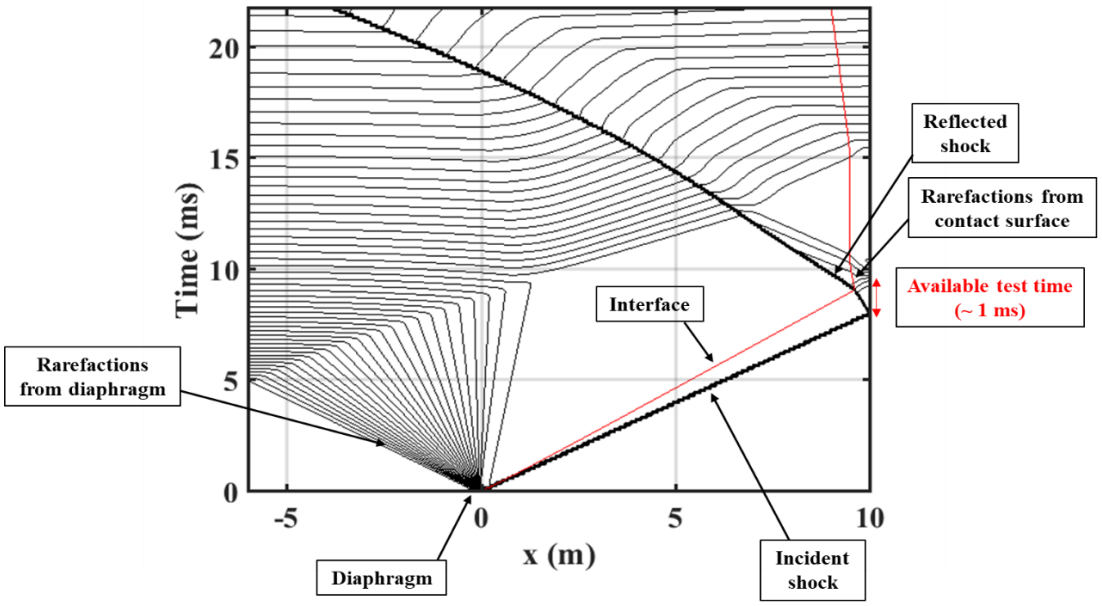

Figure 3.1. x-t diagram for P_5 = 100 bar and T_5 = 1274 K, Mach number = 3.79, driver gas: Helium, driven gas: $CH_4/O_2/CO_2$ (5:10:85)

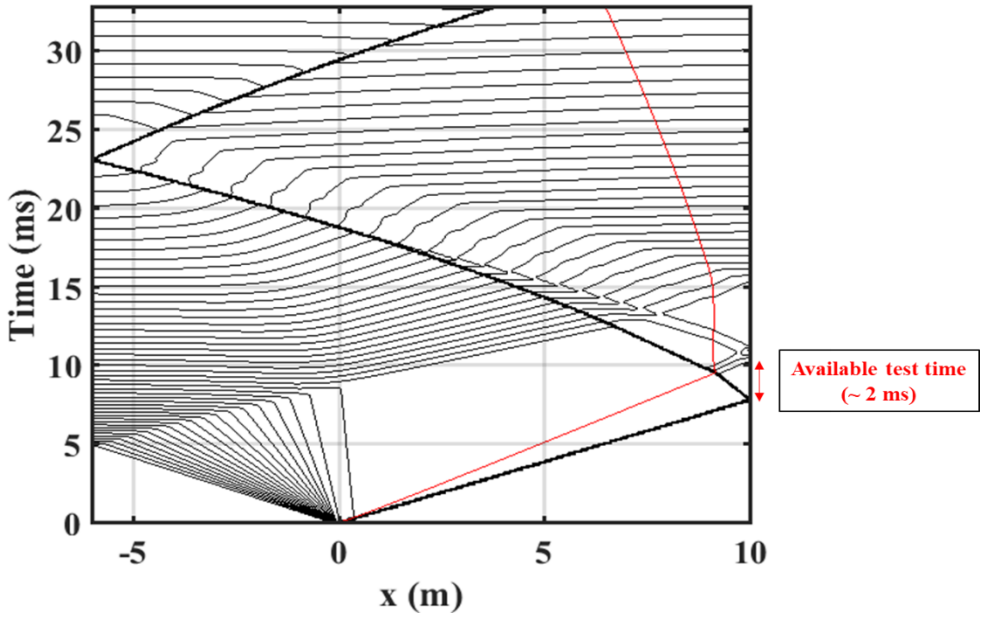

Figure 3.2. x-t diagram for P_5 = 100 bar and T_5 = 1186 K, Mach number = 3.64, driver gas: Helium, driven gas: $H_2/CO/O_2/CO_2$ (2.85:0.15:1.5:95.5)

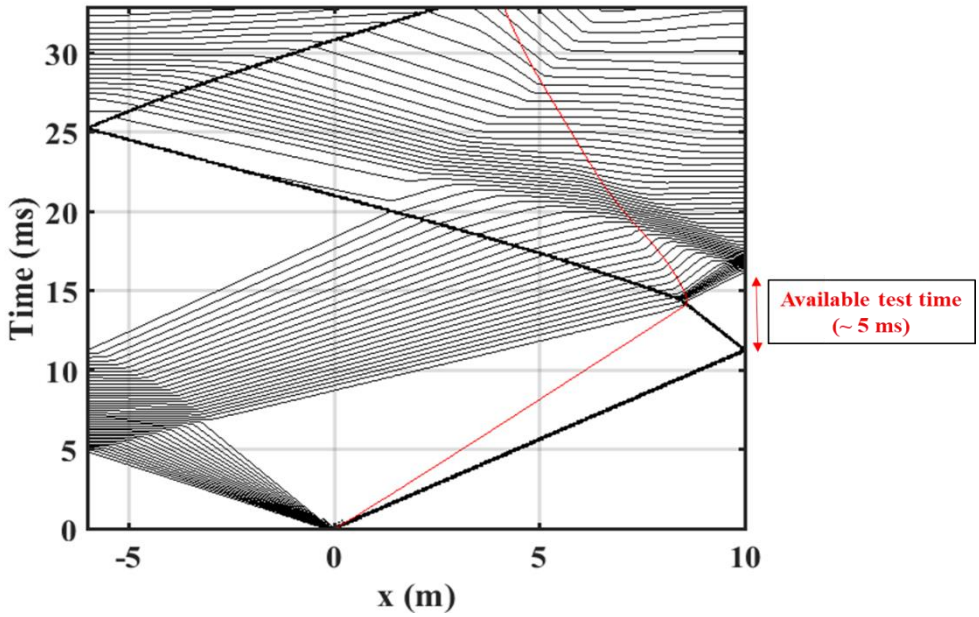

Figure 3.3. x-t diagram for P_5 = 100 bar and T_5 = 1248 K, Mach number = 2.35, driver gas: Helium, driven gas: $CH_4/O_2/Ar$ (3:6:91)

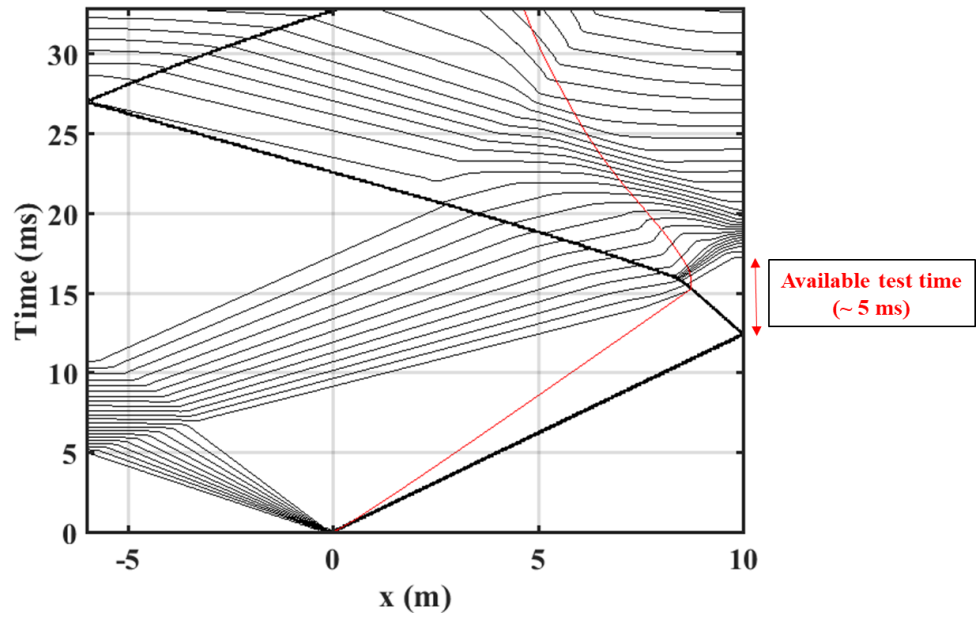

Figure 3.4. x-t diagram for P_5 = 100 bar and T_5 = 1196 K, Mach number = 2.22, driver gas: Helium, driven gas: $H_2/CO/O_2/Ar$ (2.85:0.15:1.5:95.5)

3.2 High-Pressure Shock Tube Facility

Details on the shock tube operation procedures and general design features of the facility are described in details in appendices B and C, respectively, and here brief descriptions of key components are provided. The shock tube used in this study is fabricated out of 316 stainless steel with 15.24 cm inner diameter and a wall thickness of 5.08 cm. The total length of the shock tube is 20 m consisting of a 10 m long driver section and a 10 m long driven section. In this study, the driver was shortened to 6 m for the majority of the experiments. The inner surface of the tube is electro-polished with 0.2 μm surface finish. The shock tube is equipped with six endwall plugs and eight circumferential ports (located 1.24 cm away from the endwall) enabling pressure and optical measurements. The maximum operating pressure of the tube is 376 atm with preheating capability up to 500 K. The shock tube is equipped with a hydraulically operated double-diaphragm ram section and a custom-designed contour valve for quick vacuuming. The test section is clamped into a 2-ton concrete dead mass anchored to the floor to damp out vibrations caused by high-pressure experiments. The key components of each major section of the shock tube is presented herein. The overall schematic of the facility is shown in Figure 3.5.

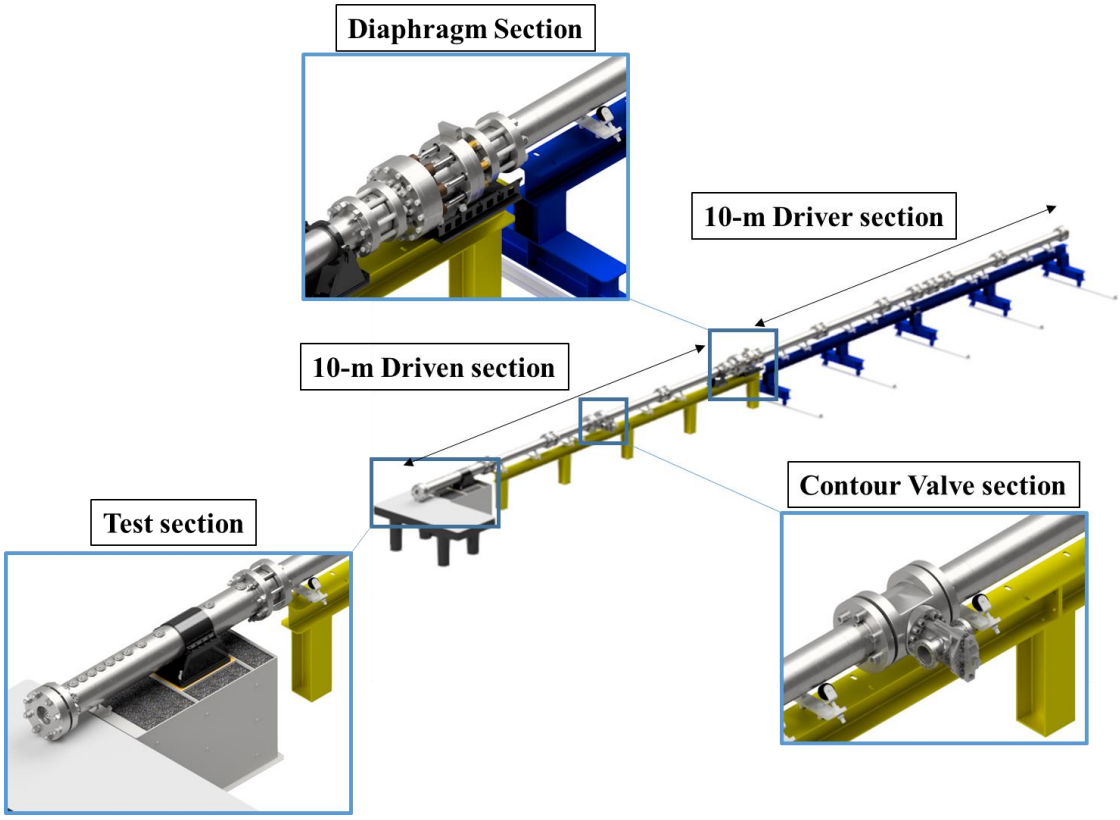

Figure 3.5. Schematic of the shock tube facility

3.2.1 Driver Section

The driver section of the shock tube consists of seven individual open-ended short tubes, giving flexibilities to obtain variable test times. To increase the available test time, the driver section can be extended to a maximum length of 10 meters to delay the arrival of the expansion waves at the measuring location. Standard tube connectors are used to connect these sections of the tube together. Four access ports are used on the driver section of the tube for filling, vacuuming, relieving and static pressure measurements as shown Figure 3.6. The inner diameter of the driver section is 15.24 cm (6 inches) and as shown in this figure.

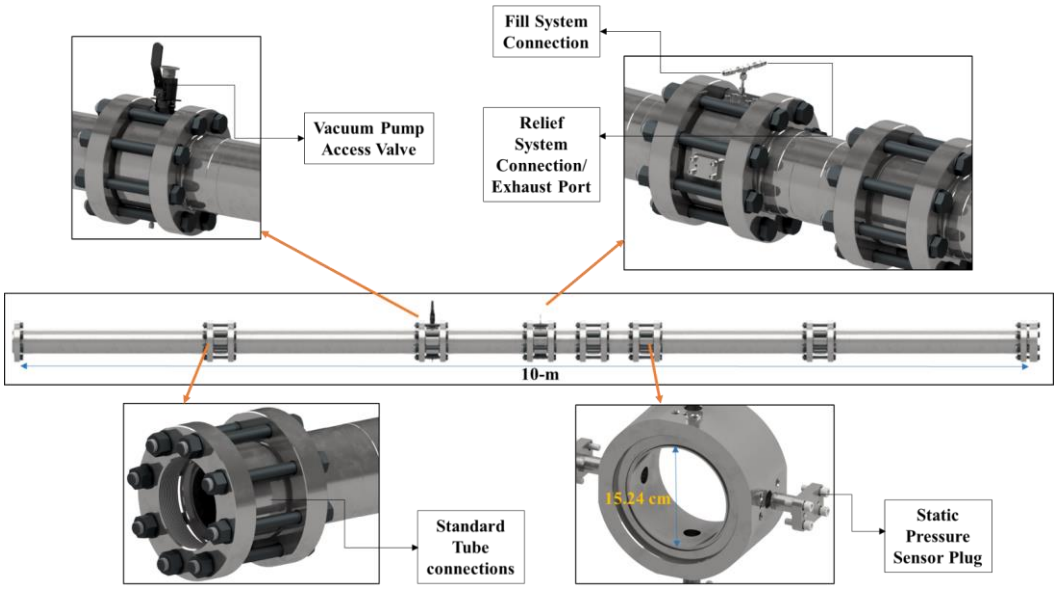

Figure 3.6. Driver section and its associated connections

The fill system for the driver section is designed to have three stages, referred to as slow fill, medium fill, and fast fill (boost tank). This configuration is found to keep the filling rate consistant and repeatable. The slow and medium fills of the tube run on eight packs of helium bottles sitting at maximum pressure of 3,000 psi (~206 bar), where the boost tank is kept at 6,000 psi (~413 bar) and only used for high-pressure experiments (busrt pressure >2,000 psi (~138 bar)). Actuated valves are used in series with manual valves to provide more control on adjusting the fill rate appropriate for each experimental condition. Figure 3.7 and Figure 3.8 show the schematic of such connections and pictures from the actual setup, respectively.

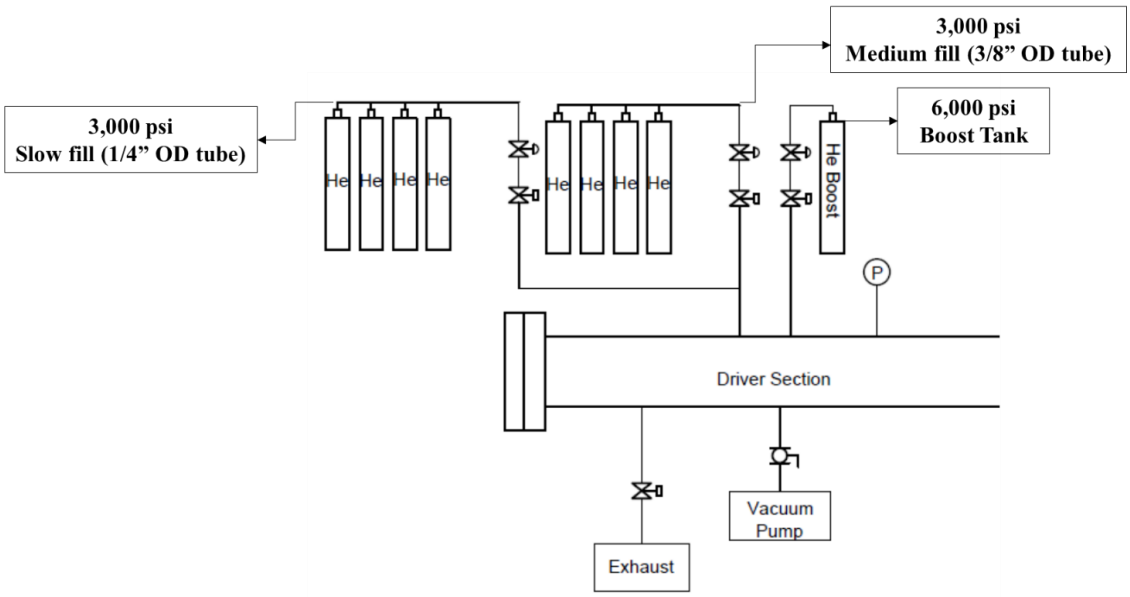

Figure 3.7. Schematic of shock tube fill system

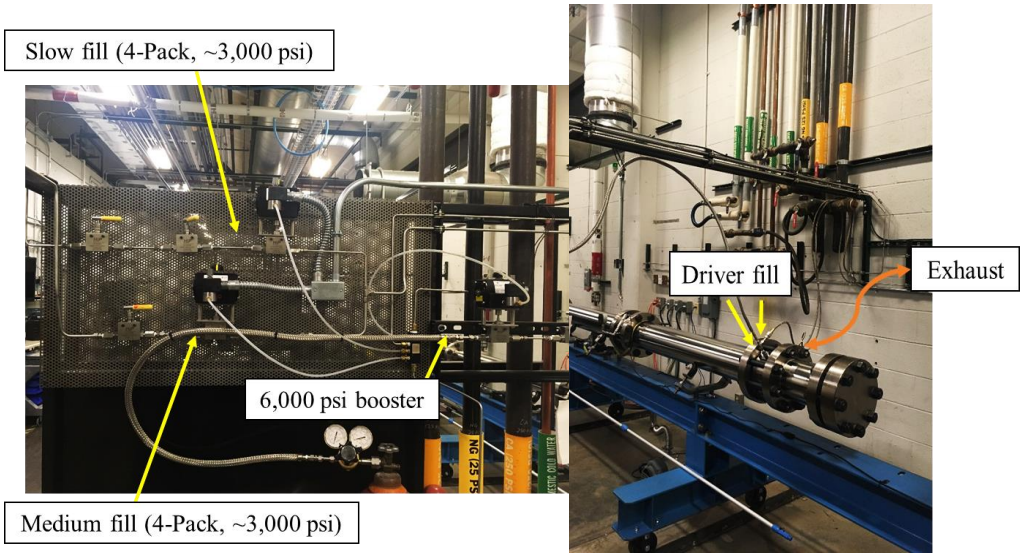

Figure 3.8. Driver fill and exhaust connections

3.2.2 Diaphragm Section

The diaphragm section of the shock tube consists of three components: 1) The transition section from driver to ram section (round to square), 2) The ram section to driven transition (square to round), and 3) The diaphragm holder section with a square cross section of 10.16 cm (4 inches). The schematic of these components could be observed in Figure 3.9. A unique feature of the diaphragm section is that it is capable of operating under single or double diaphragm configuration.

To seal the diaphragm section and keep the diaphragm in place, hydraulic pressure from a reservoir is supplied to the hydraulic fluid chamber plate where eight circumferential springs are installed. The plate is connected to eight tie-nut rods where upon pressurizing the spring-loaded plate, it retracts. Once a constant pressure of 185 bar is applied to the tie-nut rods upon engaging the shear-lock plate, the diaphragm is ensured to be in place and sealed. O-rings installed on either sides of the diaphragm section ensure that there will be no positive or negative leaks across the diaphragm. A picture from the diaphragm section setup and the hydraulic pump system is shown in Figure 3.10.

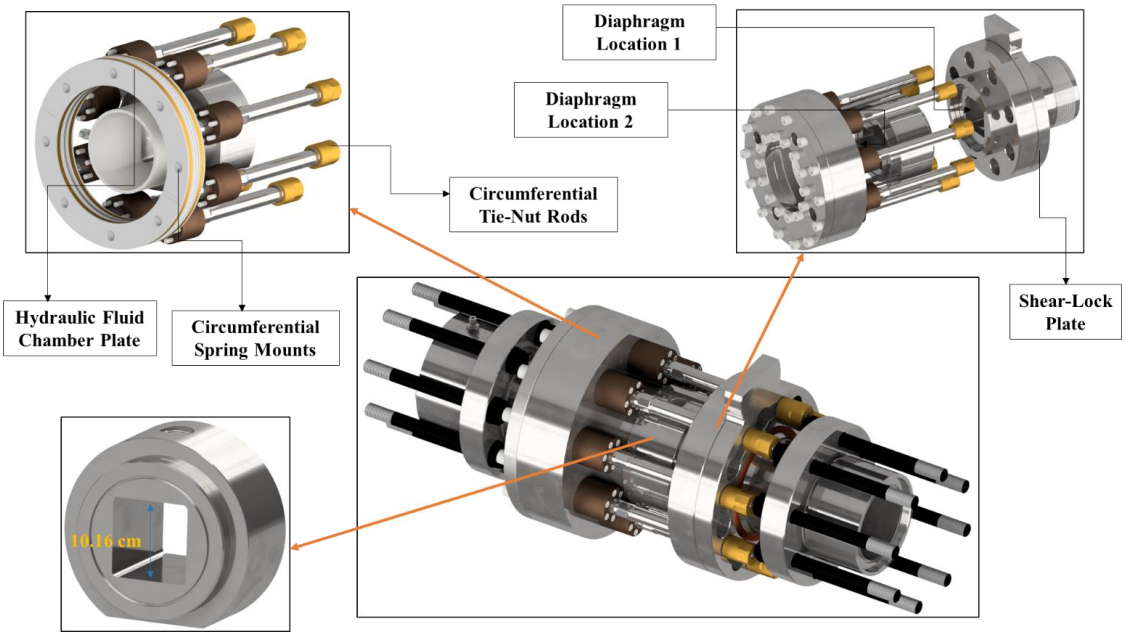

Figure 3.9. Schematic of the diaphragm section

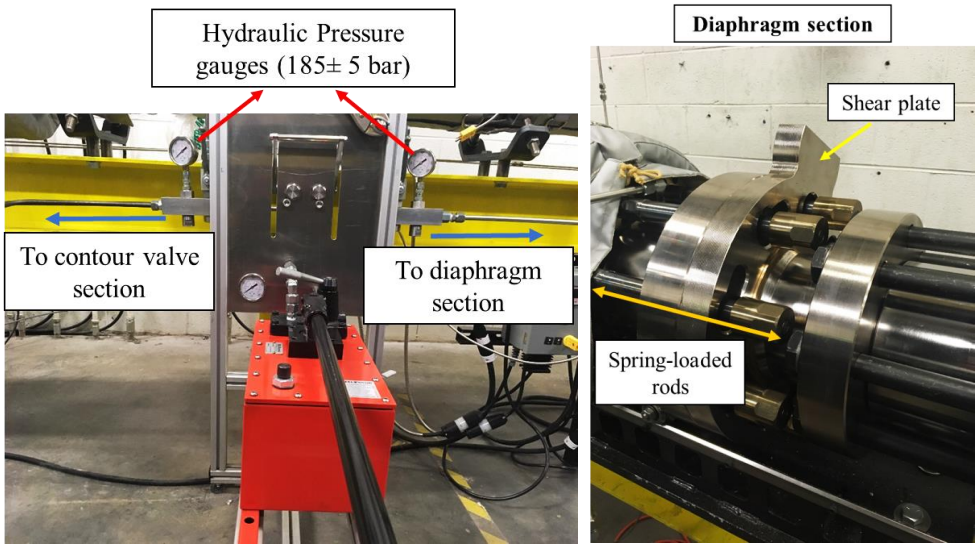

Figure 3.10. Diaphragm section and the hydraulic pump system

The diaphragm selection process is performed based on an iterative approach. Indeed, the burst pressure of the diaphragm is a function of the material type, the thickness, the score depth, shape of the score, and fill rate on the driver section of the shock tube. As was mentioned previously, the fill rate was kept constant for each burst pressure range. However, other parameters for selecting the diaphragms were arbitrary and selected by trial and error approach. For example, for the experimental conditions studied here, two types of materials were selected as aluminum 6061 and stainless steel 316. Once these metal sheets are supplied, they are water jetted to a diameter appropriate for the diaphragm section and then they are pre-scored. The pre-scoring of the diaphragms were done by using an Uncoated Carbide Drill-Point Countersink with 60^0 countersink angle where an X-shape cross was made on the low-pressure face of the diaphragm as could be seen in Figure 3.11a. Figure 3.11b shows the manner on how the diaphragm pedals were opened after an experiment, where a uniform burst was obtained.

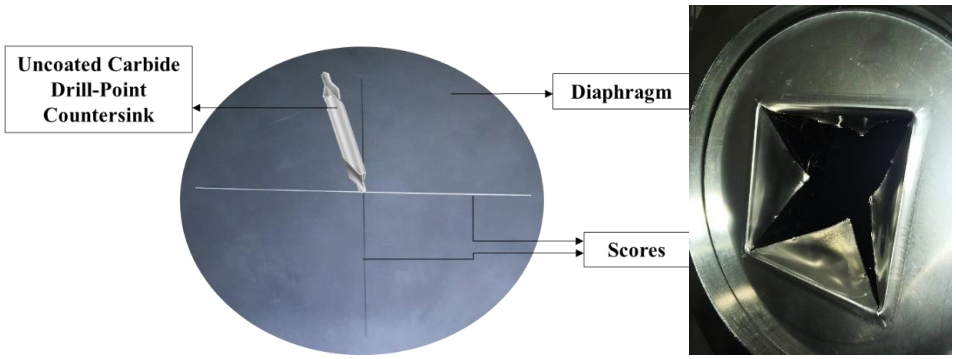

Figure 3.11. a) Unburst pre-scored diaphragm b) Opening pedals of a burst diaphragm

3.2.3 Driven Section

Following the diaphragm section is the driven section of the shock tube. The general design and assembly of the driven section is nearly the same as the driver section. For example, the total length of the driven section is also 10 meters with 15.24 cm (6 inches) internal diameter and the standard tube connectors are utilized to connect various sections of the driven section together. While there are many similarities in the design of the driven section and driver section of the tube, some of the components installed on the driven section of the tube should be described in detail.

One of the unique design features of the shock tube is its custom-designed and hydraulically operated contour as shown in Figure 3.12. A reciprocating piston is utilized to have a quick and easy access to a two-stage vacuum pump system. A large conflat flange (CF 6 with 4 inch OD) is used as a connection to maximize the vacuuming rate. This allows for the driven section to be vacuumed down initially to 10^{-5} bar (0.075 torr) using an Agilent IDP-15 Dry Scroll pump and finally down to 1.33×10^{-9} bar (9.97×10^{-7} torr) using an Agilent TwisTorr 304 FS AG turbo pump in two hours. Figure 3.13 shows a picture from the actual assembly of the driven section of the tube, the contour valve, and the vacuum pump system. As could be seen from this figure and Figure 3.12, the same hydraulic supply and feed system is used for both the diaphragm section and the contour valve. It is also important to note that the valve-acting piston is flush-mounted to the inner surface of the driven section wall upon applying 185 bar of hydraulic pressure. This ensures that the incident shock is not affected by the presence of any objects as it travels towards the test section.

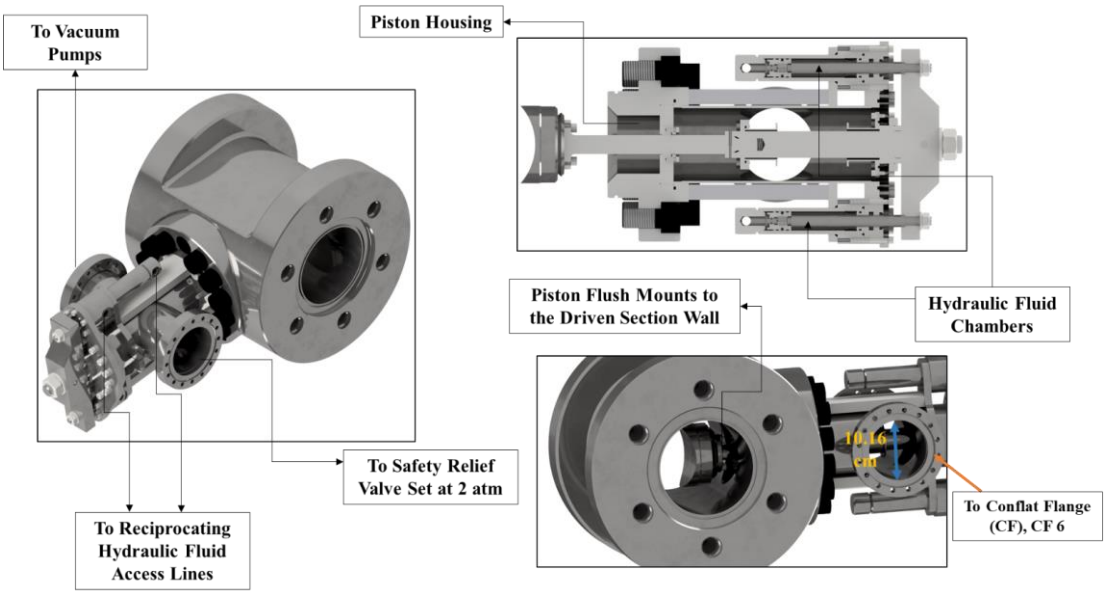

Figure 3.12. Schematic of the custom-designed contour valve

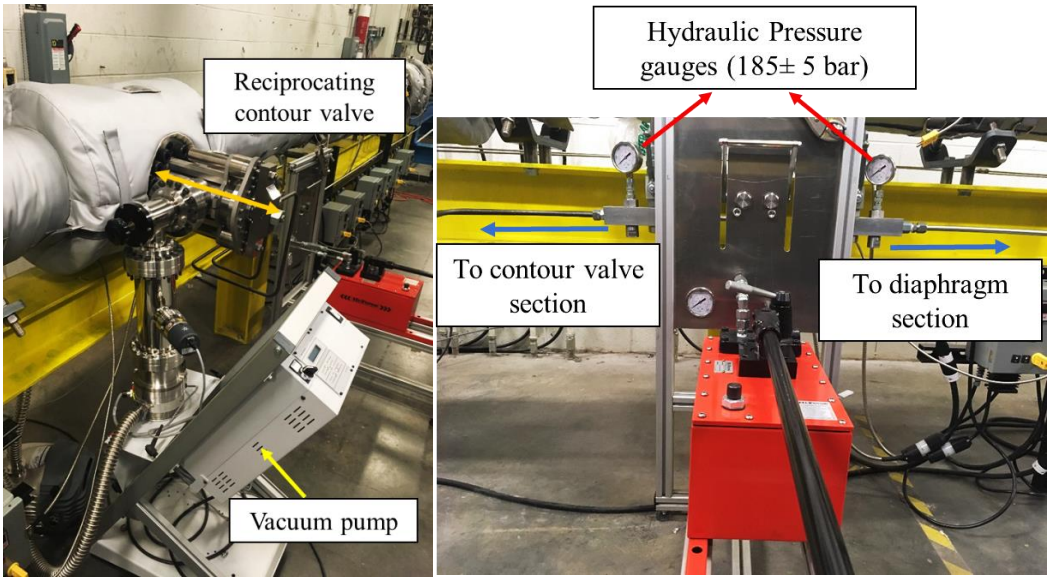

Figure 3.13. Contour valve section and the hydraulic pump system

As was mentioned earlier, the driven section of the tube is capable of reaching a preheat temperature of 500 K. This is achieved by wrapping various sections of the driven section with heating jackets, which are controlled independently. The insulated jackets are controlled by individual and independent temperature feedback controllers to achieve a

uniform temperature profile along the tube. Figure 3.14 shows the heating jackets installed on the driven section along with their temperature controller units.

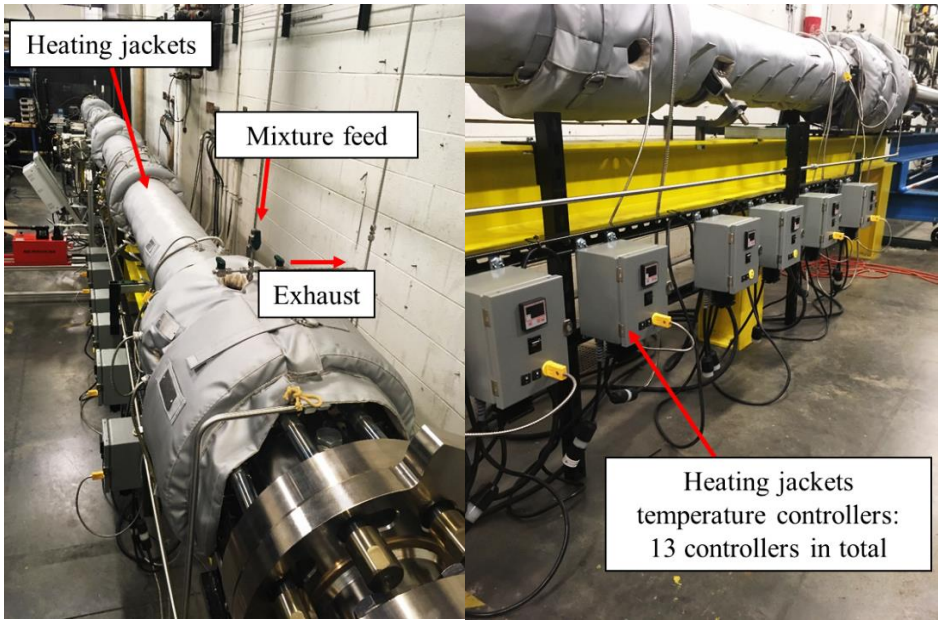

Figure 3.14. Driven section heating jackets and their controllers

The main component of the driven section is the test section, where combustion occurs. Various diagnostics instrumentations and dynamic pressure measurements are implemented in the design of this section. The schematic of the test section is shown in Figure 3.15. As observed from this figure, the test section is 2 meters long and includes eighteen access plugs along the tube as well as the circumferential location. The circumferential plugs are referred here in as “sidewall” plugs. Furthermore, the end of the tube is sealed with “endwall” where six plugs are also located on this section for adding diagnostics and dynamic pressure measurements perpendicular to the flow in the shock tube. The advantages of having such capabilities are highlighted in the subsequent sections of this chapter.

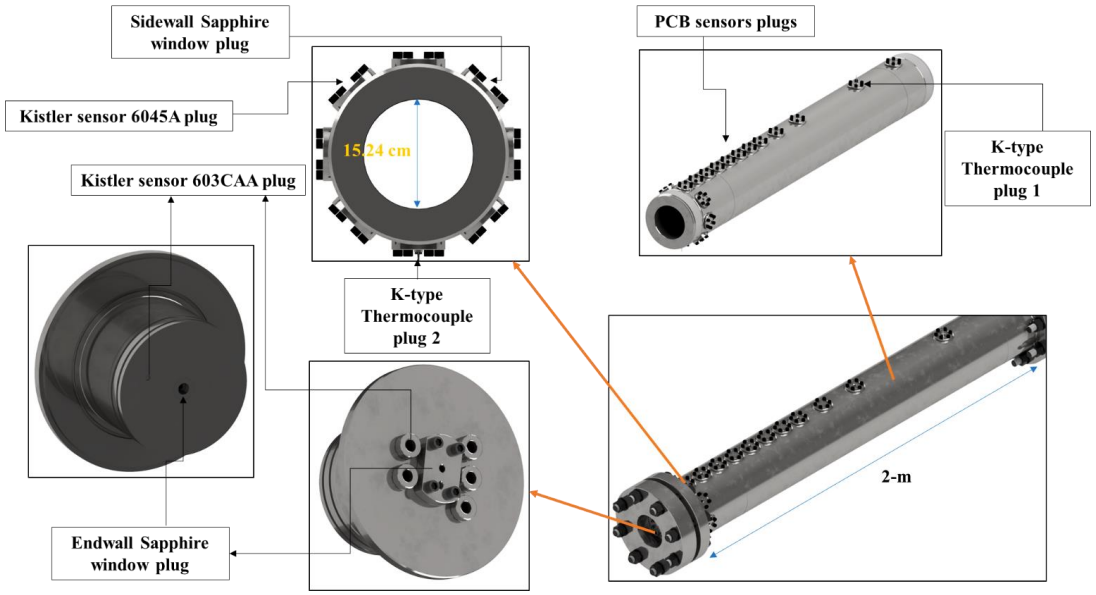

Figure 3.15. Schematic of the test section and its key components

The plugs are custom-made for each individual pressure sensor that is being installed on this section of the tube. The cylindrical sapphire window plugs are also manufactured accordingly where adhesives could be applied. As was observed in Figure 3.15, there are also thermocouple plugs that are used at two locations on the test section. It is important to note that all accessories on the tube, whether it is a dynamic pressure sensor, or a window or a thermocouple, are flush mounted to the inner wall surface of the tube as could be seen schematically in Figure 3.16. This ensures the shock waves in the tube are not perturbed or affected by the presence of any intruded parts of the equipment.

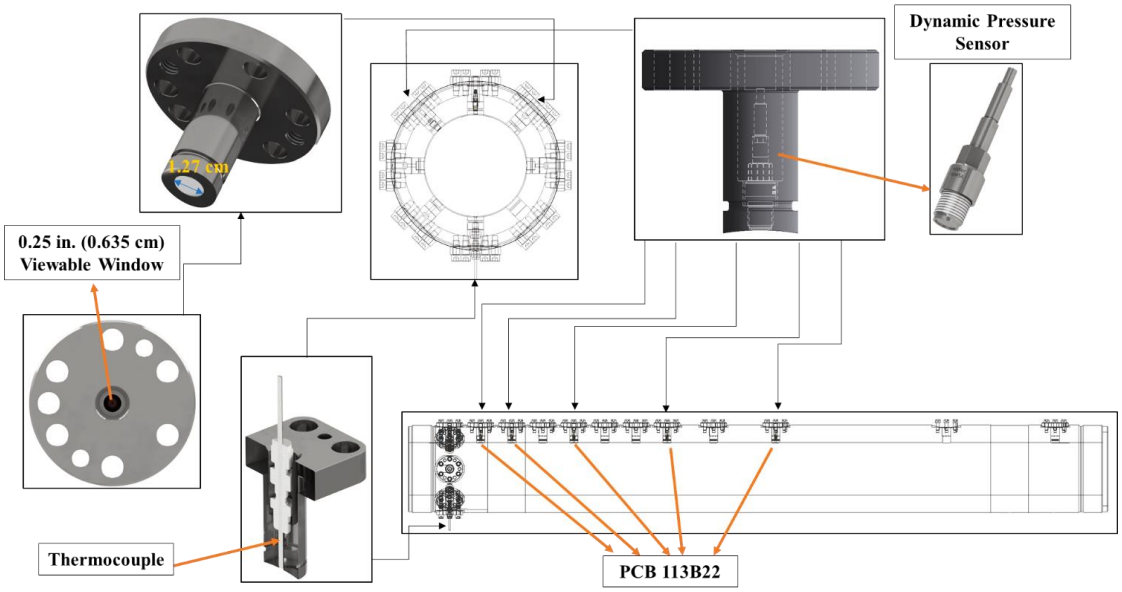

Figure 3.16. Dynamic pressure sensor, sapphire window and thermocouple plug assemblies

There are three types of dynamic pressure transducers used on the shock tube for various purposes. Kistler 6045A and Kistler 603CAA are used to record the pressure time histories of post reflected shock from sidewall and endwall, respectively. The incident shock velocities are measured by PCB 113B22 sensors used for timing purposes upon arrival of the incident shock to the test section. Summary of key features of the dynamic pressure sensors used on the shock tube are listed in Table 3.1.

Table 3.1. Key features of dynamic pressure sensors installed on the shock tube

Key Features	Kistler sensor 6045A [132]	Kistler sensor 603CAA [133]	PCB sensor 113B22 [134]
Measuring range	0–250 bar	0–1000 bar	0–344 bar
Sensitivity	0.1 V/bar	–5.0 pC/bar	2 mV/bar
Response time	< 3.0 µsec	< 0.4 µsec	≤ 1 µsec
Operating temperature range	–20…+350 °C	–196...+200 °C	–73…+135 °C

Further details regarding the instrumentations used on the test section of the tube are shown in Figure 3.17 along with a picture from the actual lab setup. The shock velocity is measured by timing the arrival of the incident shock at 957 mm prior to the endwall using four fast-response PCB 113B22 piezoelectric pressure transducers and four BNC 1105 universal frequency counters with 400 MHz sampling rate. It should be noted that one of the PCB 113B22 sensors is only used for triggering the data acquisition system as the incident shock arrives to the test section. The shock velocity obtained from these sensors is then extrapolated linearly to the endwall to account for shock attenuation. The uncertainty in the shock velocity is found to be approximately ±6 m/s. As was mentioned earlier, the sidewall and endwall pressure histories are recorded by Kistler 6045A PiezoStar and Kistler 603CAA dynamic pressure sensors, respectively. Electronically excited OH radical emission (OH*), used to monitor ignition, is measured using two Hamamatsu H10723-113 photomultipliers (PMT) with band-pass filters centered at 307 nm ±10 nm, and collected from the sidewall and endwall simultaneously. The pressure and emission trace data are collected at 500 kHz sampling rate.

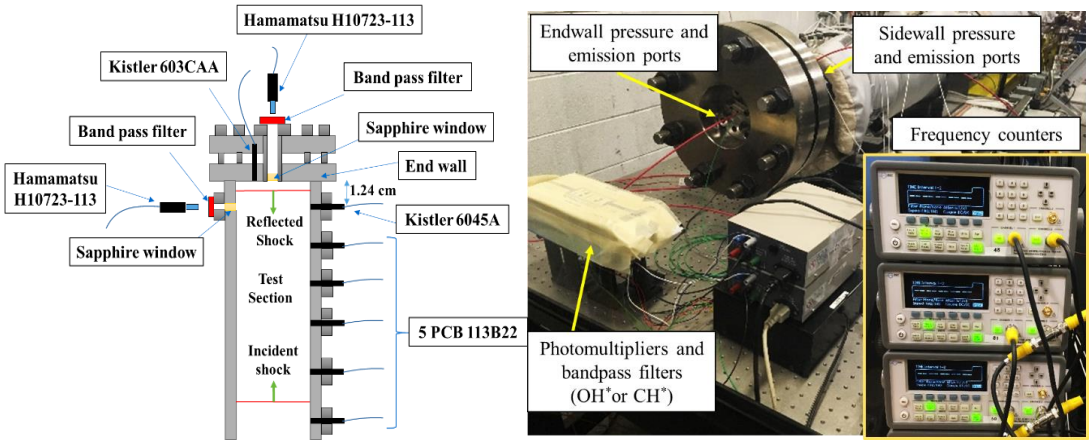

Figure 3.17. Test section schematic and an actual setup picture

3.2.4 Mixing Vessel

The mixture is prepared in a high pressure mixing vessel according to Dalton's law of partial pressure using high purity gases (99.999%) supplied by Airgas. The partial pressures are measured by three high accuracy (0.05%) MKS 960A absolute pressure sensors with ranges of 0.13 bar (100 Torr), 1.33 bar (1,000 Torr) and 13.3 bar (10,000 Torr). The prepared mixture is stirred inside a 13-liter mixing vessel by a magnetic stir for two hours to ensure sufficient mixing is achieved prior to feeding into the driven section. A schematic of the mixing facility and an actual picture from the experimental setup is shown in Figure 3.18. A sample from the mixture is then taken and analyzed by micro gas chromatography (Inficon Fusion) to estimate the uncertainty in the equivalence ratio (Φ). Gas chromatography results revealed a maximum uncertainty of no more than 0.01 in equivalence ratio.

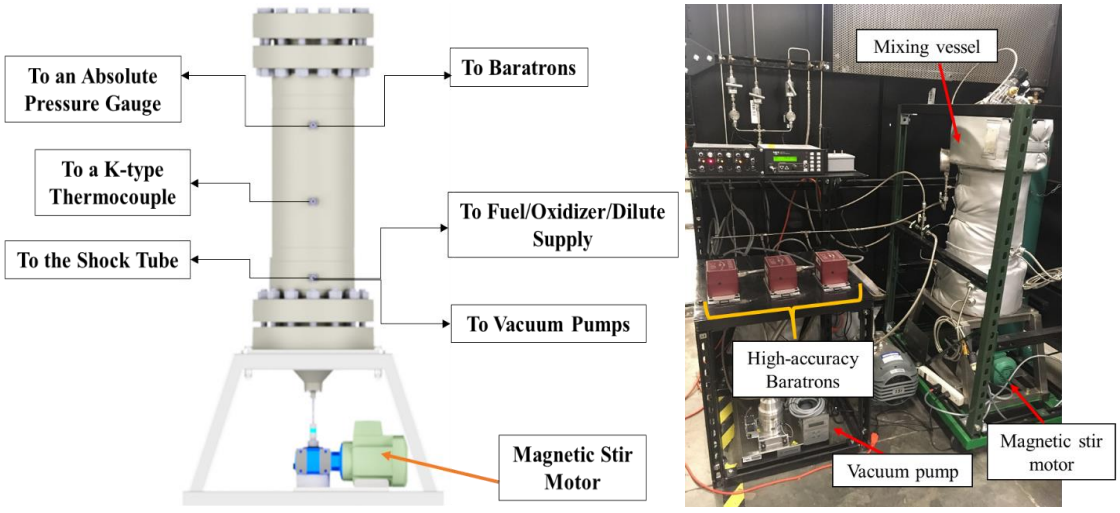

Figure 3.18. Mixing vessel facility

3.3 Shock Tube Facility Performance and Validation

Once the installation of the shock tube was completed, the facility was validated by replicating ignition delay time from a well-known database. For this purpose, the IDT data for a mixture from Stanford university database [135] was targeted. The condition selected for this validation test campaign consists of ignition delay time measurements of a stoichiometric mixture of methane, oxygen and argon mixture (CH_4/O_2/Ar: 2:4:94) at an average pressure of 14 bar and a temperature range of 1308–1765 K. The results are shown in Figure 3.19 and as could be seen in this figure, reasonable agreements are observed. It should be mentioned that a similar methodology (described in the database) was used to obtain such data. For example, sidewall CH* emission signal and sidewall pressure traces were used to report the IDT data.

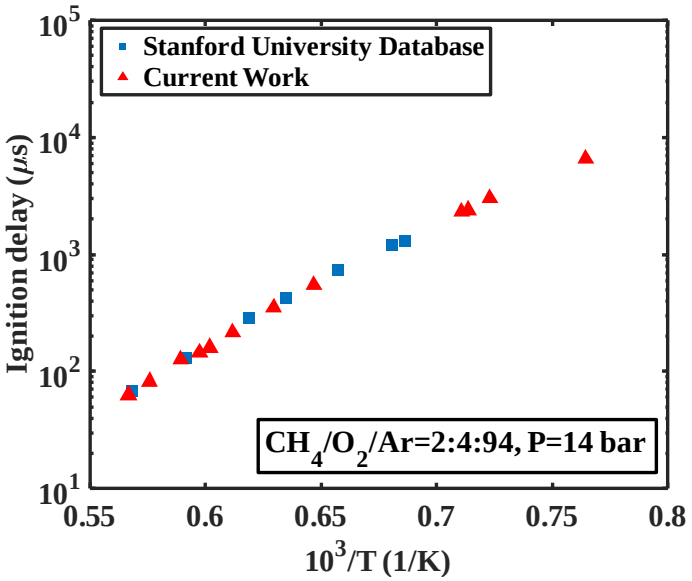

Figure 3.19. Shock tube validation data at an average pressure of 14 bar and a temperature range of 1308–1765 K

Although shock tubes have many similarities in the principles of operations, however their performances could be different. Two metrics are commonly used for evaluating the shock tubes performances. They are driver to driven pressure ratio (also known as compression ratio) (P_4/P_1) versus the achieved incident Mach number (M_s), and incident shock Mach number deceleration as it travels towards the endwall.

For the conditions studied in this thesis, wide ranges of P_4/P_1 ratios were necessary to achieve the required reflected shock pressure (P_5) and temperature (T_5). The burst pressures (P_4) were varied from couple of hundred psi to couple of thousand psi. Therefore, a wide ranges of compression ratio data were collected. On the other hand, the mixture studied in this thesis (Table 3.2) were mainly diluted in high levels of argon or carbon dioxide where Mach numbers near 2 and 4 were required to achieve temperatures above 1,000 K on the reflected shock. Therefore, experiments conducted mainly within these ranges of Mach numbers.

Table 3.2. Mixtures studied in this thesis

Mixture	**Composition**
1	$CH_4/O_2/CO_2$ = 5:10:85
2	$CH_4/O_2/Ar$ = 2:4:94
3	$H_2/CO/O_2/CO_2$ = 2.85:0.15:1.5:95.5
4	$H_2/CO/O_2/Ar$ = 2.85:0.15:1.5:95.5

Using the ideal shock theories [131] and the NIST Reference Fluid Thermodynamic and Transport Properties Database (REFPROP) [15], a plot of P_4/P_1 versus the M_s for the mixtures listed in Table 3.2 could be obtained and the results are shown in Figure 3.20.

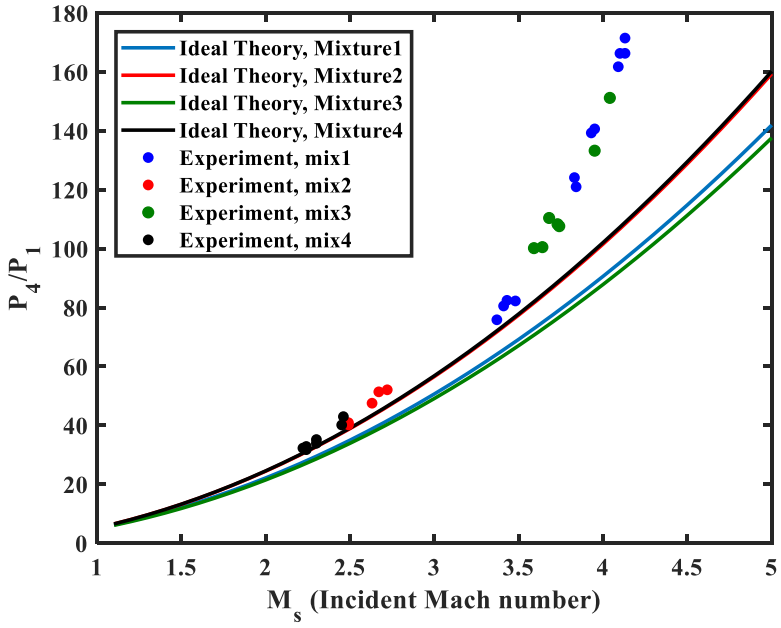

Figure 3.20. Compression ratio versus incident Mach number

As could be seen from this figure, at lower Mach numbers, the experimental data matches the ideal theory very closely. However, as the compression ratio increases, deviation from the ideal theory is observed as the incident Mach number increases. This is due to the non-ideal effects mainly the opening pedals of the diaphragm and incident shock interactions with the wall of the shock tube [136]. As the burst pressure increases, thicker diaphragms are required to withstand the driver pressure, therefore the opening sequence of the diaphragm pedals requires a substantial amount of force and takes a longer time compared to lower burst pressure cases. The maximum deviation from the conditions shown in Figure 3.20, is a factor of 2 from the ideal theory. For shock tubes operating at similar conditions, this value could be as high as a factor of 2.3–2.5 [136]. Two factors could be listed as the main contributions to the improvement of the compression ratio versus the incident Mach number. One is the large diameter of the tube where reduces the interactions between the wall of the tube and the incident shock. Another reason could be

the careful selection of diaphragm parameters. For high pressure experiments, stainless steel 316 diaphragms were used, which due to its material properties for the same burst pressure, the thickness of the diaphragms could be reduced compared to aluminum, for instance. Such feature is shown to improve the burst pressure efficiency as the pedals opening time could be much faster than using relatively softer materials.

Another important parameter for evaluating shock tube performance is the amount of shock attenuation. It was previously shown [136] that the majority (as high as 70%) of incident shock attenuations could be attributed to wall viscous effects. The opening time of the diaphragm pedals could also play a role in increasing shock attenuations. Once the diaphragm is burst and the incident shock is formed (by coalescing many compression waves), it decelerates towards the end of the driven section. The temperature behind the reflected shock is calculated using the incident Mach number, therefore it is important to investigate the amount by which shock decelerates upon arriving to the endwall of the driven section. As was mentioned earlier, four fast-response PCB dynamic pressure sensors are installed along the test section. Using three frequency counters and proper trigger settings, the timing between each PCB sensor could be obtained and knowing the distance between them a velocity value could be obtained as the shock passes by each sensor. Using the velocity value obtained from two intervals, the shock deceleration could be quantified as shown in Figure 3.21. As shown in this figure, the incident shock deceleration is highly linear and the order of deceleration is 0.01 in Mach number at worst case scenarios. Once the incident shock Mach number is linearly extrapolated to the endwall location, temperature on the reflected shock could be calculated. Under the conditions used in this

thesis, the maximum uncertainty in reflected shock temperature (T_5) is estimated as ± 10 K.

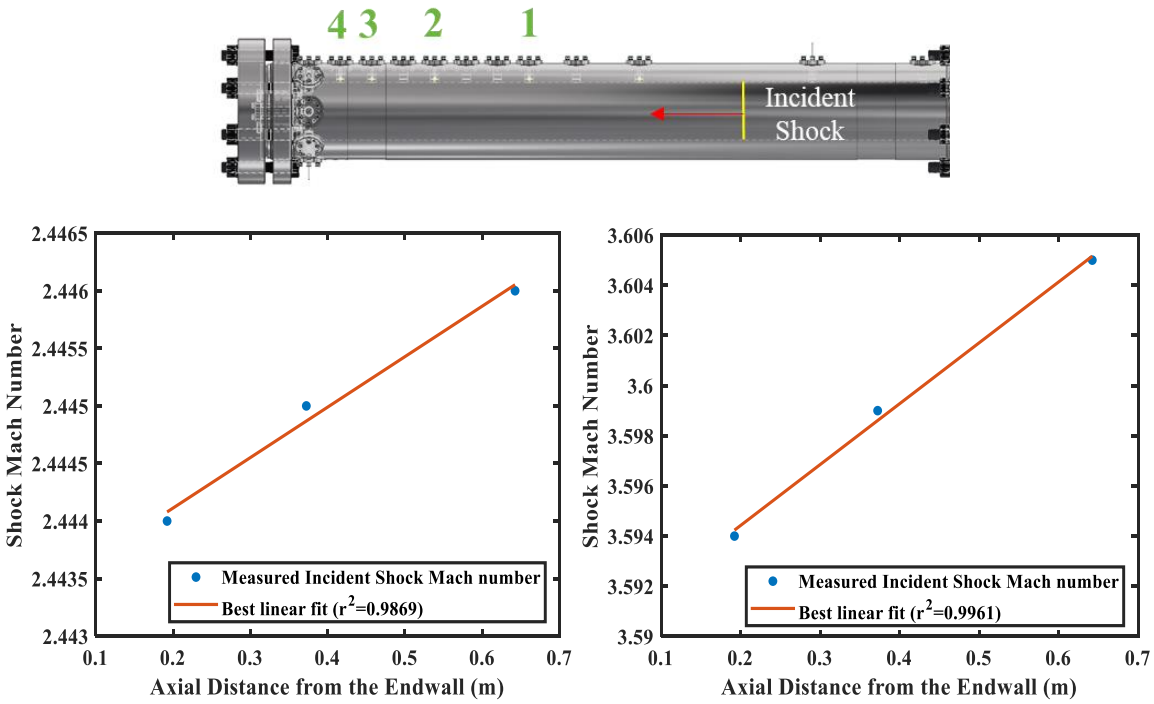

Figure 3.21. Incident shock attenuation examples at M~2.44 and M~3.59

The temperature after the reflected shock (T_5) is calculated from normal shock relations using the obtained shock velocity and normally the ideal equation of state (EoS). However, at elevated pressure, the choice of real gas EoS versus ideal gas EoS for the T_5 calculation needs to be examined in detail beforehand. Since the pressure after the reflected shock (P_5) is as high as 200 bar, the density prediction using the ideal gas EoS may not represent the actual density after the reflected shock. Therefore, it is important to quantify the difference in T_5 calculated using real/ideal gas equations of state. Davidson *et al.* [137] derived and solved normal shock relations by implementing real gas equations of state: Peng-Robinson, Soave, Redlich-Kwong and Van der Waals for pure argon up to 1000 atm and temperatures between 1000–3000 K. It was found that when using the Peng-Robinson

EoS, there was an 83 K/1000 atm difference when compared to an ideal gas. A similar approach is used in this study and showed a minor deviation of ±4 K in T_5 from ideal gas calculations. Therefore, the ideal gas EoS is validated for use in reflected shock temperature calculations for the conditions of the current study. Similar justification was shown by Shao *et al.* [70] in a recent study. In the current study, the maximum uncertainty in the measured shock velocity is found to be ±6 m/s owing to shock attenuation. Using the ideal gas EoS, this value translates into an uncertainty range of ±10 K in T_5, which is included in the total uncertainty analysis of the IDT.

3.4 Simultaneous Sidewall and Endwall Pressure and Emission Measurements and Uncertainties

When diatomic or polyatomic gases are used as diluents, the wall viscous effects (e.g. the thickness of the boundary layer) become significantly more noticeable. As the normal shock travels through the boundary layer developed behind the incident shock, the momentum of the reflected shock is reduced near the wall [69]. As a result, the normal portion of the shock wave in the boundary layer turns into a λ-shaped shock near these regions [69], a phenomenon referred to as shock bifurcation. Pryor *et al.* [65], Koroglu *et al*. [68], Hargis and Petersen [69] and Shao *et al.* [70] all reported the same phenomena while measuring IDTs of methane under highly diluted CO_2 environments. Whether or not the bifurcation of the reflected shock is significant depends on the Mach number of the incident shock, gas composition, and the interaction between the boundary layer and the reflected shock [125]. Moreover, in shock tubes, approximately 70% (or more) of the total shock attenuation is caused by viscous effects at the wall [138]. A recent study from Hargis and Petersen [139] showed the significance of the boundary layer effect for gas mixtures

with CO_2, Ar and N_2 dilution. The study reported that the thickness of the boundary layer is approximately 30 mm in a N_2/CO_2 mixture at 1400 K and 1.83 bar after 600 µs. Therefore, in similar shock tube experiments, the sidewall pressure trace could be contaminated. Another deleterious consequence of the reflected shock-boundary layer interaction is an observed pressure rise after the passage of the reflected shock (i.e. dP_5/dt). While shock tubes are meant to provide a chemically ideal environment (constant P_5 and T_5 to the point of ignition), the change in pressure (and consequently temperature) is not ideal, but inevitable. In the study conducted by Hargis and Petersen [139], dP_5/dt for Ar, N_2, and N_2/CO_2 mixtures were measured for a temperature range of 1400–1800 K and pressure of 1.73 atm. The measured pressure rise for highly diluted carbon dioxide mixtures was reported to be an order of magnitude larger than mixtures with pure argon (18.2%/ms vs. 0.4%/ms). In the current work, dP_5/dt derived from sidewall pressure measurements is between 15–18%/ms as demonstrated in Figure 3.22a, which shows examples of sidewall and endwall pressure and OH* emission traces. Correspondingly, the value from endwall traces is between 3–5%/ms for a 5:10:85 mixture of $CH_4/O_2/CO_2$. During the analysis process, the obtained endwall pressure rise over time is simulated in CHEMKIN-PRO [140] for an unbiased comparison between experimental and numerical results. The pressure rise over time (dP_5/dt) was modeled in CHEMKIN-PRO [140] by applying a time-dependent pressure fit using linear regression of the endwall pressure trace. This technique is commonly adopted, as reported by Hong *et al.* [123] and Hargis and Petersen [139] to obtain a pressure profile of the reflected shock for kinetics analysis.

When there is significant shock bifurcation, the sidewall pressure traces are affected by viscous effects simply due to the formation of the boundary layer behind the incident shock. Therefore, extracting information regarding the exact arrival time of the reflected shock to the measuring location becomes questionable. For instance, the uncertainty in reporting the arrival of the reflected shock at the sidewall measuring port is approximately 50 µs in Figure 3.22. Therefore, when CO_2 diluent is used, a shock tube with a large diameter and endwall pressure traces are desired to minimize the boundary layer effects. Figure 3.22 demonstrates the benefits of endwall pressure measurements. The exact arrival time of the reflected shock could be detected with a step change in the pressure signal with no sign of bifurcation present.

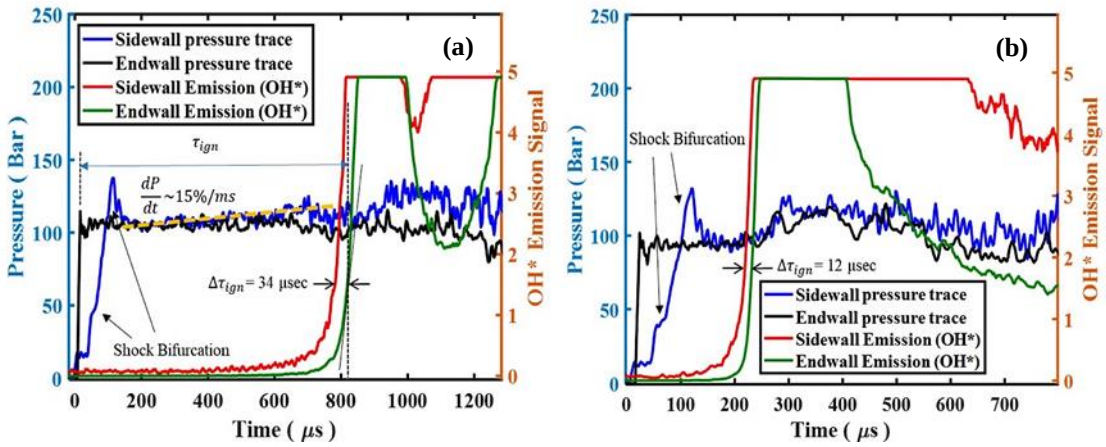

Figure 3.22. An example of simultaneous sidewall and endwall pressures and OH* emission traces for $CH_4/O_2/CO_2$=5:10:85 at 100 bar and temperature: a) 1274 K and b) 1433 K

To determine the occurrence of autoignition, OH* chemiluminescence is recorded from both sidewall and endwall throughout all experiments. The use of sidewall and endwall OH* emissions as a proper ignition marker has been previously studied and validated for a variety of experimental conditions [43, 117, 141-145]. Hargis and Petersen

[69] suggested that in experiments conducted under non-dilute mixtures, in their case 5% CH_4, the endwall diagnostics should be used to report IDTs. Having fuel concentrations ≥ 2% in the current study, the ignition delay time (τ_{ign}) is defined as the time difference between the arrival of the reflected shock at the endwall and the maximum slope of endwall OH*, as demonstrated in Figure 3.22a.

One concern in measuring IDT is the homogeneity of the autoignition event, especially at low temperature conditions, owing to the long autoignition delays. Due to the adverse pressure gradient (with respect to the direction of the reflected shock) present in regions with shock bifurcation near the wall, the entrainment of fluid at the bifurcation foot contributes to the growth of the triple-shock structure and consequently the mixing of fluids in these regions is enhanced [146]. Furthermore, the numerical and experimental results by Yamashita *et al.* [147] show that the temperature rise at the triple point of the λ-shock is significantly larger at the center of the reflected shock wave. Therefore, it is likely that ignition kernels may form in these hot spots, hence the sidewall emission shows a smaller τ_{ign} than the endwall as seen from Figure 3.22a ($\Delta\tau_{ign}$=34 μs). This difference reduces to 12 μs as the reflected shock temperature rises to 1433 K, suggesting a more homogenous-like ignition across the whole cross-section of the tube (as shown in Figure 3.22b).

To study the effect of bifurcation on the homogeneity of ignition, pressure and emission traces obtained from experiments conducted in an argon bath were compared with the CO_2 case. Due to the monatomic structure of argon, the boundary layer that develops behind the incident shock is significantly thinner compared to the case of CO_2. Therefore, bifurcation is minimized when using Ar as diluent. Figure 3.23 shows pressure traces recorded from experiments at pressure conditions near 100 bar in argon. Unlike the

pressure traces in Figure 3.22a, no substantial signs of bifurcation (pressure overshoot or breakage of the normal shock into pieces) are observed in this figure. The arrival of the reflected shock at the measuring port could easily be determined even from the sidewall pressure sensor with a sharp rise in the signal. The time difference between the sidewall and endwall onset of maximum rate of change of OH* decreases as the temperature increases, as shown in Figure 3.23. Another striking difference between Figure 3.22 and Figure 3.23 is the pressure fluctuations. Clearly, the pressure fluctuation in the CO_2 diluent case is significantly larger. This is most likely due to fluid motion and vorticity from the bifurcated shock region. A similar observation was reported by Hargis and Peterson [69].

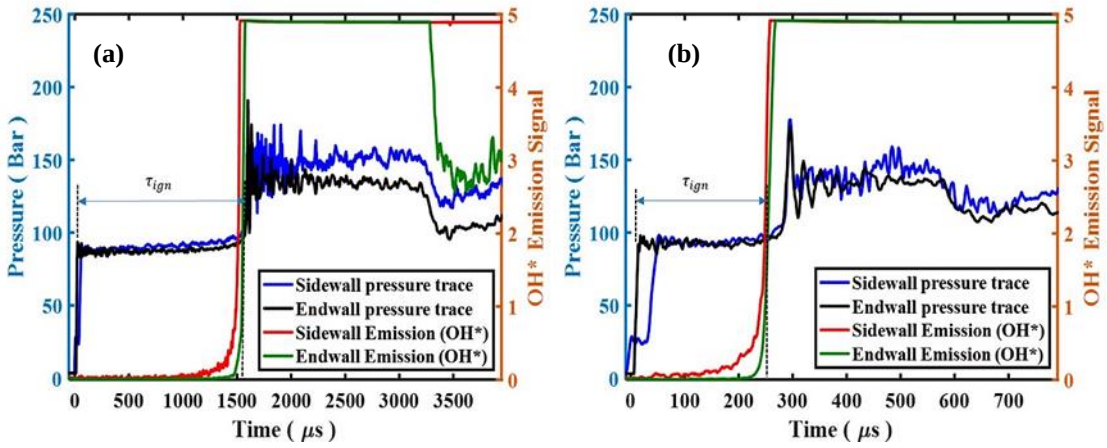

Figure 3.23. An example of simultaneous sidewall and endwall pressure and OH* emission traces for $CH_4/O_2/Ar$=3:6:91 at 100 bar and temperature: a) 1248 K and b) 1410 K

It is clear that temperature and bath gas type both can affect ignition homogeneity. Focusing on the temperature effect, it is observed that increasing the temperature improves the homogeneity. This trend is obvious in Figure 3.22 and Figure 3.23 by noticing smaller $\Delta\tau_{ign}$ as the temperature raises. Studying the bath gas effect suggests that experiments with CO_2 could favor inhomogeneous ignition. The 34-μs time difference between the sidewall

and endwall OH^* emissions for mixtures with CO_2 at 1274 K is 4.4% of reported IDT. At a similar temperature, $\Delta\tau_{ign}$ for the argon experiment is 46 μs which is 3% of reported IDT. At 1433 K this time difference between emissions is 5.8% for CO_2 experiments and 2.5% for argon experiments. Therefore, regardless of the temperature range, the existence of significant bifurcation induces larger uncertainty in the measured ignition delay. Similar trends regarding the homogeneity of ignition and shock bifurcation phenomena is observed for experiments conducted at 200 bar for CH_4 as could be observed in Figure 3.24 and Figure 3.25. While the endwall emission is used to report a single ignition delay as recommended by Petersen [145], the value obtained from the sidewall was taken into account in the uncertainty analysis. For experiments involving methane as a fuel, the overall uncertainty in ignition delay is estimated to be ±15–18%. The IDT uncertainty is estimated using 2σ probability. For methane mixtures, uncertainty in the reflected shock temperature due to shock attenuation (±11–14% in ignition time), pressure fluctuation due to non-ideal gas dynamics (±3% in ignition time) and uncertainty in the mixture composition (±1% in ignition time) all contribute to the total IDT uncertainty. The actual value for each case is used to form error bars in τ_{ign} plots in Chapter 4. At similar experimental conditions involving high CO_2 dilution levels, Shao *et al.* [70] reported ±25% uncertainty in reporting individual IDT data points.

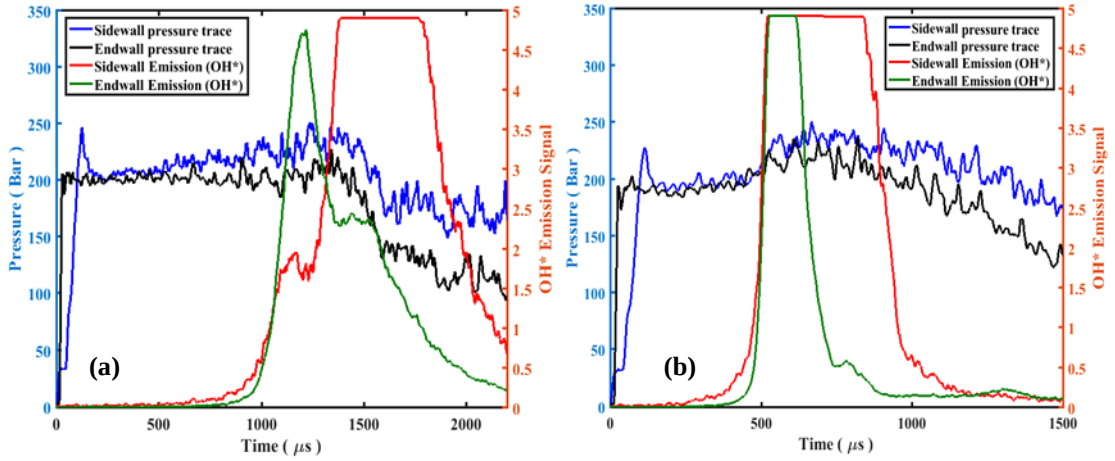

Figure 3.24. An example of simultaneous sidewall and endwall pressures and OH* emission traces for $CH_4/O_2/CO_2$=5:10:85 at 200 bar and temperature: a) 1139 K and b) 1250 K

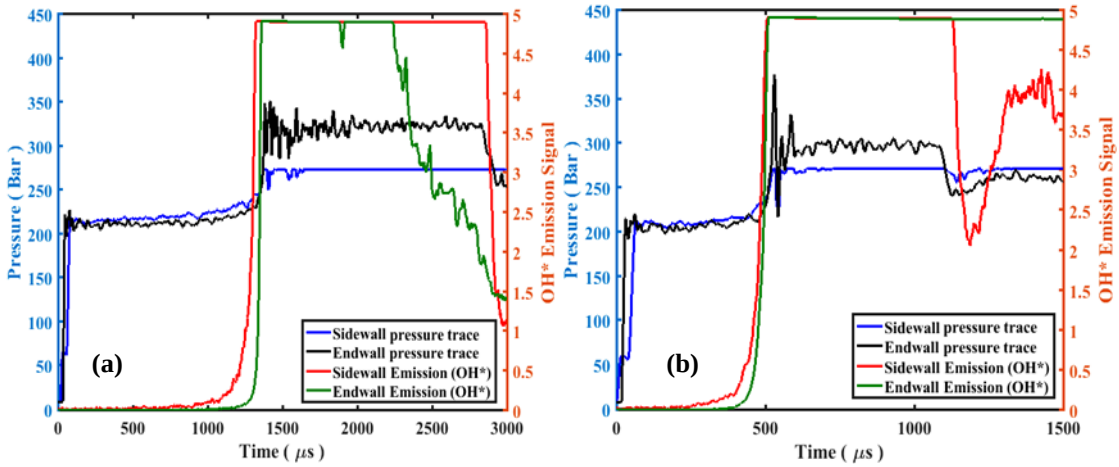

Figure 3.25. An example of simultaneous sidewall and endwall pressures and OH* emission traces for $CH_4/O_2/Ar$=2:4:94 at 200 bar and temperature: a) 1253 K and b) 1379 K

The effect of reflected shock bifurcation could also be observed when the fuel was changed from methane to a syngas mixture of 95% H_2 and 5% CO. Figure 3.26 and Figure 3.27 show the pressure traces obtained for this mixture under large dilution levels of CO_2 and Ar respectively at pressures near 100 and 200 bar. The presence of reflected shock bifurcation is obvious from Figure 3.26, where defining time zero from sidewall pressure

traces is challenging and could induce large uncertainties in reporting IDTs. However, the endwall pressure trace is used as was mentioned earlier to define time zero to overcome this issue similar to the methane case. However, one major difference compared to the methane results is the shape of the OH* emission signals. As was mentioned earlier, due to the temperature values being higher near the foot of the bifurcated regions, the sidewall emissions show a larger gradient in their signals than the enwall emission. However, since extrapolation of the maximum gradient to the baseline technique [75, 86, 87, 148] is used to define ignition time, the reported IDTs using either sidewall or endwall emission signals lead to nearly identical values. Nevertheless, the small percentage of the delay between the signals are taken into account for the uncertainty analyses.

As CO_2 is replaced by Ar, the OH* emission traces coalesce due to a more homogenous temperature distribution across the tube. Also, a more homogenous-type ignition is observed regardless of the reflected shock temperature. This could be seen from Figure 3.27 where two traces of the syngas mixture at approximately 100 bar are shown at 1196 K and 1275 K. The IDT uncertainty is estimated using 2σ probability. Uncertainty in the reflected shock temperature due to shock attenuation (±12–15% in ignition time), pressure fluctuation due to non-ideal gas dynamics (±3% in ignition time) and uncertainty in the mixture composition (±2 % in ignition time) all contribute to the total IDT uncertainty, which is found to be 20% (at maximum) for syngas mixtures. The actual value for each case is used to form error bars in τ_{ign} plots in the experimental results presented in Chapter 5.

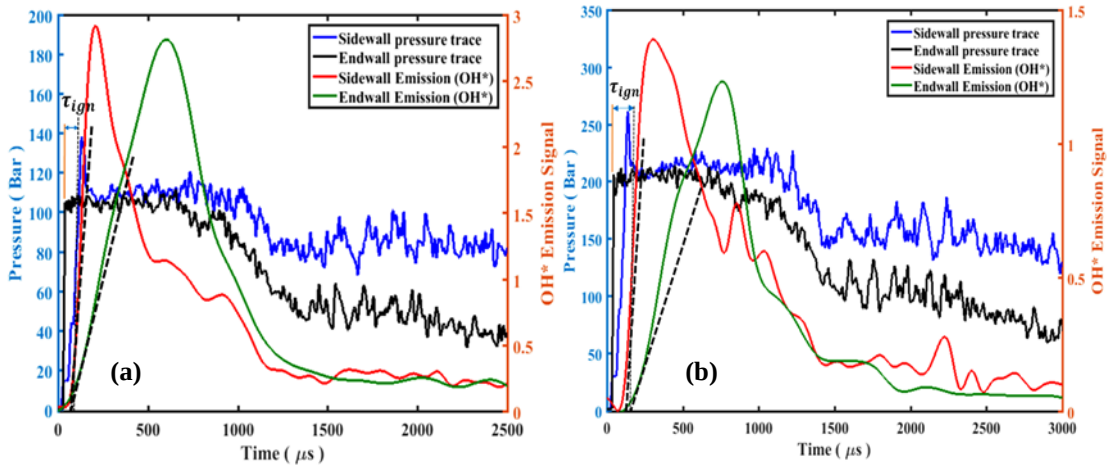

Figure 3.26. An example of simultaneous sidewall and endwall pressures and OH* emission traces for $H_2/CO/O_2/CO_2$=2.85:0.15:1.5:95.5 at a) 100 bar and 1365 K and b) 200 bar and 1257 K

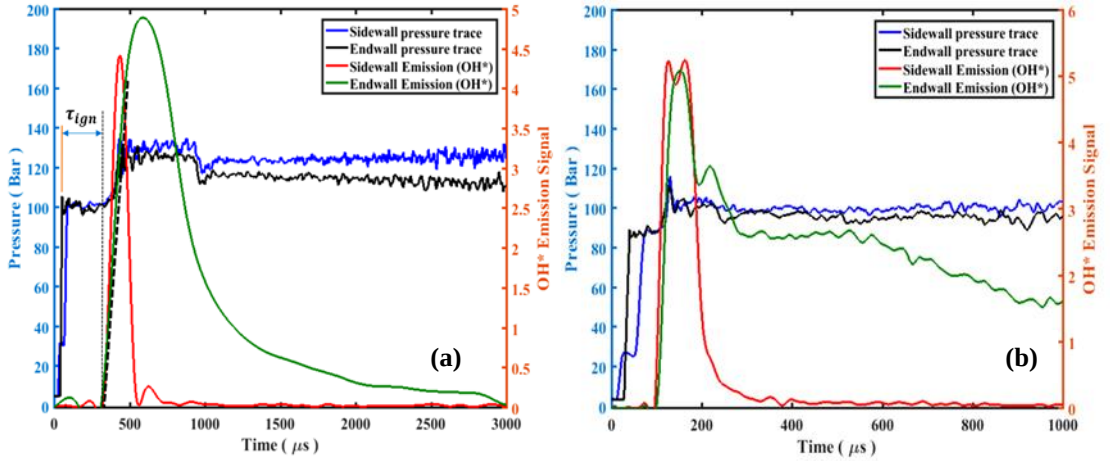

Figure 3.27. An example of simultaneous sidewall and endwall pressures and OH* emission traces for $H_2/CO/O_2/Ar$=2.85:0.15:1.5:95.5 at 100 bar and temperature: a) 1196 K and b) 1275 K

CHAPTER 4. Methane Results and Discussions

4.1 Autoignition of $CH_4/O_2/CO_2$ Mixtures

The results and discussions presented in this chapter have been published in journal of combustion and flame (Karimi *et al.* [149]). Measurements of autoignition delays for $CH_4/O_2/CO_2$ and CH_4/O_2/Ar mixtures are presented and discussed in this section. Further details of the experimental conditions and measured IDTs are provided in appendix A. Experimental results are also compared to simulations using different chemical kinetic models including USC Mech II [26], Aramco 2.0 [28-34], GRI 3.0 [24], HP-Mech [25] and FFCM-1 [27].

The experimental conditions (P_5 and T_5) for the study are targeted to be above the critical points of the mixtures. Therefore, the critical temperatures (T_{crit}) and critical pressures (P_{crit}) of the mixtures are calculated using NIST Reference Fluid Thermodynamic and Transport Properties Database (REFPROP) [15] prior to conducting experiments. Table 4.1 shows the T_{crit} and P_{crit} for all the mixtures in the study along with the conditions where the IDTs were measured.

Table 4.1. Ignition delay test conditions and critical points

Experimental cases	Reactant mole fractions				Conditions		Critical points	
	CH_4	O_2	CO_2	Ar	T_5 (K)	P_5 (bar)	T_{crit} (K)	P_{crit} (bar)
1	5	10	85	0	1274–1433	94–109	295.01	93.95
2	10	10	80	0	1297–1383	96–101	298.98	95.96
3	3	6	0	91	1248–1410	90–97	152.22	49.4
4	5	10	85	0	1139–1250	195–212	295.01	93.95
5	2	4	0	94	1253–1379	210–214	151.72	49.17

As observed in Table 4.1, the thermodynamic conditions for this study are above the critical points of the test mixtures. Therefore, real gas effects on the autoignition delay should be investigated. Kogekar *et al.* [150] developed, a constant-volume, adiabatic reactor model incorporating a real gas EoS and non-unity activity coefficient (or fugacity) of different species to represent the departure from ideality. The non-unity activity coefficients of different species were accounted for when defining the rate of progress for a reversible reaction from mass-action kinetics. They used this model to simulate the post-reflected shock conditions for supercritical n-dodecane/O_2/N_2 mixtures for pressures up to 80 atm and temperatures between 774–1163 K. Simulation results predicting IDTs using the ideal gas EoS and a real gas (Redlich-Kwong (R-K) [150, 151]) EoS were compared to experimental results. For temperatures below 1100 K, the deviation between the experimental results and simulations using the ideal gas EoS was non-trivial due to large corrections needed for density calculations. Implementing the R-K EoS into thermodynamics and kinetics provided a better IDT prediction at elevated pressure and low temperatures (T<1100 K). In this study, a similar method was utilized to evaluate the real gas effect on predicting IDTs. In this approach, the R-K EoS is used for pressure,

temperature, specific volume, and thermodynamic calculations. Figure 4.1(a) and (b) show IDTs calculated using Aramco 2.0 and FFCM-1 using the ideal gas EoS and Redlich-Kwong EoS, respectively, for a mixture of $CH_4/O_2/CO_2$=5:10:85 at 100 and 200 bar. The "a" (Van der Waals attraction parameter) and "b" (repulsive volume correction parameter) coefficients in the R-K EoS for different species were adapted from Kogekar *et al.* [150] and Redlich *et al.*[151]. As shown in Figure 4.1, the difference in IDT predictions using the real gas (R-K) EoS and the ideal gas EoS becomes larger as the pressure is doubled for the same mixture and same temperature range. However, for the experimental conditions in this study, the maximum deviations in IDTs using the real gas EoS and the ideal gas EoS are less than 5%. The uncertainty of the IDTs reported experimentally is between 15–18%; therefore the choice of EoS for validation purposes of different kinetics models based on experimental data is not critical.

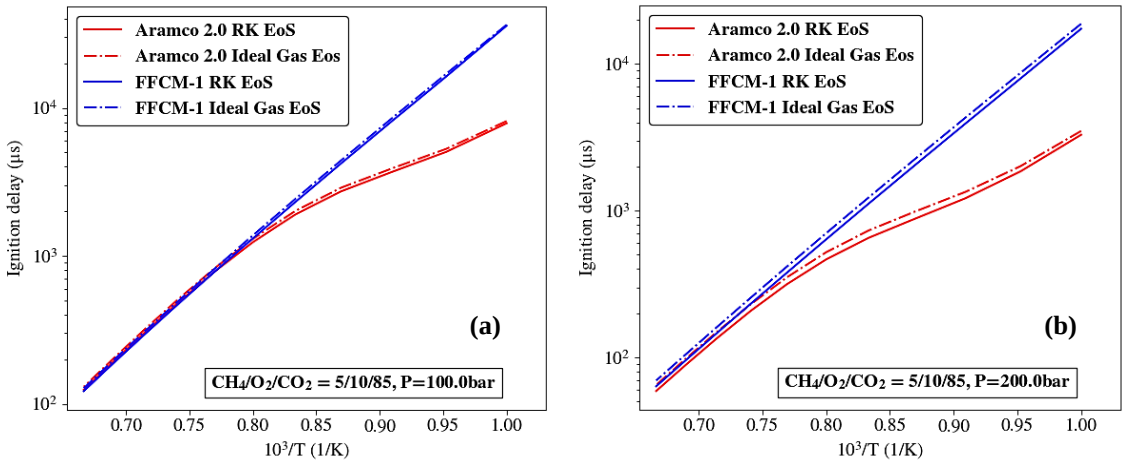

Figure 4.1. Real gas EoS and ideal gas EoS effects on chemical kinetics models for $CH_4/O_2/CO_2$=5:10:85 at a) 100 bar and b) 200 bar

The compressibility factors (calculated by REFPROP [15]) for the mixtures used in this study are listed in Table 4.2 as a reference. It can be seen that the compressibility

factors are all very close to 1, suggesting that the ideal gas EoS is a reasonable choice for the current work. Therefore, the ideal gas EoS is used in CHEMKIN-PRO [140] and CANTERA [152] for the calculations reported in the following sections.

Table 4.2. Compressibility factors (Z) of the mixtures

Experimental cases	Reactant mole fractions				Conditions		Compressibility Factor (Z)
	CH_4	O_2	CO_2	Ar	T (K)	P (bar)	
1	5	10	85	0	1274	100	1.0246
2	10	10	80	0	1297	100	1.0248
3	3	6	0	91	1248	100	1.0221
4	5	10	85	0	1139	200	1.0503
5	2	4	0	94	1253	200	1.0441

The IDTs for $CH_4/O_2/CO_2$ mixtures at stoichiometric and fuel-rich conditions (Φ=2) measured at 100 bar and at temperatures between 1274 –1433 K are shown in Figure 4.2. The predicted IDTs from different kinetic models are compared with experimental values. The simulation results herein are obtained by solving a zero-dimensional reactor with constant internal energy and volume using CHEMKIN-PRO [140]. While USC Mech II, Aramco 2.0, HP-Mech and FFCM-1 are able to predict IDTs within the uncertainty of the experimental data, GRI 3.0 underpredicts the autoignition delay by a factor of 3.

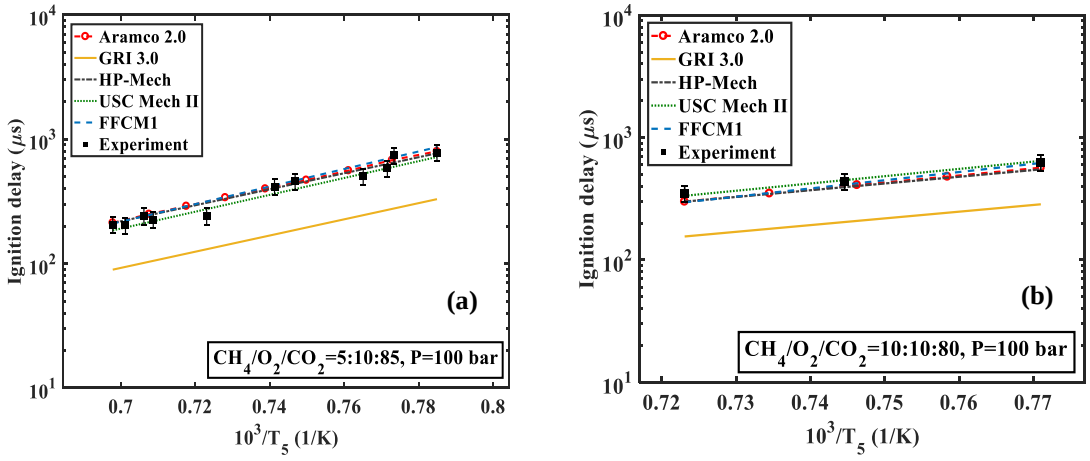

Figure 4.2. Ignition delay time of $CH_4/O_2/CO_2$ at 100 bar for (a): stoichiometric (Φ =1), T=1274–1433 K (b): rich (Φ =2) mixtures, T=1297–1383 K

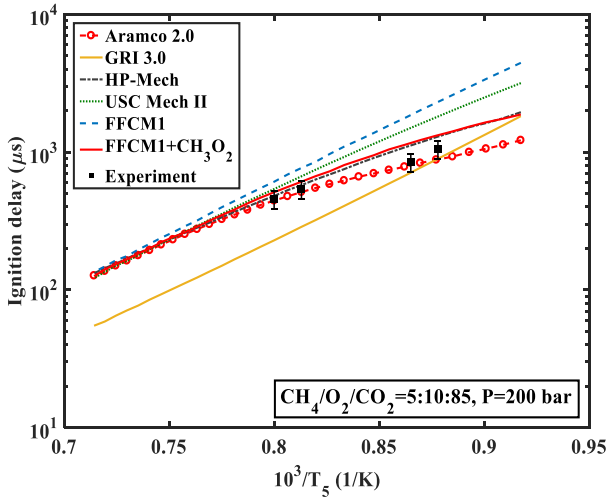

Figure 4.3. Ignition delay time measurements of stoichiometric $CH_4/O_2/CO_2$ mixtures at 200 bar, T=1139–1250 K

Figure 4.3 summarizes the results obtained from 200 bar experiments for a 5:10:85 mixture of $CH_4/O_2/CO_2$. At temperatures less than 1250 K, the deviation in IDT predicted by different kinetic models grows while at higher temperature ranges, all kinetic models except for GRI 3.0 converge. As shown in Figure 4.3, the experimental data show very good agreement with IDT predictions from Aramco 2.0 for a temperature range of 1139 to

1250 K. HP-Mech also gives a reasonable prediction to the experimental data. FFCM-1, on the other hand, overpredicts the ignition delay at these conditions by approximately a factor of 2.5. GRI 3.0 still fails to predict the ignition trend at 200 bar, having a maximum deviation of approximately 3 times faster ignition delay.

To better understand the behavior of different kinetic models, an autoignition delay sensitivity analysis for FFCM-1, Aramco 2.0 and GRI 3.0 was conducted in CANTERA [152] using the normalized sensitivity coefficient of $\frac{k_i}{\tau}\frac{\partial \tau}{\partial k_i}$. The results are summarized in Figure 4.4, Figure 4.5 and Figure 4.6 for temperature of 1200 K and 100 and 200 bar pressures.

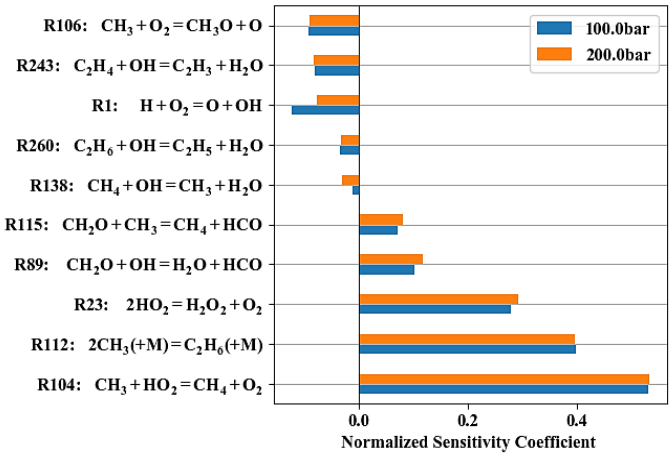

Figure 4.4. Sensitivity analysis of IDT at 1200 K, 100 and 200 bar using FFCM-1

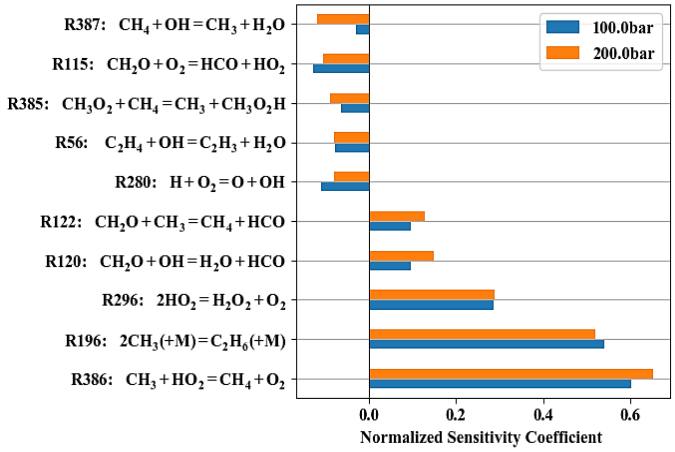

Figure 4.5. Sensitivity analysis of IDT at 1200 K, 100 and 200 bar using Aramco 2.0

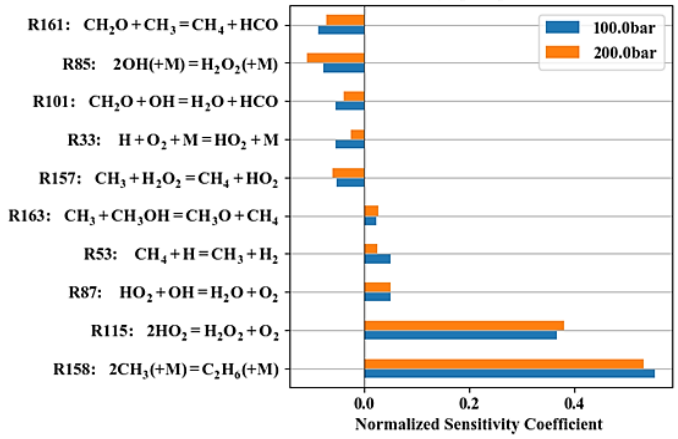

Figure 4.6. Sensitivity analysis of IDT at 1200 K, 100 and 200 bar using GRI 3.0

All three kinetic models show that autoignition is very sensitive to the reactions $2CH_3 (+M) = C_2H_6 (+M)$ and $2HO_2 = H_2O_2+O_2$. Both Aramco 2.0 and FFCM-1 predict that autoignition is most sensitive to the reaction $CH_3+HO_2 = CH_4+O_2$. However, this reaction was not picked up by GRI 3.0, as the rate constant of this reaction in GRI 3.0 is much smaller than the value used in Aramco 2.0 or FFCM-1. This might be one of the reasons why GRI 3.0 predicts much faster autoignition than the other models. Different from FFCM-1 and GRI 3.0 results, Aramco 2.0 predicts that reaction $CH_3O_2+CH_4=CH_3+CH_3O_2H$ could significantly accelerate autoignition. Note that CH_3O_2

is not included in the FFCM-1 and GRI 3.0 results. Even though the sensitivity analysis identified a few reactions which influence autoignition, it is still not clear what about GRI 3.0's underlying kinetic mechanism produces shorter IDTs; nor is it clear why predictions from the other models diverge at low temperature, as observed in the experiments.

To further investigate the reaction pathway predicted by the different kinetic models, a reaction pathway flux analysis is conducted. This analysis produces the ratio of carbon flux through different reaction pathways using a Global Pathway Selection (GPS) method [153] in CANTERA [152]. The results for $CH_4/O_2/CO_2$ (5:10:85) at 1200 K and for 100 and 200 bar are shown in Figure 4.7 and Figure 4.8, respectively.

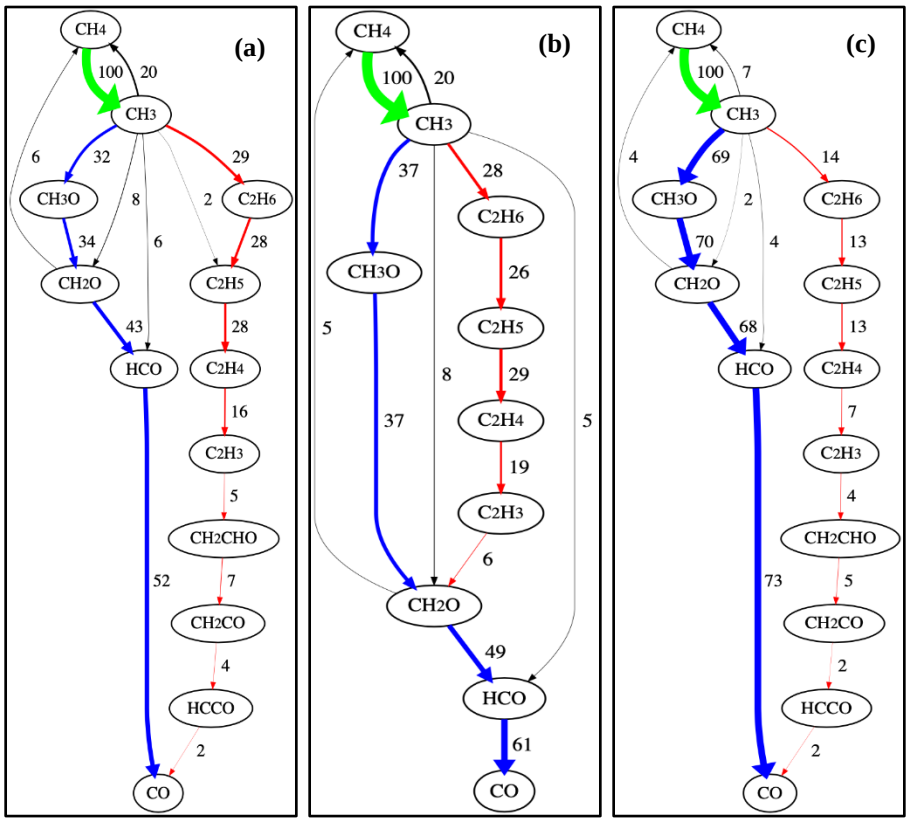

Figure 4.7. Reaction pathway flux analysis for $CH_4/O_2/CO_2$ (5:10:85) at 1200 K and 100 bar using (a) Aramco 2.0 (b) FFCM-1 and (c) GRI 3.0

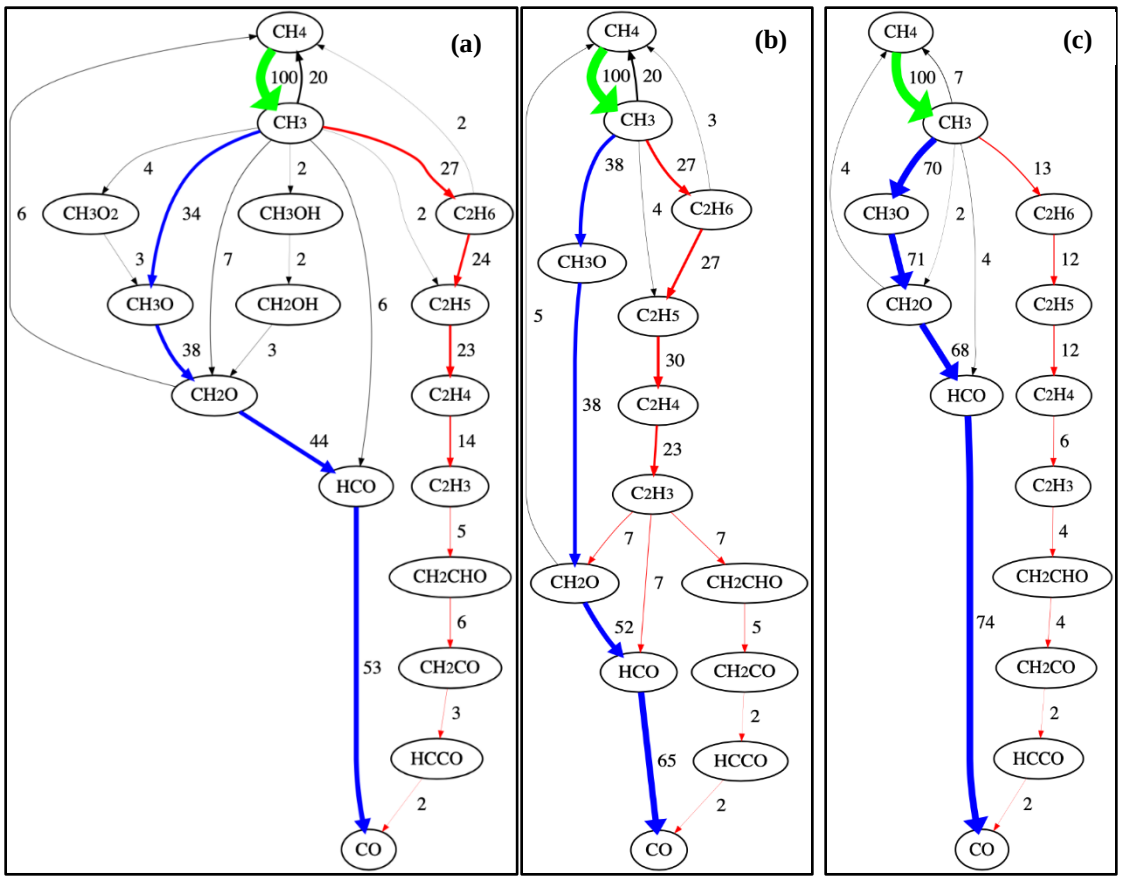

Figure 4.8. Reaction path flux results for $CH_4/O_2/CO_2$=5:10:85 at 1200 K and 200 bar using (a) Aramco 2.0 (b) FFCM-1 and (c) GRI 3.0

The numbers shown in Figure 4.7 and Figure 4.8 represent the percentage of carbon flux (normalized by the total carbon flux of the fuel, CH_4 in this study) through various pathways. The cut-off time for these analyses is the time when ignition occurred. At 100 bar, after the initiation reaction of CH_4 to form CH_3 (methyl radical), there exist two major reaction pathways of CH_3. One is CH_3 oxidation which is through:

$$CH_3 \rightarrow CH_3O \rightarrow CH_2O \rightarrow HCO \rightarrow CO \quad (1)$$

The second reaction pathway of CH_3 is recombination to form ethane (C_2H_6). Tracking this pathway to the formation of CO at 100 bar, pathway (2) for Aramco 2.0, pathways (2–4) for FFCM-1 and pathway (2) for GRI 3.0 are observed as follows:

$$CH_3 \rightarrow C_2H_6 \rightarrow C_2H_5 \rightarrow C_2H_4 \rightarrow C_2H_3 \rightarrow CH_2CHO \rightarrow CH_2CO \rightarrow HCCO \rightarrow CO \quad (2)$$

$$CH_3 \rightarrow C_2H_6 \rightarrow C_2H_5 \rightarrow C_2H_4 \rightarrow C_2H_3 \rightarrow HCO \rightarrow CO \quad (3)$$

$$CH_3 \rightarrow C_2H_6 \rightarrow C_2H_5 \rightarrow C_2H_4 \rightarrow C_2H_3 \rightarrow CH_2O \rightarrow HCO \rightarrow CO \quad (4)$$

The flux ratio between the CH_3 oxidation and recombination pathways (i.e. $CH_3 \rightarrow CH_3O$ and $CH_3 \rightarrow C_2H_6$) at 100 bar for Aramco 2.0, FFCM-1 and GRI 3.0 are 1.10, 1.30 and 4.93, respectively. The significantly larger CH_3 oxidation flux ratio explains why GRI 3.0 predicts a much faster autoignition than other two kinetics models. This observation also explains why Aramco 2.0 and FFCM-1 have similar predictions, which agree with experimental measurements but GRI 3.0 predicts much shorter IDTs.

At 200 bar, reaction pathway (1) remains the most dominant reaction pathway for all three kinetic models. Pathway (2) also remains the second most dominant pathway for Aramco 2.0, GRI 3.0 and FFCM-1. However, two additional CH_3 reaction pathways are predicted by Aramco 2.0: formation of CH_3O_2 and CH_3OH, which could accelerate autoignition. The experimental data for $CH_4/O_2/CO_2$ mixtures at 200 bar show a unique trend that is only captured by Aramco 2.0. As observed from Figure 4.3, this kinetic model shows a different trend for low and high temperatures. This unique trend is investigated in detail below. The ignition behavior predicted by Aramco 2.0 at 200 bar for the $CH_4/O_2/CO_2$ mixture suggests a strong temperature dependency, especially at lower temperatures. Therefore, the sensitivity analysis at 1100 K and 1400 K (the lowest and highest temperature range of the study) is conducted further, and the results are shown in Figure 4.9 and Figure 4.10.

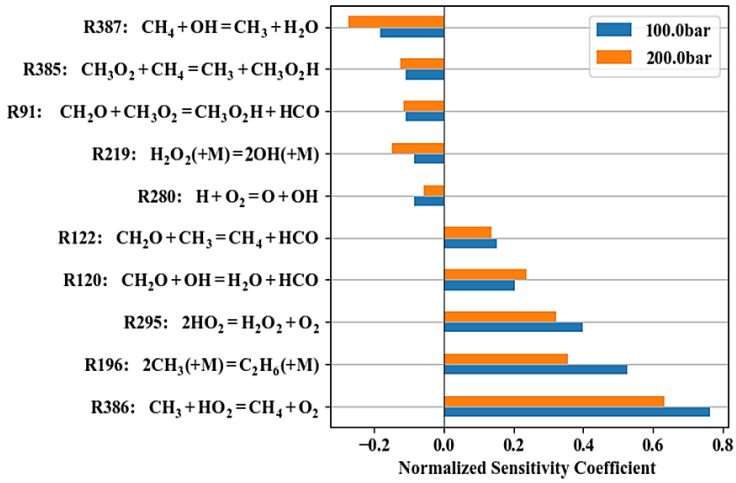

Figure 4.9. Sensitivity of IDT for $CH_4/O_2/CO_2$ mixtures at 1100 K, 100 and 200 bar using Aramco 2.0

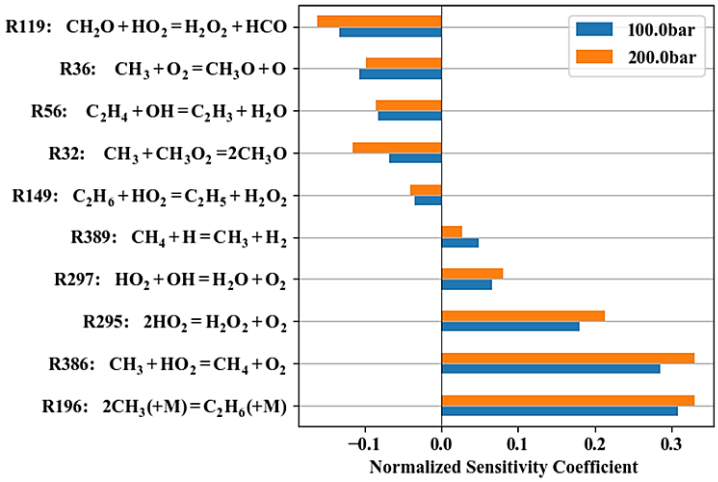

Figure 4.10. Sensitivity of IDT for $CH_4/O_2/CO_2$ mixtures at 1400 K, 100 and 200 bar using Aramco 2.0

A distinct difference is observed in the reactions that promote ignition at the two different temperatures. One major difference is the reactions of CH_3O_2 with CH_2O and CH_4, which accelerate oxidation, and therefore promote ignition at 1100 K. At 1400 K, the reaction of CH_3O_2 with CH_3 to form CH_3O becomes relevant for autoignition, and the importance of this reaction increases with pressure. Interestingly, the sensitivity analysis performed by Shao *et al.* [70] using FFCM-1 also showed the importance of CH_3O_2 to

ignition, while this species is not actually included in FFCM-1. It can be concluded from the sensitivity and path flux analysis results, that the CH_3O_2/CH_3OH kinetics accounts for the unique ignition behavior predicted by Aramco 2.0 at low temperature, 200 bar conditions. To further verify the effect of CH_3O_2 in predicting ignition delays at various temperatures, simulations were performed using an improved version of FFCM-1 with the addition of CH_3O_2/CH_3OH kinetics [154]. The results are also presented in Figure 4.3. It can be seen that the improved version of FFCM-1 with CH_3O_2/CH_3OH addition matches the experiments well. The reaction pathway of CH_3O_2 is presented in Figure 4.11 as a reference. At high pressure and lower temperature conditions, CH_3 recombines with O_2 to form CH_3O_2, which then oxidizes CH_4 and CH_3 and accelerates ignition. The existence of CH_3O_2 kinetics explains why a distinct feature of IDTs was observed in both experiments and simulation.

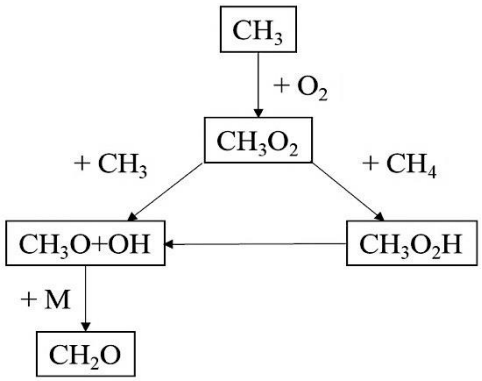

Figure 4.11. Path flux analysis of CH_3O_2 at 200 bar and 1200 K

4.2 Autoignition of $CH_4/O_2/Ar$ Mixtures

While the sensitivity and reaction path flux analyses provide details on ignition chemistry, the question of whether CO_2 alters methane oxidation at elevated pressures compared to an inert bath gas is yet to be answered. To understand the chemical role of CO_2 on ignition, experiments at 100 and 200 bar were conducted in an inert bath gas (in this case argon) at conditions similar to mixtures where only carbon dioxide is present. Figure 4.12 and Figure 4.13 summarize the experimentally measured IDTs of $CH_4/O_2/Ar$ mixtures along with simulations using different chemical kinetics models at 100 bar ($CH_4/O_2/Ar$=3/6/91) and 200 bar ($CH_4/O_2/Ar$=2/4/94), respectively.

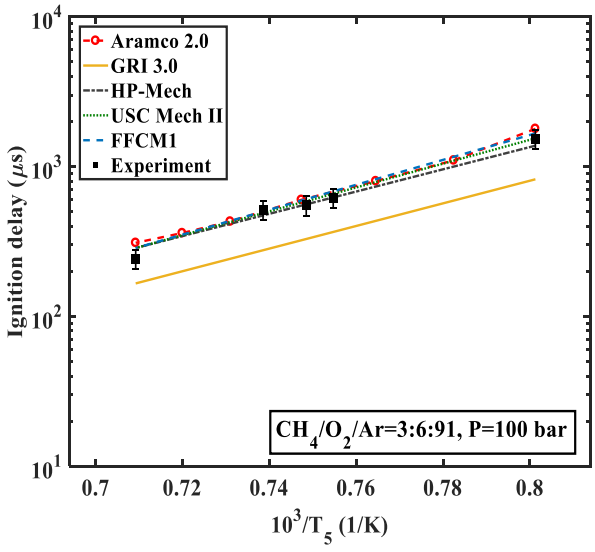

Figure 4.12. Ignition delay time measurements of stoichiometric $CH_4/O_2/Ar$ mixtures at 100 bar, T=1248–1410 K

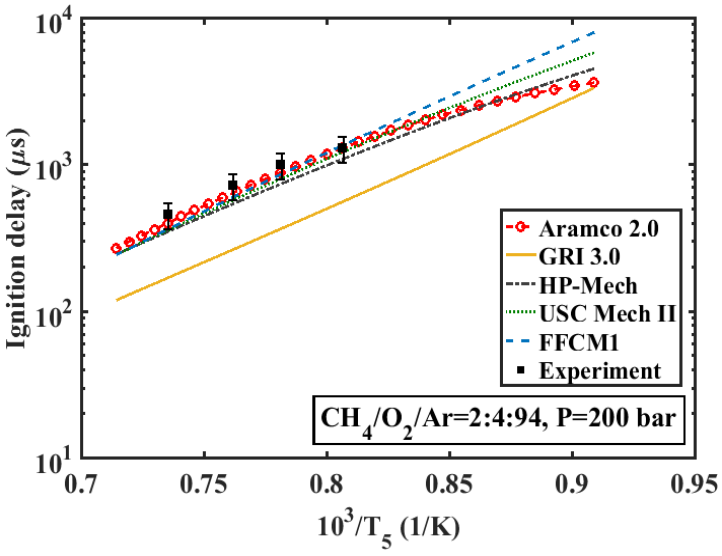

Figure 4.13. Ignition delay time measurements of stoichiometric $CH_4/O_2/Ar$ mixtures at 200 bar, T=1253–1379 K

Figure 4.12 and Figure 4.13 show that predictions from Aramco 2.0 and FFCM-1 very closely match the experimentally measured IDTs at 100 and 200 bar, and that predictions from HP-Mech also reasonably agree with experiments. However, GRI 3.0 is incapable of predicting the autoignition delays seen in the experiments. This is very similar to the $CH_4/O_2/CO_2$ mixture results, except that at 200 bar and lower temperature ranges, Aramco 2.0 is the only kinetic model that could properly predict ignition. Sensitivity and reaction path flux analyses are performed for the $CH_4/O_2/Ar$ mixtures at 1200 K to further investigate ignition trends and the results are shown in Figure 4.14, Figure 4.15 and Figure 4.16.

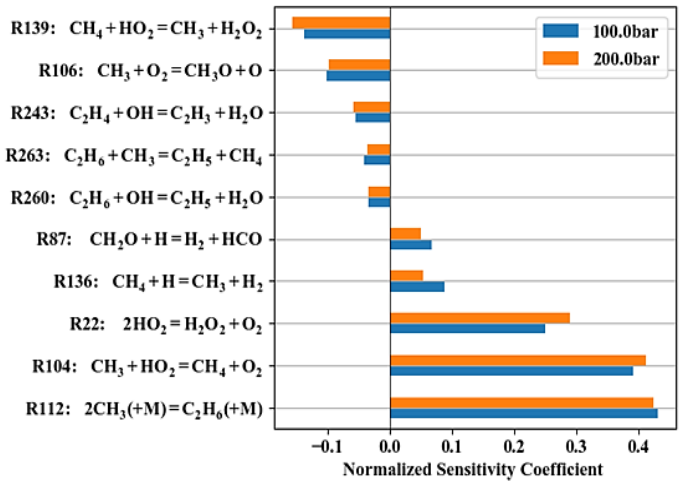

Figure 4.14. Sensitivity of IDT for $CH_4/O_2/Ar$ mixtures at 1200 K, 100 and 200 bar using FFCM-1

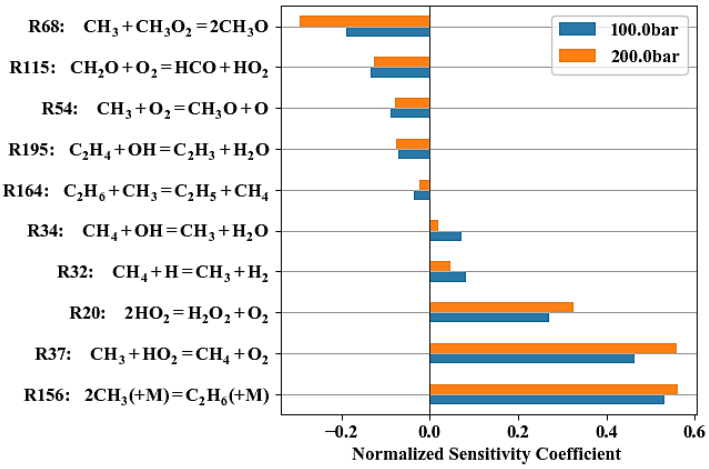

Figure 4.15. Sensitivity of IDT for $CH_4/O_2/Ar$ mixtures at 1200 K, 100 and 200 bar using Aramco 2.0

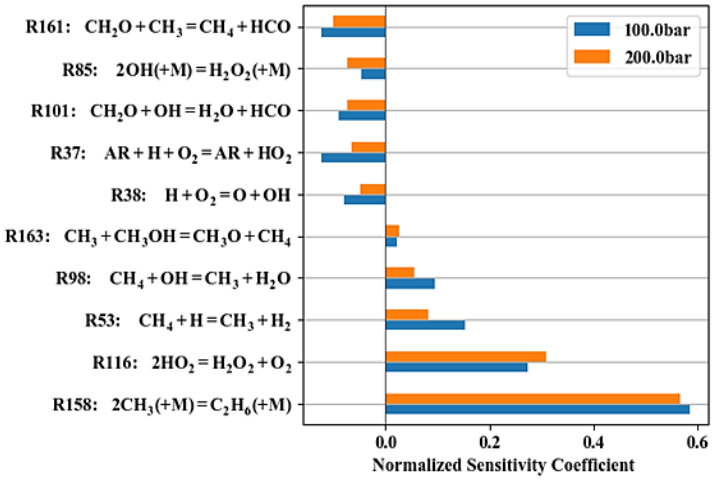

Figure 4.16. Sensitivity of IDT for $CH_4/O_2/Ar$ mixtures at 1200 K, 100 and 200 bar using GRI 3.0

The sensitivity analysis suggests that the major sink of the methyl radicals is through the recombination reaction to form ethane. This reaction, predicted by all kinetic models, is the most influential reaction hindering ignition at 100 and 200 bar. This result is slightly different from the $CH_4/O_2/CO_2$ mixture results, which showed that ignition is most sensitive to CH_3 oxidation. Reaction: $2HO_2 = H_2O_2+O_2$ is also important to the autoignition event. One reaction that is missing from GRI 3.0 but that appears in Aramco 2.0 and FFCM-1 is $CH_3+HO_2=CH_4+O_2$. This suggests that studying the CH_3 reaction pathway can provide an explanation for the discrepancy observed in Figure 4.12 and Figure 4.13. Therefore, the carbon path flux analysis was conducted at 100 and 200 bar, and the results are shown in Figure 4.17 and Figure 4.18.

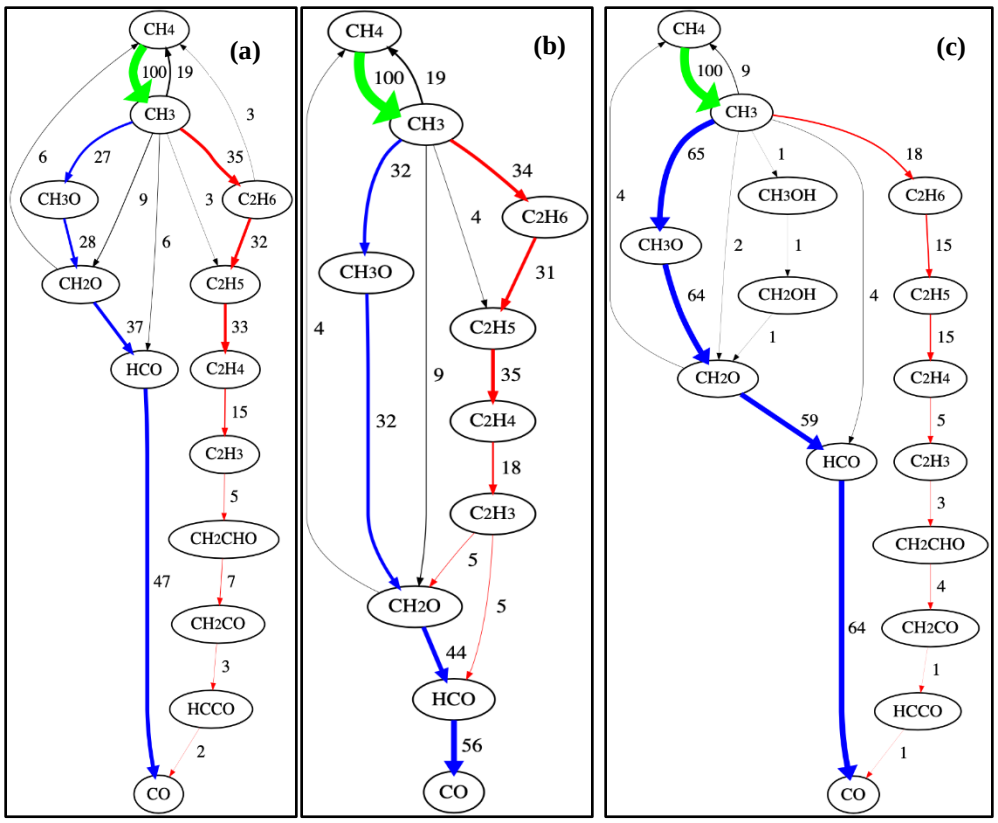

Figure 4.17. Reaction path flux results for $CH_4/O_2/Ar=3:6:91$ at 1200 K and 100 bar using (a) Aramco 2.0 (b) FFCM-1 and (c) GRI 3.0

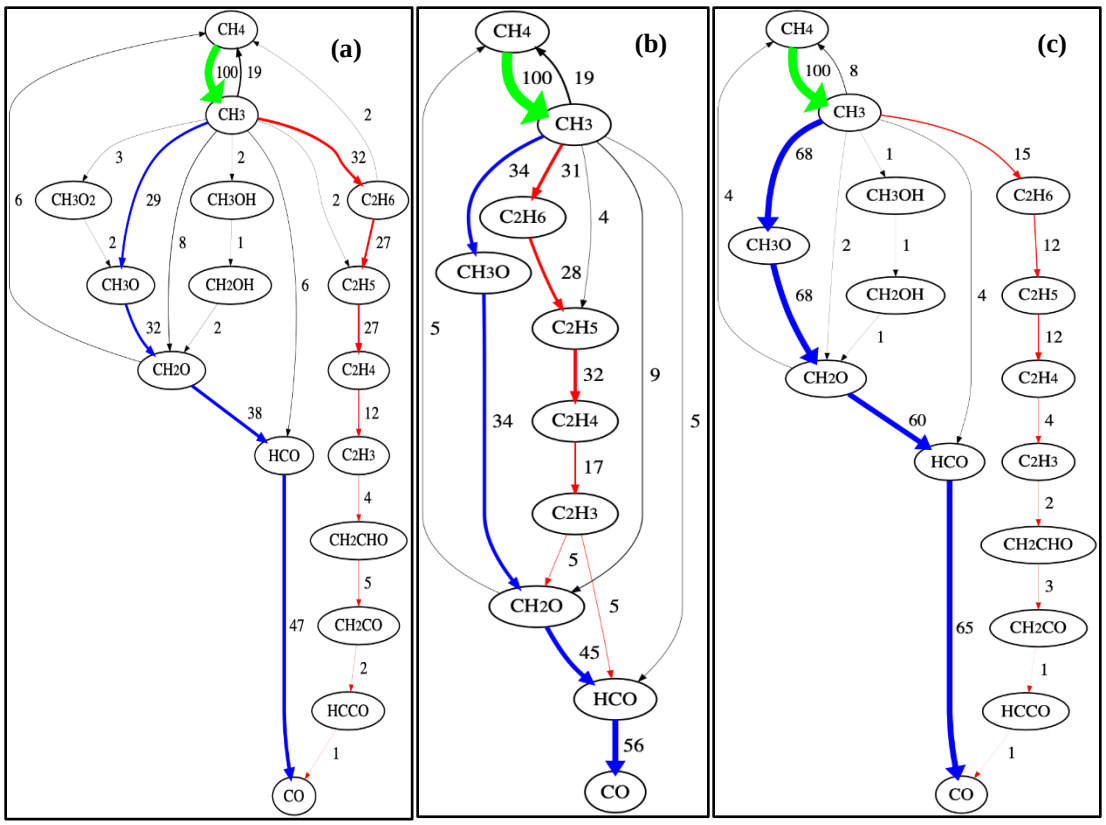

Figure 4.18. Reaction path flux results for $CH_4/O_2/Ar$=3:6:91 at 1200 K and 200 bar using (a) Aramco 2.0 (b) FFCM-1 and (c) GRI 3.0

Very similar to the $CH_4/O_2/CO_2$ results, the reaction path flux analysis using GRI 3.0 suggests that the most dominant pathway at 100 and 200 bar is through reaction pathway (1), which is competing with the CH_3 recombination pathway. The dominance of the methyl oxidation pathway predicted by GRI 3.0 is in agreement with the underprediction of IDTs by this model, as observed previously in Figure 4.2 and Figure 4.3. At 100 and 200 bar, pathway (2) is the dominant recombination path for Aramco 2.0 and pathways (3) and (4) are the dominant recombination pathways for FFCM-1. Due to the higher temperature range (1253–1379 K) for experiments using Ar as diluent, the effect of CH_3O_2 kinetics was not significant.

CHAPTER 5. Syngas Results and Discussions

5.1 Autoignition of $H_2/CO/O_2/CO_2$ Mixtures

Measurements of autoignition delays for $H_2/CO/O_2/CO_2$ and $H_2/CO/O_2/Ar$ mixtures are presented and discussed in this section. Details of the experimental conditions and measured ignition delay times (IDTs) are provided in the appendix A. Experimental results are also compared to simulations using different chemical kinetic models including USC Mech II [26], Aramco 2.0 [28-34], GRI 3.0 [24], HP-Mech [25] and FFCM-1 kinetic model [27]. The experimental conditions (P_5 and T_5) for the study are targeted to be above the critical points of the mixtures. Therefore, the critical temperatures (T_{crit}) and critical pressures (P_{crit}) of the mixtures are calculated using NIST Reference Fluid Thermodynamic and Transport Properties Database (REFPROP) [15] prior to conducting experiments. Table 5.1 shows the T_{crit} and P_{crit} for all the mixtures in the study along with the conditions where the IDTs were measured.

Table 5.1. Ignition delay test conditions and critical points

Exper. cases	Reactant mole fractions					Conditions		Critical points	
	H_2	CO	O_2	CO_2	Ar	T_5 (K)	P_5 (bar)	T_{crit} (K)	P_{crit} (bar)
1	2.85	0.15	1.5	95.5	0	1186–1365	90–106	304.01	87.624
2	2.85	0.15	1.5	0	95.5	1196–1275	89–100	151.94	58.381
3	5.7	0.3	1.5	92.5	0	1175–1280	84–90	303.04	97.441
4	2.85	0.15	1.5	95.5	0	1161–1257	204–213	304.01	87.624

An approach similar to methane study is taken to study the real gas effect where the R-K EoS is used for pressure, temperature, specific volume and thermodynamic calculations. Figure 5.1 shows IDTs calculated using Aramco 2.0 and FFCM-1 using the ideal gas EoS and Redlich-Kwong EoS, respectively for a mixture of $H_2/CO/O_2/CO_2$=2.85:0.15:1.5:95.5 at 100 and 200 bar. As shown in this figure, the difference in IDT predictions using the real gas (R-K) EoS and the ideal gas EoS becomes larger as the pressure is doubled for the same mixture and temperature range. However, for the experimental conditions in this study, the maximum deviations in IDTs using the real gas EoS and the ideal gas EoS are less than 2%. The uncertainty of the IDTs reported experimentally is approximately 20%; therefore, the choice of EoS for validation purposes of different kinetics models based on experimental data is not critical.

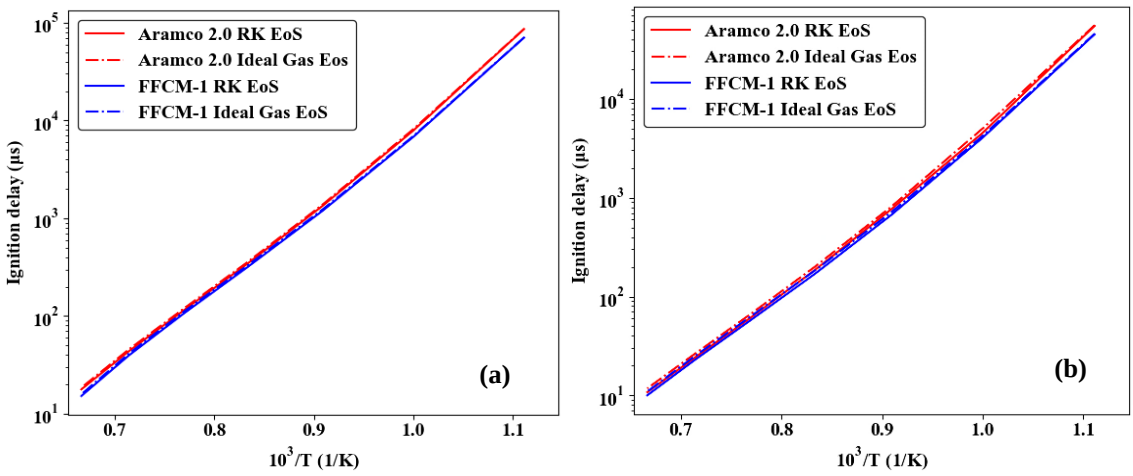

Figure 5.1. Real gas EoS and ideal gas EoS effects on chemical kinetics models for $H_2/CO/O_2/CO_2$=2.85:0.15:1.5:95.5 at a) 100 bar and b) 200 bar

The compressibility factors (calculated by REFPROP [15]) for the mixtures used in this study are listed in Table 5.2 as a reference. It can be seen that the compressibility factors are all very close to 1, suggesting that the ideal gas EoS is a reasonable choice for the current work. Therefore, the ideal gas EoS is used in CHEMKIN-PRO [140] and CANTERA [152] for the calculations reported in the following sections.

Table 5.2. Compressibility factors (Z) of the mixtures

Exper. cases	Reactant mole fractions					Conditions		Compressibility Factor (Z)
	H_2	CO	O_2	CO_2	Ar	T (K)	P (bar)	
1	2.85	0.15	1.5	95.5	0	1186	100	1.0240
2	2.85	0.15	1.5	0	95.5	1196	100	1.0224
3	5.7	0.3	1.5	92.5	0	1175	100	1.0242
4	2.85	0.15	1.5	95.5	0	1161	200	1.0491

IDTs for $H_2/CO/O_2/CO_2$ mixtures at stoichiometric and fuel-rich conditions (Φ=2) measured at 100 bar and at temperatures between 1175– 1365 K are shown in Figure 5.2. The predicted IDTs from different kinetic models are compared with experimental values. The simulation results herein are obtained by solving a zero-dimensional reactor with constant internal energy and volume using CHEMKIN-PRO [140]. Figure 5.3 summarizes the results obtained from 200 bar experiments for a 2.85:0.15:1.5:95.5 mixture of $H_2/CO/O_2/CO_2$.

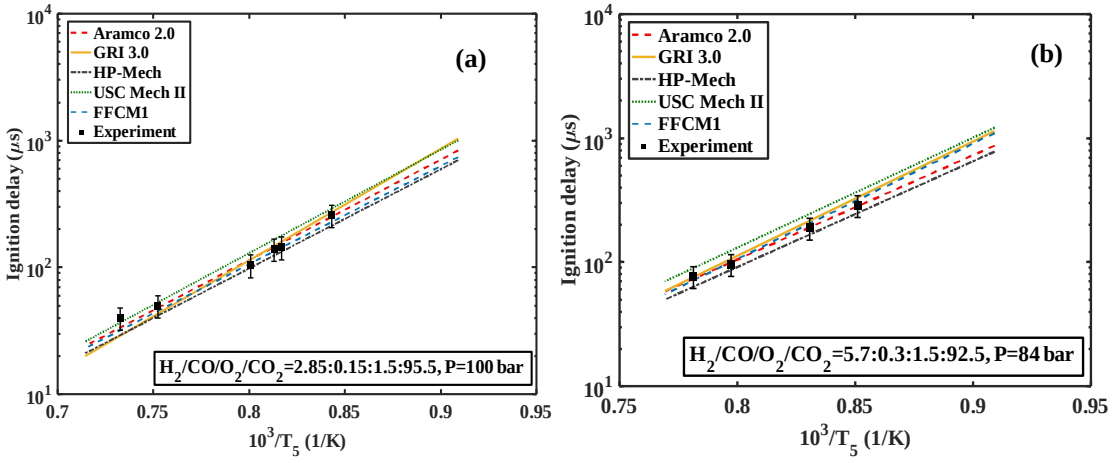

Figure 5.2. Ignition delay time of $H_2/CO/O_2/CO_2$ mixture at 100 bar for (a): stoichiometric (Φ =1), T=1186–1365K (b): rich (Φ =2) mixtures, T=1175–1280K

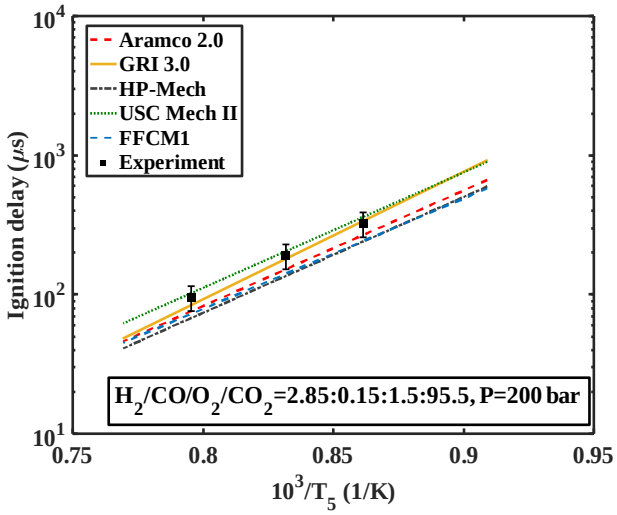

Figure 5.3. Ignition delay time measurements of stoichiometric $H_2/CO/O_2/CO_2$ mixture at 200 bar, T=1161–1257K

As shown in Figure 5.2 and Figure 5.3, the experimental data show very good agreement with IDT predictions (within the experimental uncertainty) of all kinetics models. To better understand the behavior of different kinetic models on predicting the autoignition delay brute-force sensitivity analysis for FFCM-1 and Aramco 2.0 was conducted in CANTERA [152] using the normalized sensitivity coefficient of $\frac{k_i}{\tau}\frac{\partial \tau}{\partial k_i}$. These

two kinetics model show to have a very well agreement with the experimental data. Therefore, these mechanisms were selected to perform the remaining of the analyses for both mixtures.

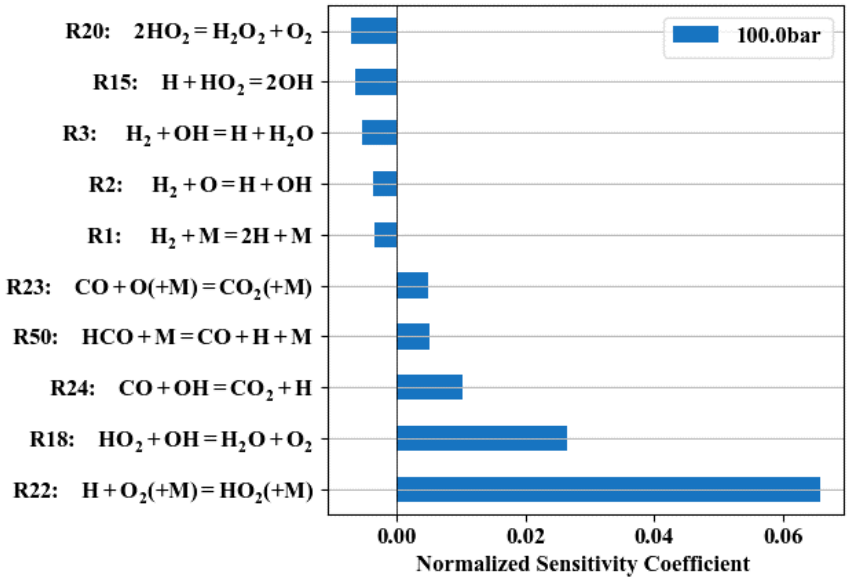

Figure 5.4. Sensitivity analysis of IDT at 1200 K, 100 bar using Aramco 2.0

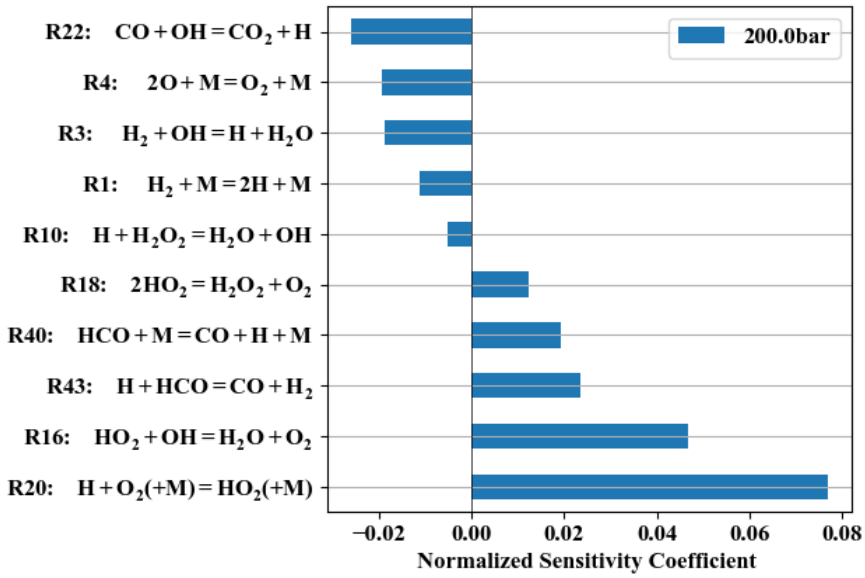

Figure 5.5. Sensitivity analysis of IDT at 1200 K, 200 bar using Aramco 2.0

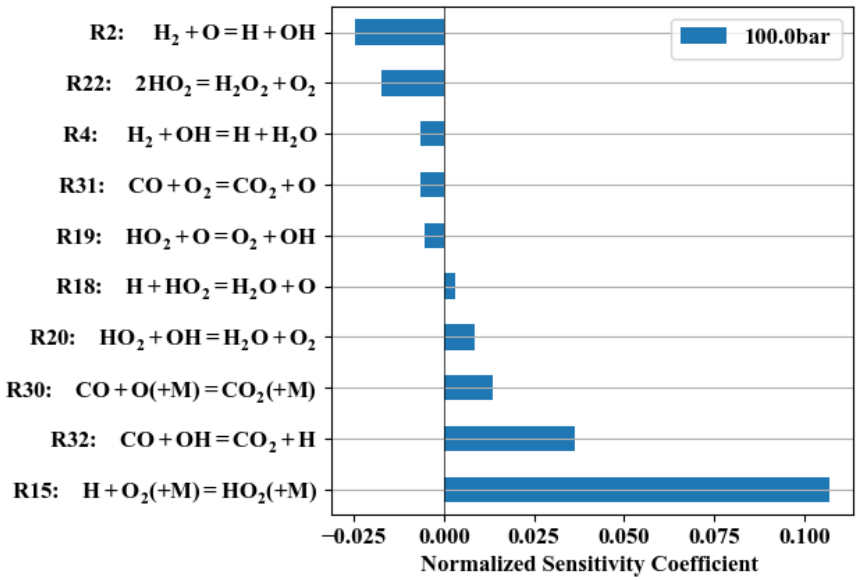

Figure 5.6. Sensitivity analysis of IDT at 1200 K, 100 bar using FFCM-1

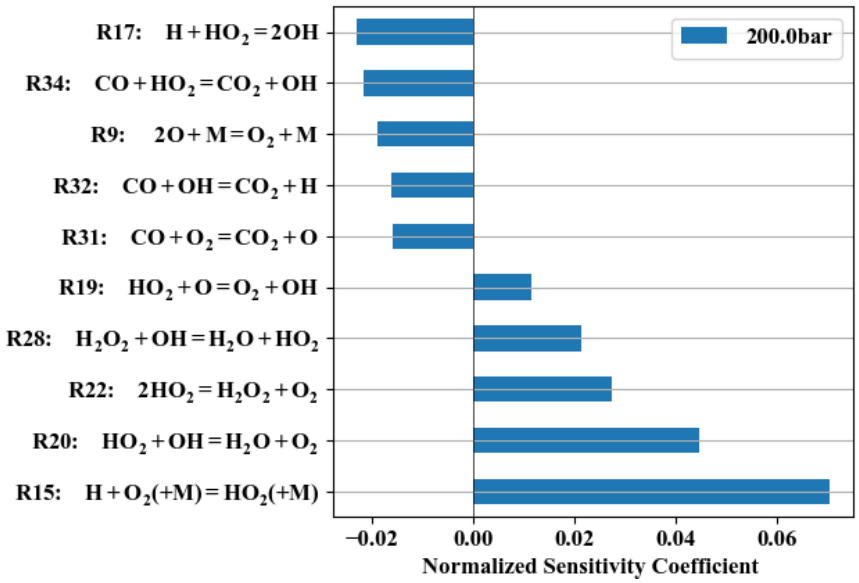

Figure 5.7. Sensitivity analysis of IDT at 1200 K, 200 bar using FFCM-1

While various kinetic models have many differences in their detailed chemical reactions, the pre-exponential factors and activation energies, yet general information regarding important reactions could be obtained through sensitivity analysis. For example,

both mechanisms selected here for this analysis emphasize the importance of reaction $H+O_2$ (+M) = HO_2 (+M) as the main inhibitor of ignition at 100 and 200 bar. Another important reaction in prohibiting ignition is found to be $HO_2+OH=H_2O+O_2$. Focusing on 100 bar results, reactions $2HO_2=H_2O_2+O_2$, $H_2+OH=H+H_2O$, and $H_2+O=H+OH$ are picked up by both mechanisms as main reactions to enhance ignition. Two important reactions that suppress ignition at this pressure are found to be CO+O (+M) = CO_2 (+M), and CO+OH = CO_2+H appearing in sensitivity analyses from both mechanisms.

As the pressure increases to 200 bar, the sensitivity analysis from both mechanisms show some differences in the reactions controlling ignition compared to 100 bar. For example, one of the major differences is that reaction $CO+OH=CO_2+H$ is enhancing ignition while reaction $2HO_2=H_2O_2+O_2$ plays an inhibiting role on ignition. This observation is the opposite of the 100 bar case. In Aramco 2.0 simulation results at 200 bar, two other important reactions appear as $H+H_2O_2=H_2O+OH$ and $H+HCO=CO+H_2$ as an enhancer and inhibitor reactions, respectively. This suggests that as the pressure is doubled, the productions of H_2O_2 and CO are increased at the ignition point (~200 μsec at 200 bar and ~100 μsec at 100 bar). This could be observed when the CO and H_2O_2 mole fractions are plotted at 100 and 200 bar using Aramco 2.0 mechanism as seen in Figure 5.8 and Figure 5.9.

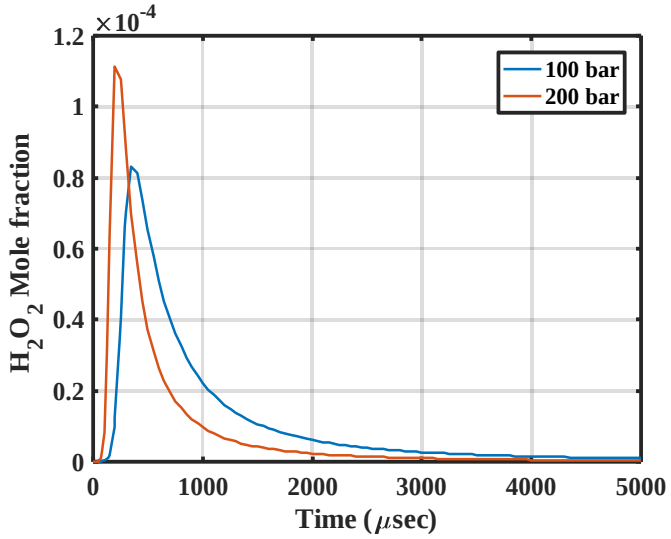

Figure 5.8. H_2O_2 mole fraction using Aramco 2.0

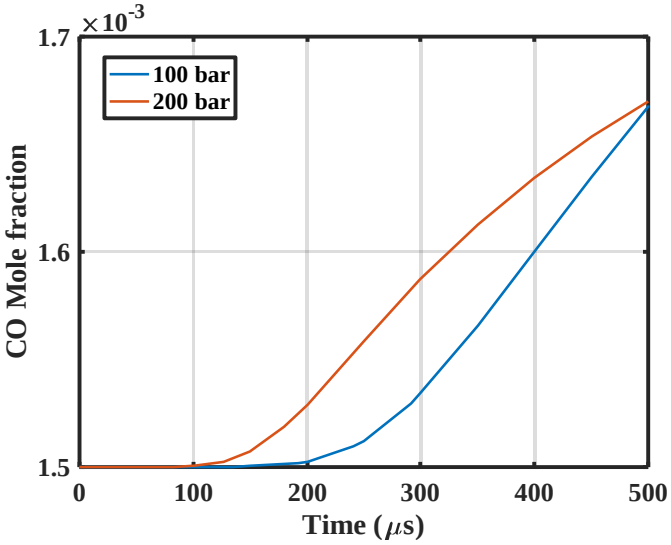

Figure 5.9. CO mole fraction using Aramco 2.0

FFCM-1 kinetic model also highlights additional reactions involving these two species at 200 bar. These reactions are $H_2O_2+OH=H_2O+HO_2$ and $CO+HO_2=CO_2+OH$ where the former inhibits the ignition and the later enhances the ignition. This kinetic model shows that the formation of HO_2 through $H_2O_2+OH=H_2O+HO_2$ and recombination of this species through $2HO_2=H_2O_2+O_2$ could inhibit ignition. On the other hand, the

production of CO through $CO+HO_2=CO_2+OH$ could enhance reaction $CO+OH=CO_2+H$ and accelerate ignition.

It is clear from the results of both mechanisms that reactions $2HO_2=H_2O_2+O_2$ and $CO+OH=CO_2+H$ show opposite effects in governing ignition trends. However, these two mechanisms show different paths leading to such phenomena. Limited information could be obtained from sensitivity analyses regarding the extent of which these reactions could alter the ignition chemistry. Therefore, alternative analyses such as reaction pathways and rate of productions of key species are considered and the results are summarized herein.

It is also evident from the sensitivity analyses that the hydrogen oxidation is the dominant pathway for syngas mixtures ignition considered for this study. Therefore, the hydrogen atom flux is generated through Global Pathway Selection (GPS) method [153] in CANTERA [152] for temperature of 1200 K and 100 and 200 bar pressures for $H_2/CO/O_2/CO_2=2.85:0.15:1.5:95.5$ mixture. Figure 5.10 shows the reaction path flux results for this mixture at 1200 K and 100 bar using Aramco 2.0. The numbers shown in this figure represent the percentage of hydrogen atom flux (normalized by the total hydrogen flux of the fuel) through various pathways. The cut-off time for these analyses is the time when ignition occurred.

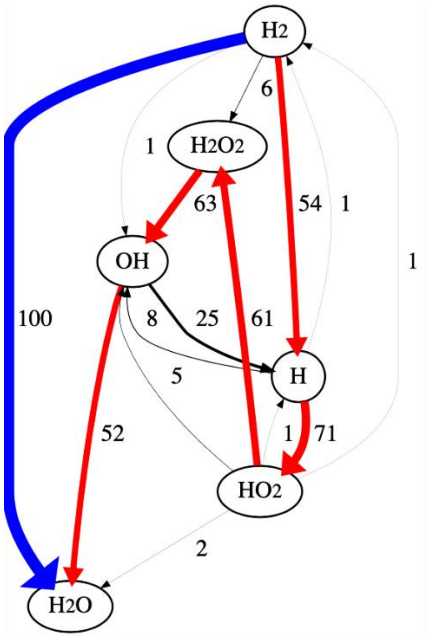

Figure 5.10. Reaction path flux results for $H_2/CO/O_2/CO_2$=2.85:0.15:1.5:95.5 at 1200 K and 100 bar using Aramco 2.0

The reaction pathway shows that the dominant oxidation pathways for hydrogen oxidation are $H_2 \rightarrow H_2O$ and $H_2 \rightarrow H \rightarrow HO_2 \rightarrow H_2O_2 \rightarrow OH \rightarrow H_2O$. These pathways remain the same for 100 and 200 bar using Aramco 2.0 and FFCM-1 kinetic models and no major differences are noticed in that regards. This observation suggests that while reactions $2HO_2=H_2O_2+O_2$ and $CO+OH=CO_2+H$ have the opposite effect in enhancing and inhibiting ignition at 100 and 200 bar, their effects in altering ignition delay time chemistry is negligible compared to other important reactions. For instance, the most important reaction in controlling ignition at 100 and 200 bar for $H_2/CO/O_2/CO_2$=2.85:0.15:1.5:95.5 mixture is $H+O_2 (+M) = HO_2 (+M)$. The third-body collision efficiency of M (in this case CO_2) is listed as 3.8 in original Aramco 2.0 mechanism and 3.45 in FFCM-1 kinetics model. Using Aramco 2.0 mechanism, changing the collision efficiency from M=3.8 to M=0.5 of this reaction, the ignition delay times could be reduced as much as approximately 50% at 100 bar and 36% at 200 bar as shown in Figure 5.11 and Figure 5.12.

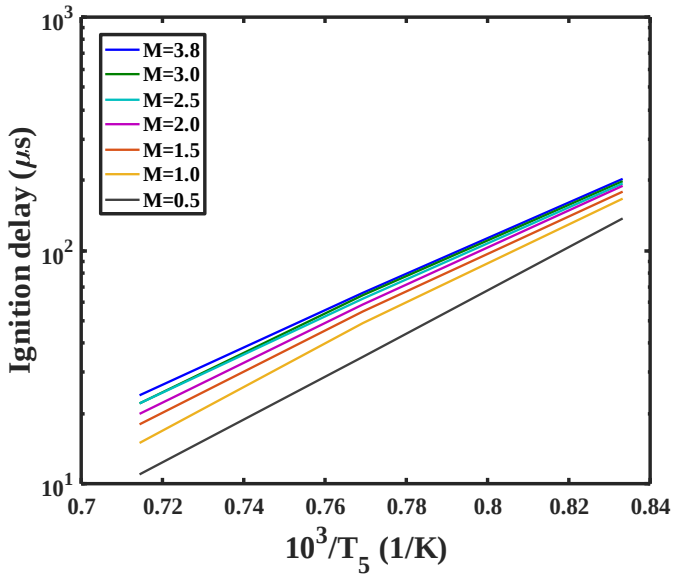

Figure 5.11. Effect of various M values in $H+O_2$ (+M) = HO_2 (+M) for $H_2/CO/O_2/CO_2$=2.85:0.15:1.5:95.5 mixture on IDT predictions from Aramco 2.0 mechanism at 100 bar

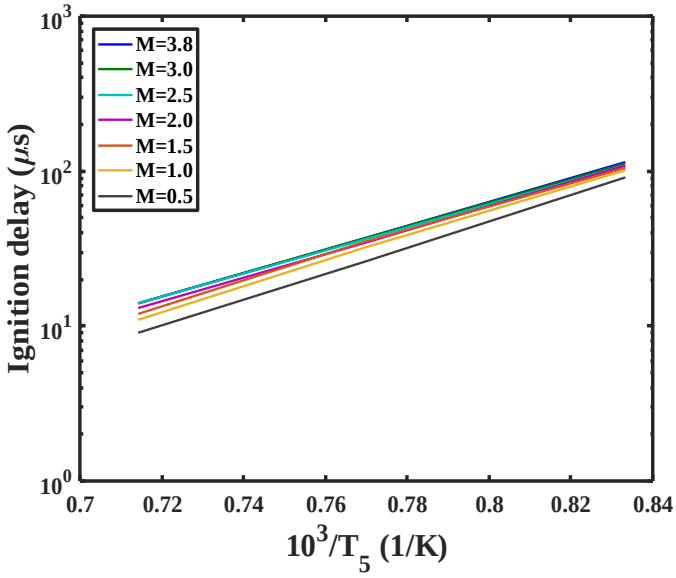

Figure 5.12. Effect of various M values in $H+O_2$ (+M) = HO_2 (+M) for $H_2/CO/O_2/CO_2$=2.85:0.15:1.5:95.5 mixture on IDT predictions from Aramco 2.0 mechanism at 200 bar

The measured IDTs show very well agreements with predictions from the original Aramco 2.0 mechanism (M=3.8 for CO_2 in reaction $H+O_2$ (+M) = HO_2 (+M)). Therefore, to merely investigate the effect of pressure on $H_2/CO/O_2/CO_2$=2.85:0.15:1.5:95.5 mixture, the rate of productions for key species (OH, HO_2 and CO) and their main contributing reactions are investigated and the results are shown below. As could be seen from these figures, the main reactions contributing to the rate of production and consumption of these species are almost identical. Furthermore HO_2 sensitivity analyses at 100 and 200 bar also show no difference in top seven reactions most sensitive to production and consumption of this specie as shown in Figure 5.16. Therefore, based on various analyses conducted thus far, it is evident that using Aramco 2.0 mechanism, increasing pressure from 100 to 200 bar does not alter the ignition chemistry significantly for $H_2/CO/O_2/CO_2$=2.85:0.15:1.5:95.5 mixture.

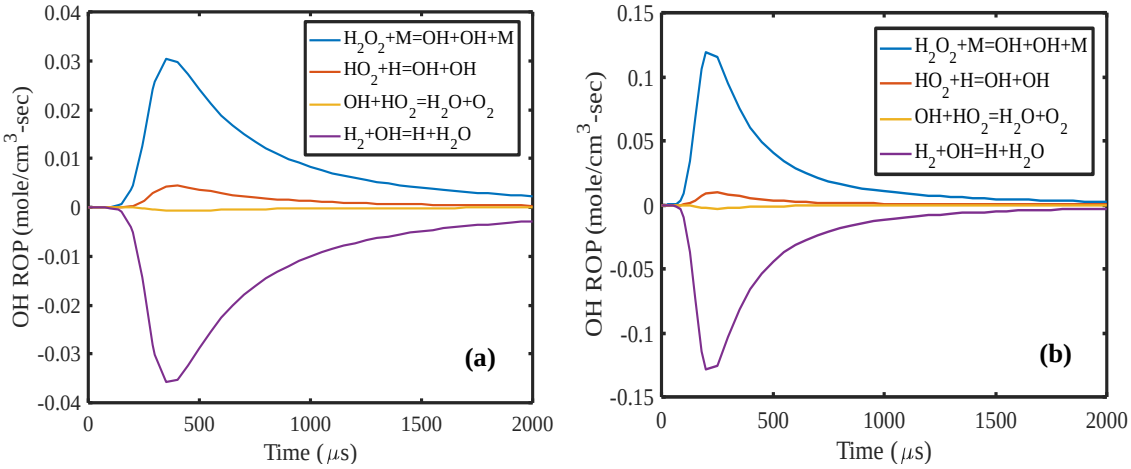

Figure 5.13. OH Rate of Production (ROP) for $H_2/CO/O_2/CO_2$=2.85:0.15:1.5:95.5 at 1200 K for a) 100 bar, b) 200 bar

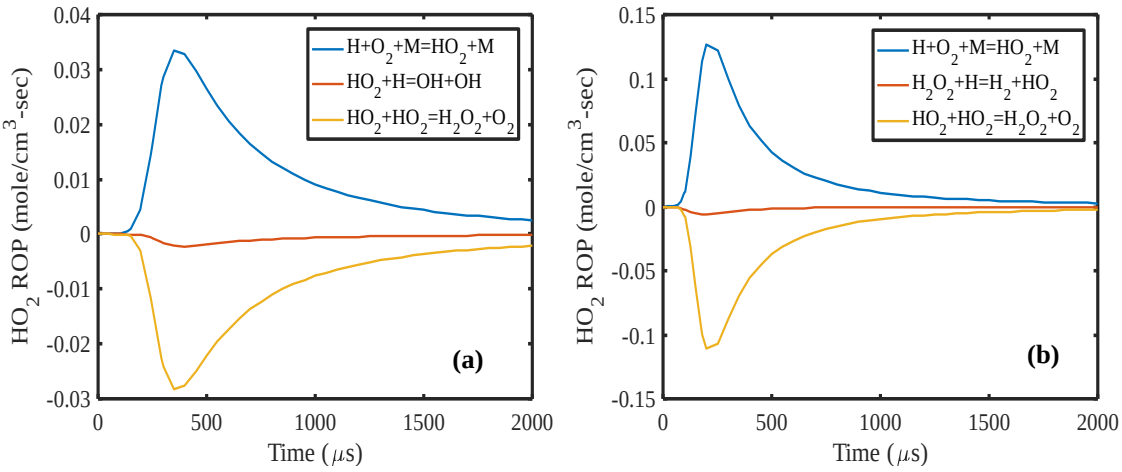

Figure 5.14. HO_2 Rate of Production (ROP) for $H_2/CO/O_2/CO_2$=2.85:0.15:1.5:95.5 at 1200 K for a) 100 bar, b) 200 bar

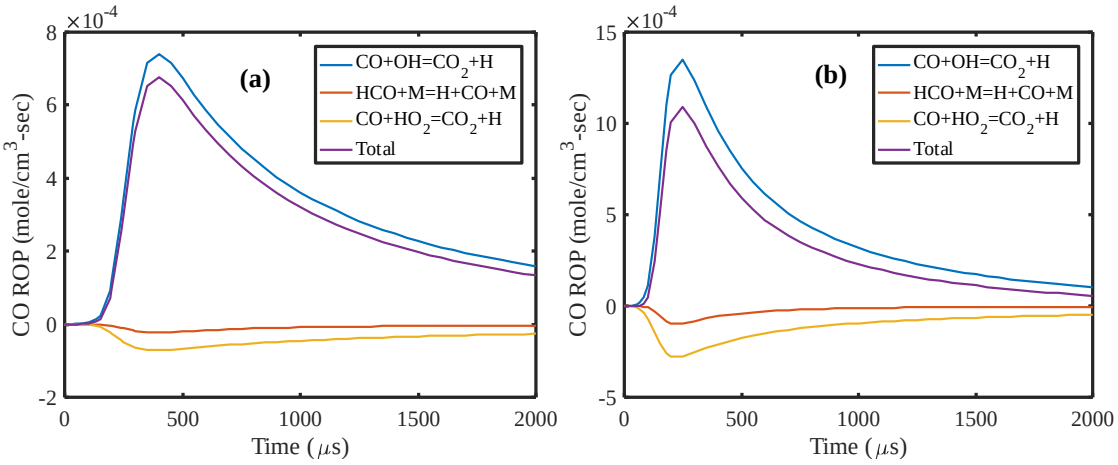

Figure 5.15. CO Rate of Production (ROP) for $H_2/CO/O_2/CO_2$=2.85:0.15:1.5:95.5 at 1200 K for a) 100 bar, b) 200 bar

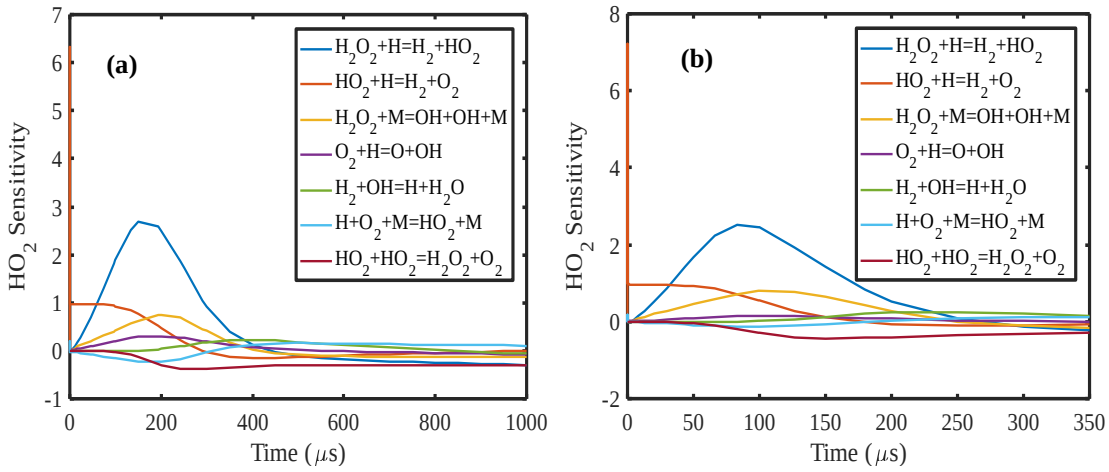

Figure 5.16. HO_2 Sensitivity for $H_2/CO/O_2/CO_2$=2.85:0.15:1.5:95.5 at 1200 K for a) 100 bar, b) 200 bar

5.2 Autoignition of $H_2/CO/O_2$/Ar Mixtures

In previous section, the effect of pressure on ignition delay time was investigated and it was found that increasing pressure from 100 to 200, the rate of production of key species and the most sensitive reactions in that regards remain unchanged. Furthermore, the third-body collision efficiency (M) of CO_2 in reaction $H+O_2$ (+M) = HO_2 (+M) was studied and it was found that by reducing M, the ignition delay time is reduced at 100 and 200 bar. While this information provides some insights regarding the ignition characteristics of $H_2/CO/O_2/CO_2$=2.85:0.15:1.5:95.5 mixture, however the chemical effect of CO_2 is yet to be explained.

To study the chemical effect of CO_2 in syngas mixture, experiments were conducted at around 100 bar for $H_2/CO/O_2$/Ar=2.85:0.15:1.5:95.5 mixture where simply CO_2 is replaced by an inert bath gas, argon. To have a direct comparison, a similar temperature range was targeted experimentally and the results are presented in Figure 5.17. Prior to proceeding with the remaining of the discussion, it should be noted that constant

temperature and pressure in zero-dimensional reactor model is used for conducting the analyses herein as well as in the previous section. This was done to eliminate the thermal effect of argon and carbon dioxide on ignition and allowing for studying chemical effects on the IDT systematically.

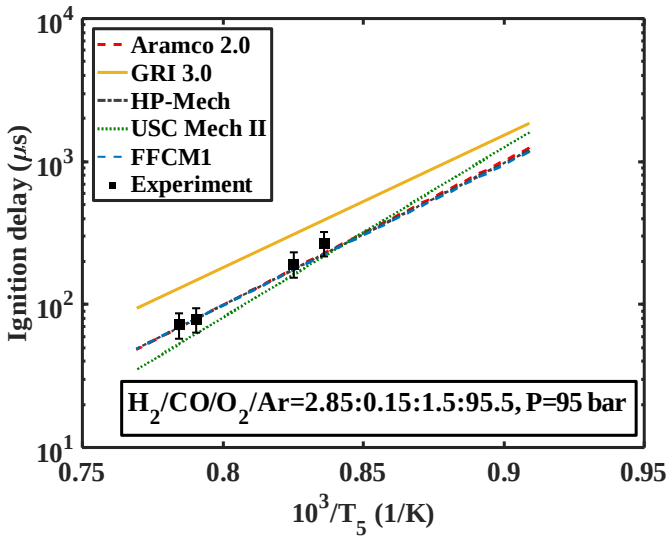

Figure 5.17. Ignition delay time of stoichiometric $H_2/CO/O_2/Ar$ mixture at 100 bar and T=1196–1275

As observed from this figure, except for GRI 3.0 mechanism, the experimental data (within the uncertainty of the measurements) agree well with the predictions from USC Mech II, Aramco 2.0, HP-Mech and FFCM-1 kinetic model. Since the experimental results were obtained at a similar pressure and temperature ranges, the IDTs could be compared directly to the values obtained from $H_2/CO/O_2/CO_2$ case. As could be seen from Figure 5.18, the ignition delay times follow the same trend and overlay nicely when CO_2 is replaced by Ar. To further explain this observation, a similar approach as in previous section is taken where the sensitivity analyses are conducted for both mixtures at a medium temperature of 1200 K as the initial step. It is important to note that the reaction pathway

analyses for $H_2/CO/O_2/Ar$=2.85:0.15:1.5:95.5 mixture in terms of tracking hydrogen atoms is similar to what was presented in Figure 5.10.

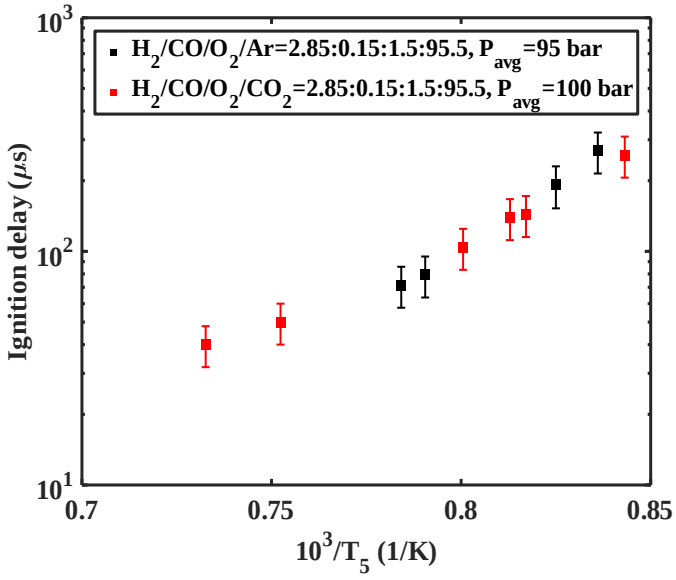

Figure 5.18. Comparison of ignition delay time measurements of $H_2/CO/O_2/Ar$ and $H_2/CO/O_2/CO_2$ at 100 bar and T=1186–1365 K

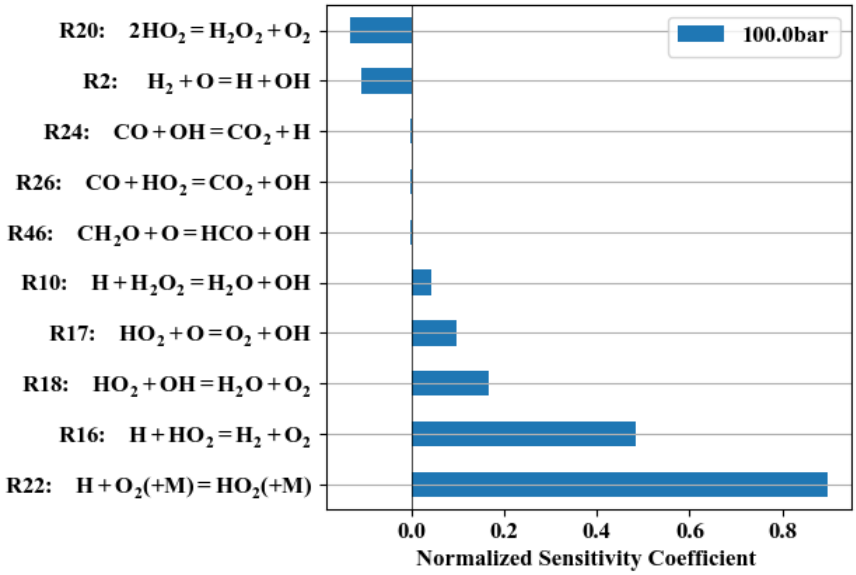

Figure 5.19. Sensitivity analysis of IDT at 1200 K for $H_2/CO/O_2/Ar$=2.85:0.15:1.5:95.5 mixture at 100 bar using Aramco 2.0

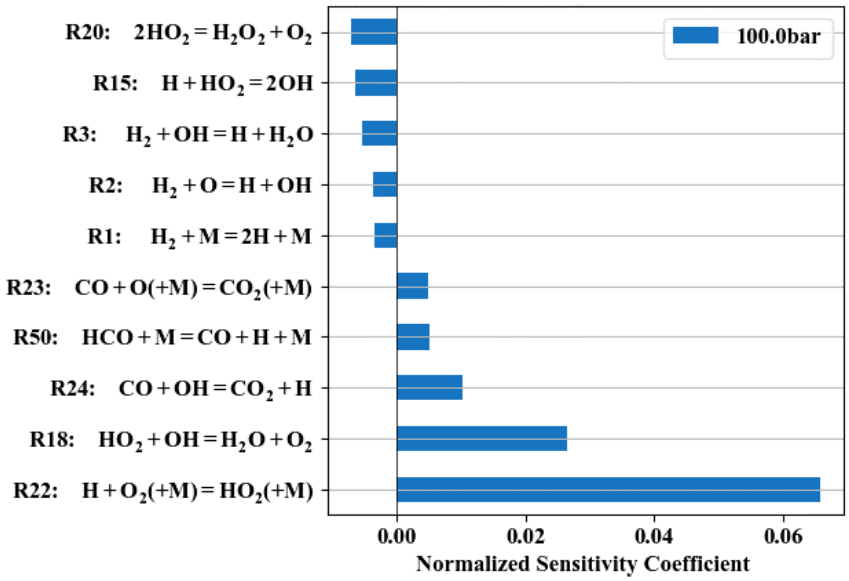

Figure 5.20. Sensitivity analysis of IDT at 1200 K for $H_2/CO/O_2/CO_2$=2.85:0.15:1.5:95.5 mixture at 100 bar using Aramco 2.0

Comparing the results from these two figures suggests that there are some similarities in important reactions governing the ignition chemistry. For example, the most dominant reaction in hindering ignition is $H+O_2$ (+M) = HO_2 (+M). The importance of this reaction is so significant in the argon mixture that reducing the reaction rate coefficient of this single reaction could change the ignition delay time prediction by a kinetic model significantly. As observed from Figure 5.21, GRI 3.0 mechanism is over predicting the IDT by as much as a factor of two. If the reaction rate of reaction R22 is halved in this mechanism, IDT predictions match the experimental data as observed in Figure 5.21.

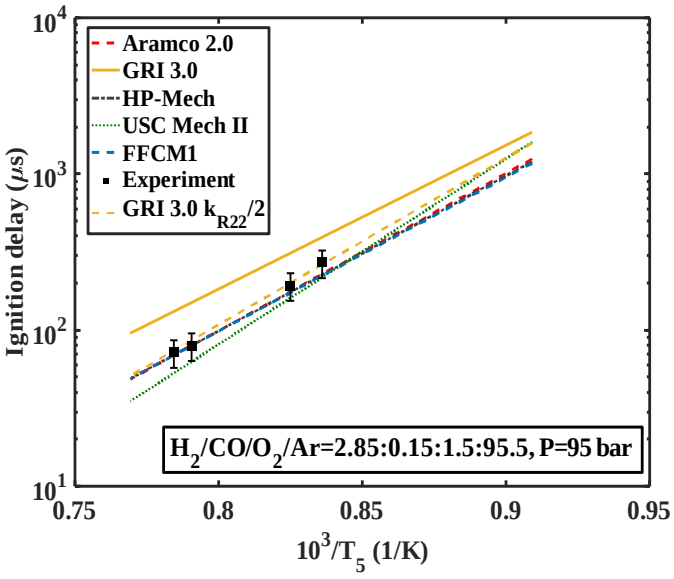

Figure 5.21. Effect of reducing reactions rate coefficient in improving GRI 3.0 mechanism in predicting IDT

In addition to R22, reaction $HO_2+OH=H_2O+O_2$ is also appearing as one of the important reactions in hindering ignition. The similarities in sensitivity analysis from these two mixtures are not limited to reactions that hinder ignition. Reactions $2HO_2=H_2O_2+O_2$ and $H_2+O=H+OH$, which are two of the most influential reactions on ignition are also appearing in Ar and CO_2 mixtures. Moreover, the mole fractions of some of the key species such as OH and HO_2 are nearly identical at the ignition point (~200 μsec at 100 bar) for both mixtures as could be observed in Figure 5.22 and Figure 5.23.

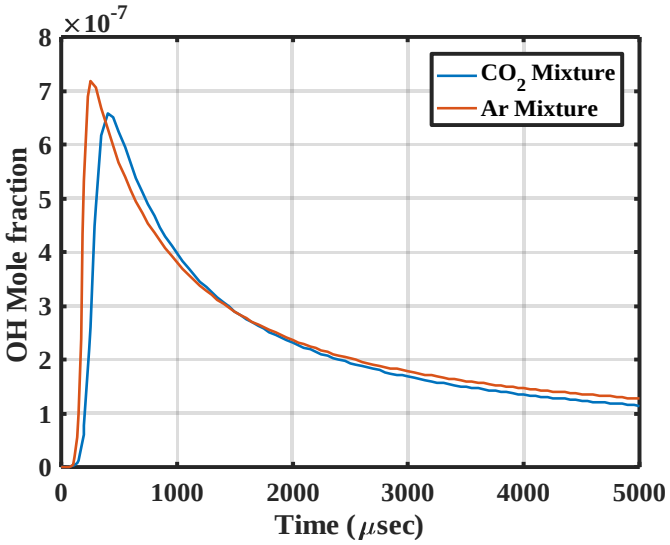

Figure 5.22. OH mole fraction comparison for mixtures $H_2/CO/O_2/Ar=2.85:0.15:1.5:95.5$ and $H_2/CO/O_2/CO_2=2.85:0.15:1.5:95.5$ at 100 bar and 1200 K

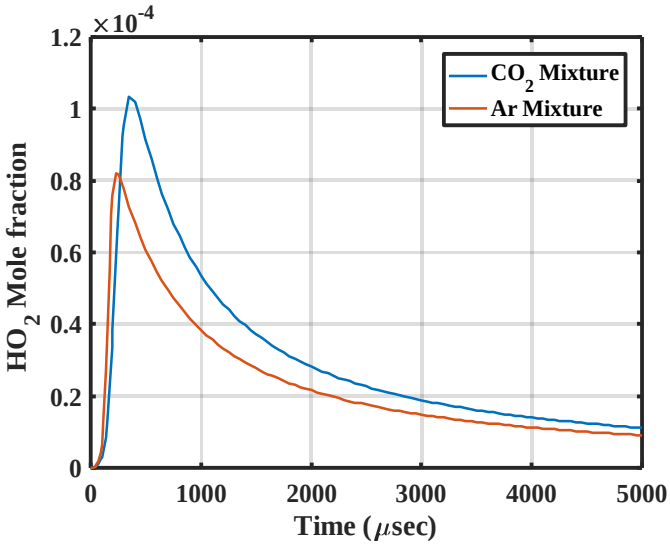

Figure 5.23. HO_2 mole fraction comparison for mixtures $H_2/CO/O_2/Ar=2.85:0.15:1.5:95.5$ and $H_2/CO/O_2/CO_2=2.85:0.15:1.5:95.5$ at 100 bar and 1200 K

While there are similarities in the sensitivity analyses from both mixtures, however an obvious and indeed important discrepancy between the two emerges from reaction $CO+OH=CO_2+H$. This reaction appears as an ignition enhancer in argon mixture, but it appears as an ignition inhibitor in CO_2 mixture. As was observed previously, the OH mole

fraction is nearly the same at the ignition time for both mixtures. However, the situation is not the same when the H mole fraction and CO mole fraction are simulated using Aramco 2.0 mechanism. The hydrogen atom mole fraction is much higher in the Ar mixture than in the CO_2 mixture while this is the opposite for the CO mole fraction. Such trends could be seen in Figure 5.24 and Figure 5.25.

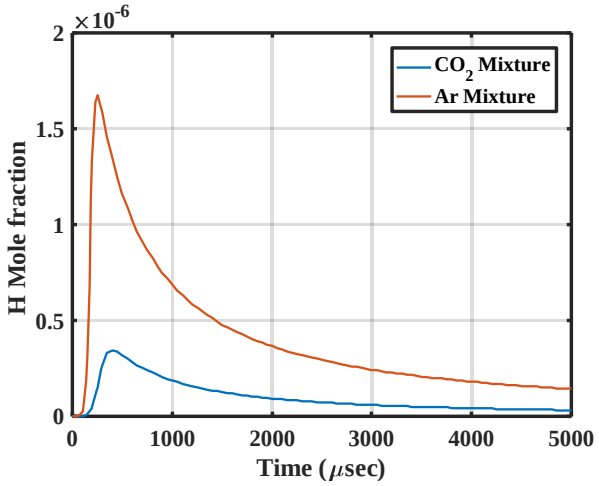

Figure 5.24. H mole fraction comparison for mixtures $H_2/CO/O_2/Ar$=2.85:0.15:1.5:95.5 and $H_2/CO/O_2/CO_2$=2.85:0.15:1.5:95.5 at 100 bar and 1200 K

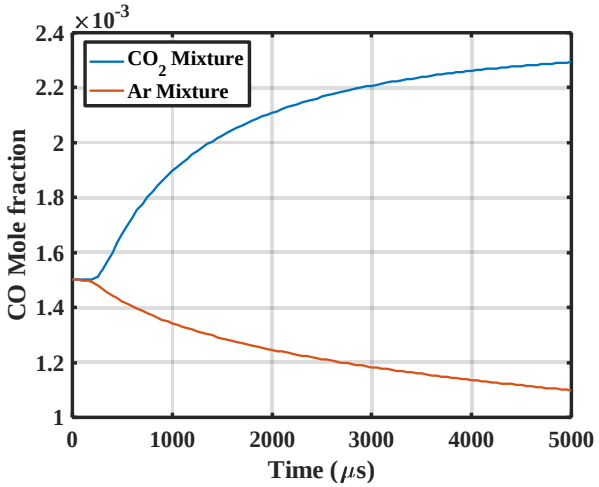

Figure 5.25. CO mole fraction comparison for mixtures $H_2/CO/O_2/Ar$=2.85:0.15:1.5:95.5 and $H_2/CO/O_2/CO_2$=2.85:0.15:1.5:95.5 at 100 bar and 1200 K

Whether other reactions are involved in counter effect of reaction $CO+OH=CO_2+H$ or not, the rate of production of CO and important reactions in that regard are investigated at 100 bar and 1200 K, and the results are shown in the following figures for both mixtures. As observed from Figure 5.26, this reaction is the main reaction in consuming CO in argon mixture while on the contrary it is the most dominant reaction in production of CO in the CO_2 mixture.

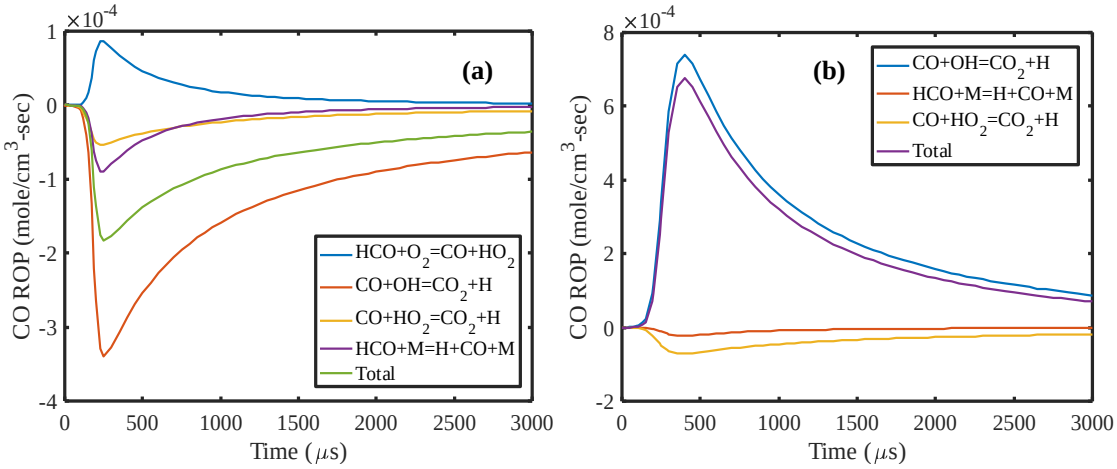

Figure 5.26. CO Rate of Production (ROP) at 100 bar and 1200 K for a) $H_2/CO/O_2/Ar=2.85:0.15:1.5:95.5$ mixture and b) $H_2/CO/O_2/CO_2=2.85:0.15:1.5:95.5$ mixture

A possibility to explain such phenomena is by investigating the role of hydrogen atom in its reaction with CO_2 since its mole fraction was shown to be dramatically different in argon and CO_2 mixture. Therefore, the rate of production of hydrogen atom is simulated and the results are shown below. As observed in Figure 5.27, reactions $H_2+OH=H+H_2O$ and $H+O_2+M=HO_2+M$ are the most dominant reactions in producing and consuming H radicals, respectively. However, there are differences such as reactions $H_2+O=H+OH$ and $O_2+H=O+OH$ where they appear in argon mixture analyses, while these reactions are replaced by $H_2O_2+H=H_2+HO_2$ in the CO_2 mixture. This observation suggests that OH

radical rate of productions might be influenced by the presence of CO_2. Thus, it is necessary to investigate the rate of production of this key specie in both mixtures and the results are summarized in Figure 5.28.

As could be observed from Figure 5.28, reactions $H_2O_2+M=OH+OH+M$ and $H_2+OH=H+H_2O$ are the most dominant reactions in producing and consuming OH radicals, respectively. However, the major difference is the significant role of reaction $HO_2+H=OH+OH$ in increasing the rate of production of OH in argon mixture, while this reaction does not have as high of the impact in OH production in the CO_2 mixture. This implies that due to a larger amount of H atom present in argon mixture (as shown in Figure 5.24) at the ignition time, the forward reaction rate of $HO_2+H=OH+OH$ increases while this reaction does not contribute much in OH production the CO_2 mixture due to a smaller mole fraction of H present during ignition. However, the third-body collision efficiency of reaction $H_2O_2+M=OH+OH+M$ in the CO_2 mixture is 60% higher than Ar in Aramco 2.0 mechanism. Therefore, the contribution of this reaction in the argon mixture is less than in the CO_2 mixture as this comparison could be noticed from Figure 5.28. Therefore, CO_2 exhibits a counterbalancing effect in governing ignition delay time of the mixture studied herein, when compared to an inert gas (in this case argon). In summary, the existence of a large CO_2 concentration in $H_2/CO/O_2/CO_2$=2.85:0.15:1.5:95.5 mixture causes the mole fraction of OH radical to remain approximately the same by two mechanism. First, due to a higher third-body collisional efficiency of CO_2 (compared to Ar) in reaction $H_2O_2+M=OH+OH+M$, the OH radical production is increased. Second, CO_2 causes the H atom mole fraction to be reduced at the ignition point, therefore making the effect of reaction $HO_2+H=OH+OH$ in OH production to be much less than the argon mixture. Thus,

these effects cancel out the change of OH productions eventually, and CO_2 does not change the ignition delay time of the mixture when compared with the mixture with argon bath gas.

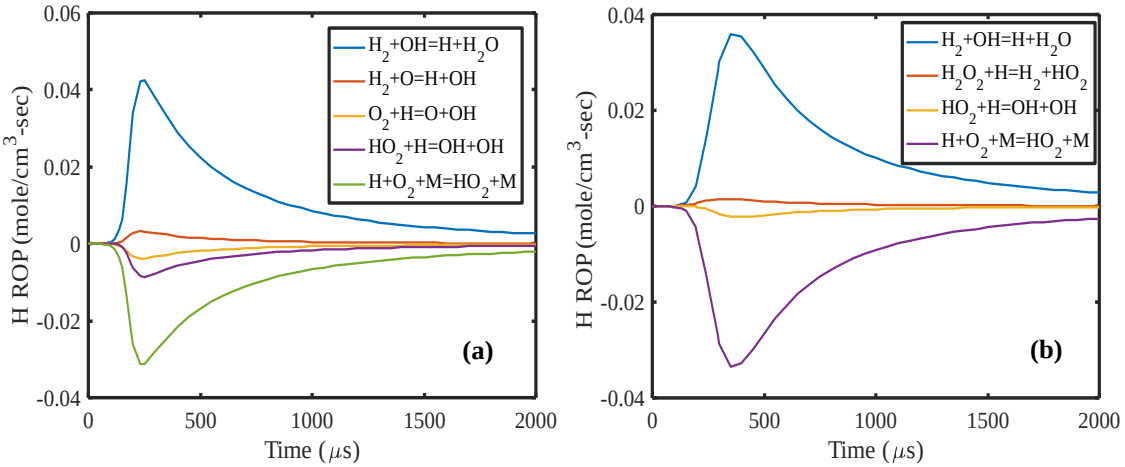

Figure 5.27. H Rate of Production (ROP) at 100 bar and 1200 K for a) $H_2/CO/O_2/Ar$=2.85:0.15:1.5:95.5 mixture and b) $H_2/CO/O_2/CO_2$=2.85:0.15:1.5:95.5 mixture

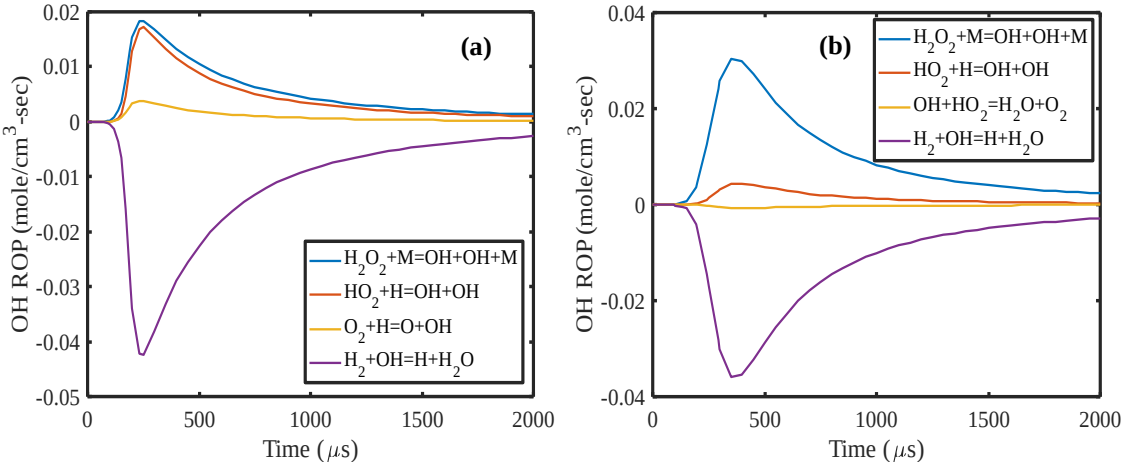

Figure 5.28. OH Rate of Production (ROP) at 100 bar and 1200 K for a) $H_2/CO/O_2/Ar$=2.85:0.15:1.5:95.5 mixture and b) $H_2/CO/O_2/CO_2$=2.85:0.15:1.5:95.5 mixture

CHAPTER 6. Conclusions and Future Works

6.1 Summary and Conclusions

Autoignition delay times for $CH_4/O_2/CO_2$, $CH_4/O_2/Ar$, $H_2/CO/O_2/CO_2$ and $H_2/CO/O_2/Ar$ mixtures for various mixture conditions are reported at 100 and 200 bar using a high-pressure and large-diameter shock tube. In these experiments, simultaneous sidewall and endwall emissions and pressure measurements are obtained. The acquired data are particularly important to interpret results for CO_2-rich mixtures, as shock bifurcation induces large uncertainties in the IDT. In this study, the combined effect of simultaneous sidewall and endwall measurements and the large ID of the tube is shown to reduce the uncertainty to approximately 15% for mixtures with CH_4 as a fuel and to approximately 20% for mixtures with H_2/CO=95:5 as fuel.

For $CH_4/O_2/CO_2$ and $CH_4/O_2/Ar$ mixtures, comparison between experimental data and kinetic models shows that the Aramco 2.0 kinetics model adequately captures ignition trends across all temperatures, pressures, and mixture compositions. Sensitivity analysis results emphasize the importance of the reactions: $2CH_3 (+M) = C_2H_6 (+M)$, $2HO_2 = H_2O_2+O_2$, and $CH_3+HO_2=CH_4+O_2$ in hindering ignition for both mixtures (with CO_2 and Ar). The experimental data from this study indicates that GRI 3.0 is not applicable at high pressure conditions, as a majority of its validation experiments were below 10 atm when it was developed. FFCM-1 could predict ignition at all conditions except at low temperature (below approximately1250 K), 200 bar for the $CH_4/O_2/CO_2$ mixture, owing to the missing CH_3O_2/CH_3OH kinetics. Reaction path flux analysis reveals that the ratio of carbon flux between the oxidation of methyl radicals (CH_3) to form methoxide (CH_3O) and the

recombination of this species to form ethane (C_2H_6) is the controlling parameter for ignition at 100 and 200 bar and temperatures greater than approximately 1250 K. However, at 200 bar and for temperatures below approximately 1250 K, the formation of methyldioxidanyl (CH_3O_2) becomes significantly important in promoting ignition. Removing CH_3O_2 and its corresponding reactions from Aramco 2.0 changes the ignition behavior dramatically at 200 bar and 1100 K, which highlights the impact of this species in ignition chemistry at low temperature conditions.

It is also found that carbon dioxide provides no significant chemical effect on ignition for $CH_4/O_2/CO_2$ mixtures when compared to experiments using argon as diluent. This observation, along with the shallow pressure rise during the post combustion process in CO_2-rich mixtures, suggests that CO_2 has a negligible chemical effect on ignition and that its influence on ignition is simply thermal, owing to its large heat capacity. This is because shock tube experiments only concern ignition kinetics where CO_2 formation is not critical. However, CO_2 could still have a chemical effect on flames and may require future investigation using different experimental approaches.

For $H_2/CO/O_2/CO_2$ and $H_2/CO/O_2/Ar$ mixtures, comparison between experimental data and kinetics models shows that the Aramco 2.0, FFCM-1, HP-Mech and USC Mech II kinetic models, properly capture ignition trends across all temperatures, pressures, and mixture compositions. Sensitivity analysis results emphasize the importance of the reaction: $H+O_2 (+M) = HO_2 (+M)$ in hindering ignition for both mixtures with CO_2 and Ar dilutions. The experimental data from this study indicates that GRI 3.0 is not applicable of capturing ignition delay times for $H_2/CO/O_2/Ar$ mixture. However, reducing the reaction rate of reaction $H+O_2 (+M) = HO_2 (+M)$ by 50% in this kinetic model, shows a major

improvement in predictions from this kinetic model. Reaction path flux analyses, by tracking hydrogen oxidation pathways, reveal that CO_2 does not alter any dominant pathways when compared to the argon case.

Examining the effect of pressure on ignition delay time of $H_2/CO/O_2/CO_2$=2.85:0.15:1.5:95.5 under supercritical conditions is done by comparing the sensitivity analysis results at 100 and 200 bar. While at 100 bar reactions $CO+OH=CO_2+H$ and $2HO_2=H_2O_2+O_2$ are shown to hinder the ignition and enhance the ignition respectively; however, their effect on the ignition was found to be opposite at 200 bar. This scenario is shown by implementing two kinetic models Aramco 2.0 and FFCM-1. As these mechanisms have many differences in their detailed chemistry, it is challenging to draw any definite conclusions regarding the details on how this phenomenon occurs as the pressure is doubled. However, implementing both mechanisms in simulations at 200 bar suggests that the mole fractions of H_2O_2 and CO are higher than for the 100 bar case.

Ignition delay time measurements of $H_2/CO/O_2/CO_2$ and $H_2/CO/O_2$/Ar mixtures at 100 bar show no significant differences when compared against each other. However, when sensitivity analyses, mole fractions, and rate of production of key species are investigated, interesting trends are found. Brute-force sensitivity analyses using Aramco 2.0 mechanism show many similarities between the reactions that enhance the ignition and hinder the ignition for these two mixtures. However, a discrepancy is found from this analyses regarding reaction $CO+OH=CO_2+H$ where it appears as one of the reactions to hinder ignition for the CO_2 mixture, while it shows to accelerate ignition in the Ar mixture.

To explain the opposite effect of reaction $CO+OH=CO_2+H$ on CO_2 and Ar mixtures, mole fractions of OH, H, CO, and HO_2 are obtained using Aramco 2.0 mechanism. While for both mixtures OH and HO_2 mole fractions are almost identical, the mole fractions of H and CO show opposite trends. Mole fraction of H atoms is found to be much higher in case with Ar dilution, while CO mole fraction is found to be much higher in the CO_2 mixture when compared against each other.

Inspecting the rate of production of CO suggests that $CO+OH=CO_2+H$ is the main reaction in consuming CO in the argon mixture, while on the contrary, it is the most dominant reaction in production of CO in the CO_2 mixture. On the other hand, when H atom rate of productions for both diluents are compared, reactions $H_2+OH=H+H_2O$ and $H+O_2+M=HO_2+M$ are shown to be the most dominant reactions in producing and consuming H radicals, respectively. One should be careful in interpreting analyses here, as there are differences such as reactions $H_2+O=H+OH$ and $O_2+H=O+OH$ in the argon mixture being replaced by $H_2O_2+H=H_2+HO_2$ in the CO_2 mixture. This observation suggests that OH rate of production is important to investigate.

Even though the mole fraction of OH radical for argon and CO_2 mixtures are nearly identical at the ignition point, the rate of production points out an important difference between the two. It is found that due to a higher H atom mole fractions in the Ar mixtures than in the CO_2 mixtures, reaction $HO_2+H=OH+OH$ increases the rate of production of OH in argon mixture, while this reaction does not have as much impact in OH production in the CO_2 mixture. However, since CO_2 has a larger collision efficiency than Ar (by 60% in reaction $H_2O_2+M=OH+OH+M$), the contribution of this reaction in the CO_2 mixture in OH rate of production is larger than for mixtures with Ar as a diluent. Therefore, CO_2 has a

counterbalancing effect in governing ignition delay time of the mixture studied herein, when compared to an inert gas.

Real-gas thermodynamic effects on kinetic model simulations at 100 and 200 bar suggest that the difference in IDT, when using the ideal gas equation of state is less than 5% at maximum. Therefore, the ideal gas equation of state appears to be a satisfactory choice at the supercritical conditions of this study, where the experimental uncertainty in reporting IDT is 15–20%. Furthermore, the mixtures compressibility factors are found to be very close to unity, justifying the use of the ideal gas equation of state in the simulations at high pressure and temperature conditions.

6.2 Future Works

Ignition delay time (IDT) information play an important role in supercritical CO_2 oxy-combustion applications. Whether it is from combustor design point of view or future chemical kinetics developments, IDT is one of the key parameters to be considered. In this dissertation, the chemical effect of carbon dioxide and the effect of pressure under supercritical conditions were investigated for methane and a syngas mixture. However, there are other interesting and yet important aspects of the problem that could be investigated in future.

Speciation measurements are often implemented in shock tube experiments to obtain deep insights into the rate of consumption or production of specific species. Such information could be very beneficial in predicting the reaction rates of important reactions governing ignition delays. Typically, direct absorption spectroscopy by implementing Tunable Diode Laser Absorption Spectroscopy (TDLAS), gas chromatography or mass

spectrometry are used for this purpose. While TDLAS could be done on the shock tube facility presented here for multiple species simultaneously, however the well-known pressure broadening effect prohibits its application at high-pressure conditions. For the pressure conditions relevant to sCO_2 oxy-combustion systems, the facility could be modified to incorporate more promising methodologies such as gas chromatography or mass spectrometry and gain useful information regarding stable species (such as carbon monoxide) concentration time histories. Developing optical diagnostic techniques such as high-speed imaging at elevated pressures are also useful to provide more information regarding the fluid mechanics of the shock-boundary layer interaction and ignition homogeneity at elevated pressures. This task could be challenging due to the limited optical access size availabilities in high-pressure shock tubes with large diameters, while it is extremely advantageous.

In this thesis, only two types of fuels were studied while there are other candidates for this application. For example, the syngas mixture studied here consisted of 95% H_2 and 5% CO. This ratio was selected due to the constraints on the laboratory facilities and safety considerations. It was shown in this thesis that reactions involving carbon monoxide (for instance, reaction $CO+OH=CO_2+H$) could influence the ignition delay times. Therefore, it is necessary to investigate the extent in which CO concentration could alter the ignition chemistry of syngas. To further understand such effect, a parametric study on CO concentration could be done by increasing its percentage in the fuel up to 95%. It was previously shown that in inert bath gases (such as argon or nitrogen), increasing the percentage of CO/H_2 ratio beyond 50:50 changes the ignition delay times and alters the oxidation pathways substantially. Whether such a conclusion still holds under highly

diluted sCO_2 environment is unknown and requires further experimental efforts. In a similar scenario, various types of natural gas mixtures could also be suited at similar conditions. Even though the main component of natural gas is methane, but the effect of addition of small percentage of other constituents such as ethane, propane or butane could have considerable effects on ignition chemistry under highly diluted CO_2 environments at supercritical conditions.

Finally, related to the operation of sCO_2 power cycles is the amount of soot generated at elevated pressure and temperature conditions. Information regarding soot generation from the combustion process is mainly important for heat exchanger developments of the cycle. Large amount of soot formations during combustion process could mitigate the current heat exchanger designs and increase the need for investigating alternatives in that regard.

APPENDIX A. Details of Experimental Conditions

Details of experimental conditions for each mixture are listed in the following tables. These include the initial mixture temperature in driven section (T_1), initial mixture pressure in driven section (P_1), the incident Mach number ($M_{incident}$), temperature on the reflected shock (T_5),), average pressure on the reflected shock (P_5), and the ignition delay time (τ_{ign}). The first five tables summarize the conditions for mixtures with methane (CH_4) as fuel and the second four tables summarize the conditions for mixtures with H_2/CO=95:5 as fuel.

Table A.1. Experimental conditions for stoichiometric mixture of $CH_4/O_2/CO_2$=5:10:85 at 100 bar

Mixture 1 ($CH_4/O_2/CO_2$=5:10:85)						
Run	T_1 (K)	P_1 (bar)	$M_{incident}$	T_5 (K)	P_5 (Avg.) (K)	τ_{ign} (μs)
1	294	0.597	4.13	1433	95.2	206
2	294	0.599	4.13	1426	98.3	204
3	295	0.597	4.1	1416	94.1	242
4	295	0.644	4.09	1411	101.8	226
5	295	0.666	4.03	1383	105.3	242
6	296	0.708	3.95	1349	100.5	504
7	296	0.685	3.93	1339	96.7	744
8	293	0.697	3.88	1307	100.02	416
9	298	0.802	3.83	1296	107.6	458
10	296	0.709	3.84	1293	94.2	584
11	296	0.847	3.79	1274	109.2	782

Table A.2. Experimental conditions for rich mixture (Φ=2) of $CH_4/O_2/CO_2$=10:10:80 at 100 bar

Mixture 2 ($CH_4/O_2/CO_2$=10:10:80)						
Run	T_1 (K)	P_1 (bar)	$M_{incident}$	T_5 (K)	P_5 (Avg.) (K)	τ_{ign} (μs)
1	297	0.595	4.05	1383	94.1	350
2	295	0.68	3.97	1343	99.7	438
3	297	0.742	3.86	1297	101.2	626

Table A.3. Experimental conditions for stoichiometric mixture of CH_4/O_2/Ar=3:6:91 at 100 bar

Mixture 3 (CH_4/O_2/Ar=3:6:91)						
Run	T_1 (K)	P_1 (bar)	$M_{incident}$	T_5 (K)	P_5 (Avg.) (K)	τ_{ign} (μs)
1	298	3.5	2.35	1248	90.8	1532
2	298	3.2	2.46	1354	93.6	516
3	298	3.0	2.52	1410	93.8	242
4	298	3.35	2.44	1336	95.2	550
5	298	3.45	2.43	1325	97.4	620

Table A.4. Experimental conditions for stoichiometric mixture of $CH_4/O_2/CO_2$=5:10:85 at 200 bar

Mixture 4 ($CH_4/O_2/CO_2$=5:10:85)						
Run	T_1 (K)	P_1 (bar)	$M_{incident}$	T_5 (K)	P_5 (Avg.) (K)	τ_{ign} (μs)
1	297	2.05	3.48	1139	195.5	1050
2	338	2.07	3.43	1230	199.1	540
3	355	2.25	3.37	1250	211.7	458
4	314	2.19	3.41	1156	211.9	842

Table A.5. Experimental conditions for stoichiometric mixture of $CH_4/O_2/Ar=2:4:94$ at 200 bar

Mixture 5 ($CH_4/O_2/Ar=2:4:94$)						
Run	T_1 (K)	P_1 (bar)	$M_{incident}$	T_5 (K)	P_5 (Avg.) (K)	τ_{ign} (μs)
1	298	8.5	2.35	1293	213.7	1016
2	298	9.0	2.31	1253	218.9	1310
3	297	8.0	2.39	1323	211.9	734
4	298	7.5	2.44	1379	210.8	464

Table A.6. Experimental conditions for stoichiometric mixture of $H_2/CO/O_2/CO_2=2.85:0.15:1.5:95.5$ at 100 bar

Mixture 1 ($H_2/CO/O_2/CO_2=2.85:0.15:1.5:95.5$)						
Run	T_1 (K)	P_1 (bar)	$M_{incident}$	T_5 (K)	P_5 (Avg.) (K)	τ_{ign} (μs)
1	291	0.70	4.04	1365	103.9	40
2	292	0.85	3.73	1224	101.9	144
3	293	0.90	3.74	1230	106.2	140
4	292	0.95	3.64	1186	106.3	258
5	292	0.80	3.78	1249	89.35	104
6	292	0.70	3.95	1329	98.1	50

Table A.7. Experimental conditions for stoichiometric mixture of $H_2/CO/O_2/Ar=2.85:0.15:1.5:95.5$ at 95 bar

Mixture 2 ($H_2/CO/O_2/Ar=2.85:0.15:1.5:95.5$)						
Run	T_1 (K)	P_1 (bar)	$M_{incident}$	T_5 (K)	P_5 (Avg.) (K)	τ_{ign} (μs)
1	293	4.0	2.3	1265	93.0	79
2	293	4.5	2.24	1212	95.4	192
3	294	4.8	2.22	1196	101.4	270
4	295	3.7	2.30	1275	88.3	72

Table A.8. Experimental conditions for rich mixture (Φ=2) of $H_2/CO/O_2/CO_2$=5.7:0.3:1.5:92.5 at 85 bar

Mixture 3 ($H_2/CO/O_2/CO_2$=5.7:0.3:1.5:92.5)						
Run	T_1 (K)	P_1 (bar)	$M_{incident}$	T_5 (K)	P_5 (Avg.) (K)	τ_{ign} (μs)
1	289	0.80	3.61	1175	83.7	287
2	288	0.75	3.68	1204	84.4	189
3	290	0.70	3.78	1254	86.7	96
4	290	0.65	3.84	1280	81.9	77

Table A.9. Experimental conditions for stoichiometric mixture of $H_2/CO/O_2/CO_2$=2.85:0.15:1.5:95.5 at 200 bar

Mixture 4 ($H_2/CO/O_2/CO_2$=2.85:0.15:1.5:95.5)						
Run	T_1 (K)	P_1 (bar)	$M_{incident}$	T_5 (K)	P_5 (Avg.) (K)	τ_{ign} (μs)
1	292	2.0	3.59	1257	212.9	95
2	292	1.8	3.68	1202	207.3	190
3	292	1.6	3.80	1161	203.9	322

APPENDIX B. Experimental Approach and Procedures

This appendix describes the details of operating the shock tube, which is mainly divided into three sections:

1. The cleaning and inspection of the shock tube prior to conducting any experiments
2. The steps taken during mixture preparation and pressurizing the tube
3. The procedures to be followed once the shock is successfully fired and the tube is drained

The safety operating procedures at each of these parts are presented below.

The preparation of the tube begins with checking the pressure in each helium bottle connected to the driver section of the tube. Every bottle located in the 8-pack of 3,000 psi (~206 bar) bottle rack is checked for their pressure levels and a small note regarding the supply pressure is made on the bottle. Bottles that contain pressures lower than 500 psi (~34 bar) are discarded from the rack and considered empty. Once the pressure on each bottle is checked and noted, the flexible hoses (that connect each bottle to its designated regulator) are secured and are ensured to be twist-free. Following this step, leak tests are conducted on each end connections of the hose to ensure the fill system is not leaking. Furthermore, no loose connections should be spotted upon pressurizing the associated connections to full bottle pressure (approximately 3,000 psi (~206 bar)). The same procedures are conducted on the boost tank (set at 6,000 psi (~413 bar)). It should be mentioned that the boost tank must be kept exactly at 6,000 psi (~413 bar); otherwise a

burst of 2,600 psi (~180 bar) is extremely hard to achieve on the driver section of the tube. Figure B.1 shows the picture of the fill system assembly.

Figure B.1. Driver fill system connections

Once the supply bottle racks are prepared, the entire inner surface of the shock tube is cleaned. The cleaning procedure consists of two parts. First, a dry-cloth connected to a mop rod is used to collect any remaining pieces of diaphragm residues left inside the tube from previous experiments. Once all the pieces are recovered, a separate cloth containing acetone is used to remove any combustion-product residues on the surface of the tube. This step is done until a satisfactory results are obtained. The importance of this step is highlighted in two phenomena that could negatively affect the performance and the quality of data obtained. A large level of dirt causes the ignition delay time to drift to a shorter value as the number of reacting experiments increases and various fuels are tested. Furthermore, upon applying high vacuum, the dirt on the wall surface starts to come off and weaken the vacuum pumps power level. Consequently, longer vacuuming time will be required and the lower limit of vacuum pressure increases over time, making it difficult to achieve pressure as low as 10^{-6} Torr. Therefore, it is recommended for the tube to be dry-

cleaned and acetone-cleaned after each run. Figure B.2 shows a picture of the dry-clean cloth and the tube preparation for cleaning.

Figure B.2. Dry-clean cloth for diaphragm pieces recovery

Following the cleaning process of the tube is diaphragm selection and placement in the diaphragm section. Depending on the targeted reflected shock pressure and temperature conditions, a compression ratio is calculated and eventually a narrow range of burst pressure is selected. Using a historical diaphragm data over three years, the appropriate diaphragm is selected and placed in the diaphragm section. It should also be noted that the diaphragm is also wiped and cleaned with acetone to remove residues left over from machine shopping and water jetting works. The driver section is then rolled back by mechanical winches installed on the driver section support frame and diaphragm is placed in its designated location with scored side of the diaphragm facing the low pressure side.

Once the orientation of the diaphragm is ensured to be correct, the driver section is rolled back in place till the diaphragm is in contact with O-rings on the high-pressure and low-pressure sides. The tie-nut rods are then locked in place via a shear plate and the hydraulic pressure is pumped to approximately 185 bar to ensure the diaphragm is completely sealed in place on either sides. It should be noted that this pressure is kept on the diaphragm section until the experiment is completed and the tube is drained. Throughout the duration of the experiment, the hydraulic pressure is checked multiple times to ensure of normal operation of the subsystems and no pressure drops have occurred.

The next step in preparing for experiments is mixture preparation. Prior to preparing the mixture of interest, the driven section of the tube, the mixing vessel facility, and their tubing connections to the gas supply bottles are vacuumed. Thus, a pressure value in the order of 10^{-6}–10^{-5} Torr is achieved by using two dry scroll pumps and two turbomolecular pumps. One of the vacuum pump setup is used on the shock tube and the second one is used on the mixing vessel and its tubing connections. Due to the large volume of the shock tube and the mixing vessel, achieving a low vacuum level could be time consuming. Therefore, both vacuum pumps are used simultaneously and it was shown that the desired pressure level for the driven section of the tube and the mixing vessel could be obtained in approximately two hours. Once this pressure is achieved, the vacuum pump used on the driven section is isolated by the means of the contour valve. The same hydraulic system that was used in sealing the diaphragm section is capable of supplying the same pressure (185 bar) to the reciprocating piston-valve on the contour valve section of the tube. An O-ring housing is used to seal the piston in place upon applying the hydraulic pressure. Similar to the hydraulic pressure of the diaphragm section, throughout the duration of the

experiment, the hydraulic pressure on the contour valve is also checked multiple times to ensure this subsystem is operating normally and no pressure drops have occurred. If at any point during the operation of tube a drop in hydraulic pressure is noticed, the experiment is quickly stopped until the problem is resolved. Figure B.3 shows a picture of the pressure gauge and isolation valves of the hydraulic systems.

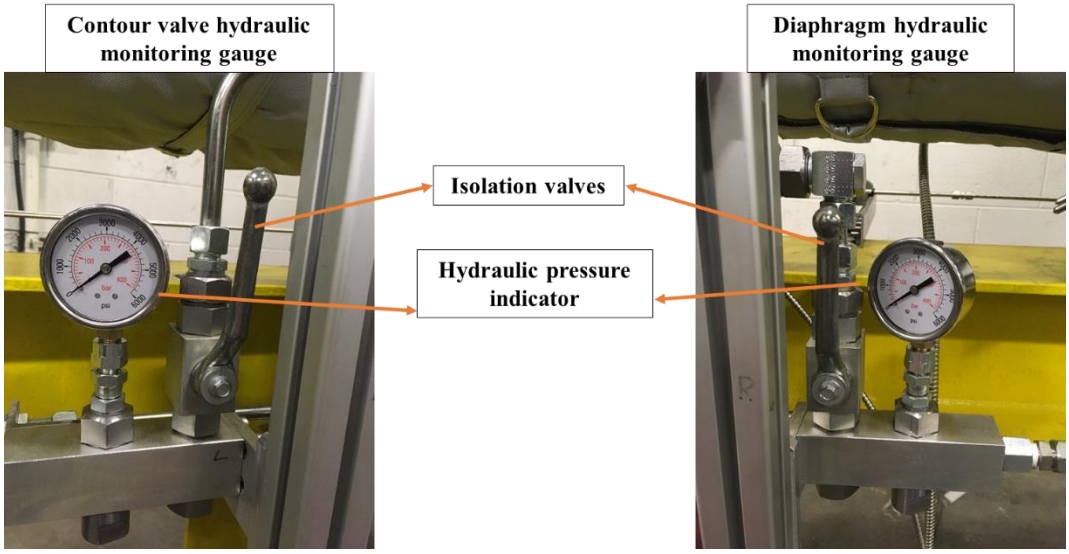

Figure B.3. Hydraulic pressure gauge and isolation valves

After about two hours of vacuuming, the mixture of interest is prepared. Depending on the experimental condition, the mixture could be prepared in the mixing vessel and then fed in the driven section or prepared in the vessel and shock tube simultaneously. Ideally, it is preferred for the mixture to be prepared in the mixing vessel since it can be stirred for some times to ensure sufficient mixing between constituents has achieved prior to transferring it to the driven section of the tube. However, for certain experimental cases, mixture preparation in the vessel is not practical due to the allowable designed pressure of the mixing vessel. In these cases, the mixture is prepared in the driven section, however to

ensure of sufficient mixing, it is rested in the driven section for couple of hours. This mixing technique merely relies on the diffusion of constituents in the driven section.

Mixture preparation starts by calculating the amount of total mixture required to be in the driven section. This is obtained from the target compression ratio found during the diaphragm selection process. Following that, the partial pressures of fuel, oxidizer and dilute are calculated and using high-accuracy Baratrons absolute pressure sensors, the mixture is prepared. It should be mentioned that to maximize the ability on controlling the rate at which each constituents is introduced to the mixture, three needle valves and three solenoid valves are used in series. They are equipped with pulse switches located downstream of the regulators from fuel, oxidizer, and dilute bottles. Figure B.4 shows the absolute pressure sensors and the valves that are used for controlling fill rate of the constituents.

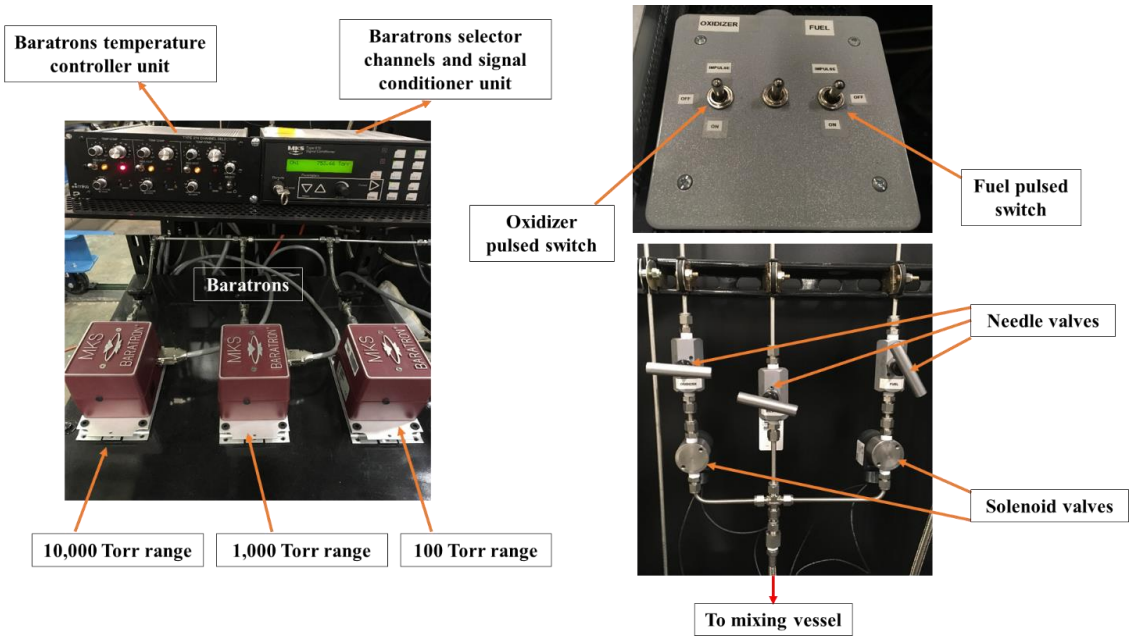

Figure B.4. Mixing facility pressure sensors and various valves used in the setup

While the mixture sits in the driven section for couple of hours, the driver section is vacuumed and appropriate settings are applied to the data acquisition system. The driver vacuuming procedure is not as rigorous as in the driven section and a pressure value of couple of milliTorrs is found to be sufficient prior to filling this section with helium gas. While the driver section vacuuming is ongoing, the sensors on the test section is checked for their normal operations and noise levels.

Once the signal conditioners for PCB sensors are turned on, their noise levels are checked on the frequency counters. The maximum noise level requires to be lower than 10 mV to avoid any premature triggering of the sensors during the experiment. The desired noise levels are achieved and monitored for 100 seconds on the BNC software. Then the frequency counters are armed and stay on trigger mode till the shock is fired and the timing between each two consecutive PCBs is recorded. Figure B.5 shows a schematic of the PCB sensors used for data acquisition triggering and shock velocity measurements. The noise levels of the Kistler sensors and Photomultipliers are checked in a similar manner, however this is done on a LabVIEW code utilizing a compactRIO setup and appropriate modules for data collections. The code is also capable of controlling actuators, temperature measurements, and recoding the dynamic pressure values and emission signals.

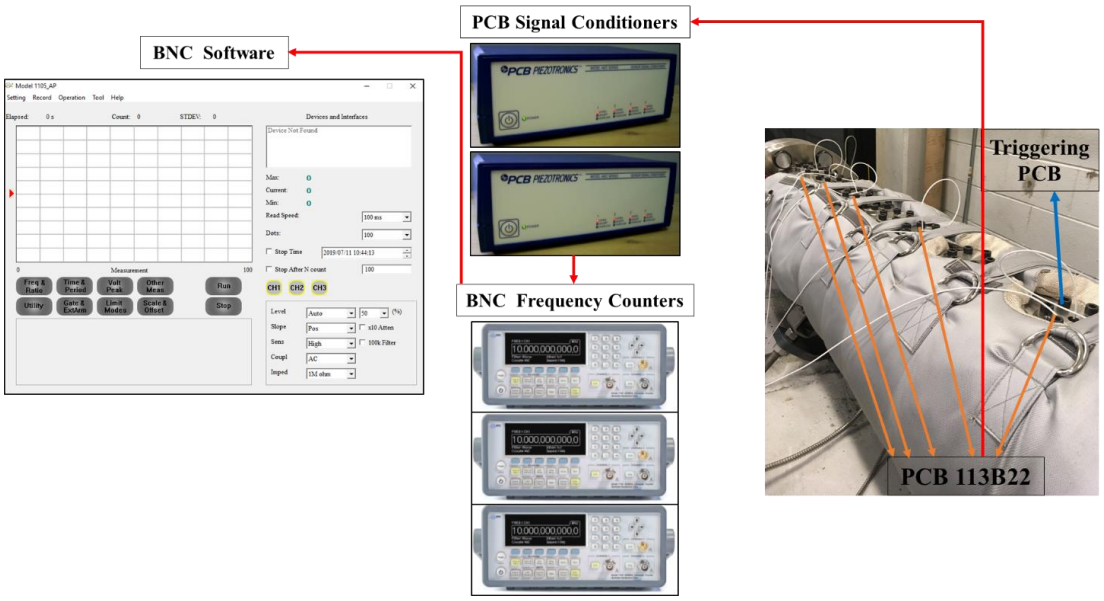

Figure B.5. PCB sensors and BNC frequency counters

Once all data acquisitions systems are armed, the lights in the lab are turned off to avoid inducing any extra noise levels on the photomultipliers. Then all the access valves on the driven section of the tube are closed and isolated and the driver vacuum pump is turned off and its access valve to the tube is closed. The hydraulic pressure values on the contour valve and on the diaphragm section are checked to ensure of holding 185 bar of pressure. At this point, the driver section is pressurized to 200–300 psia (~13–20 bar) and the entire tube is inspected for the last time prior to increasing the fill pressure to higher values. The filling process of the tube continues until the diaphragm is burst and the shock is fired. The data collection is checked for proper triggering and the frequency counters timing values are recorded. The tube is fully drained subsequently and hydraulic pressures are removed from the diaphragm section and the contour valve section. Eventually, the tube is opened and inspected for any potential damages after conducting each high-pressure experiment.

APPENDIX C. General Shock Tube Design and Operation

The shock tube, designed and manufactured as covered in this section and associated design calculations and drawings, forms only part of an overall system. The tube itself has standard bolted connections with simply actuated contour valve and hydraulic ram. It is the responsibility of the end user to ensure method statements for the correct use of the tube are developed as the end user will design the system that controls the following operational requirements of the shock tube:

- Filling the tube with test gases via connected pipe work system and associated control
- Initiating experiment via controlled pressure differential across diaphragm in single diaphragm mode
- Initiating experiment via evacuation between diaphragms in double diaphragm mode
- Removal of test gases after experimentation via provided plugs or prior to experiment should the experiment be aborted
- Applying preheat temperature to the tube and control thereof

C.1 Diaphragm Section and Contour Valve Section Operations

A hydraulic ram is incorporated to the diaphragm section to remove the need of undoing a bolted connection as shown in Figure C.1. As this is not like a standard bolted connection care needs to be taken to ensure the correct steps are taken in order to allow safe disengagement of section. The sequence of works detailed here are from the closed position with hydraulic load applied as it would be after performing an experiment.

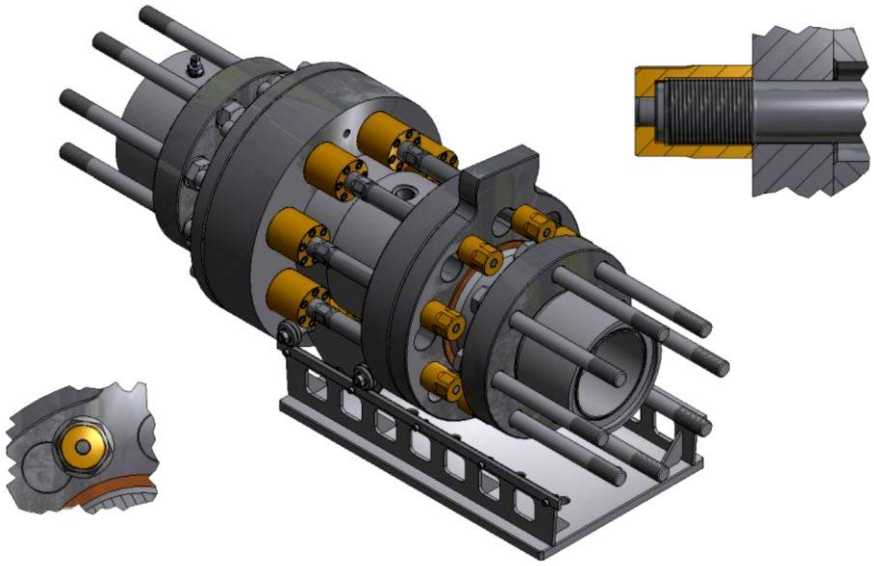

Figure C.1. Ram in its locked position with the pressure inside the ram housing forcing the piston back and applying pressure to the shear plate and tie rod support flange

As shown in Figure C.1, the tie rod nut and shear plate are engaged. Note the shear plate groove orientation in the top left of Figure C.1 and the neck of the tie rod engaged with the chamfered hole on the reduced side of the slot in the bottom left of Figure C.1. The shear plate resists only the shear witnessed while under the load provided by tie rods. The tie rod flange acts to guide the tie rods during the assembly and disassembly, but also provides the strength to minimize deformation when under load. When under load, the shear plate and tie rod flange are pulled against the shoulder of the driver tube extension. Similarly, the ram housing is pulled against the shoulder of the driven tube extension.

When the hydraulic pressure is released from the ram, the springs in the ram housing push the ram piston and tie rods back to their home position, slacking off the tie rod nuts from the shear plate allowing it be rotated by 15 degrees so that the tie rod nuts are now in the clearance portion of the shear plate slot as shown Figure C.2.

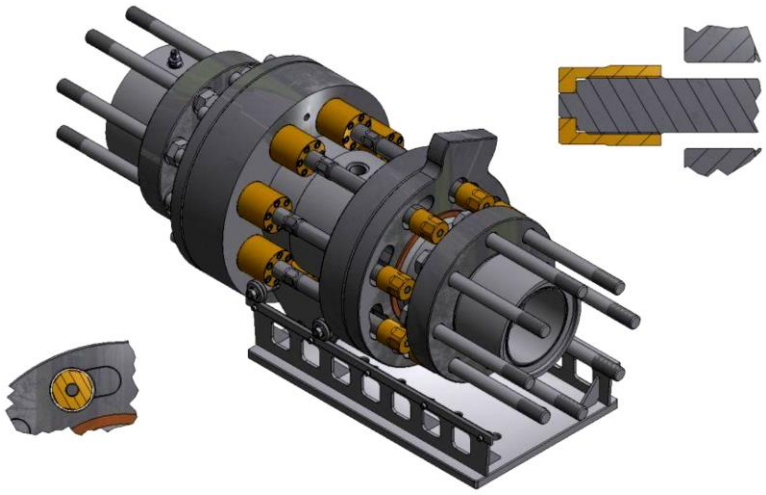

Figure C.2. Pressure in the ram housing is released allowing the springs to push the ram piston home which in turn pushes the tie rods away from the shear plate

Now the connection is essential free, where the driven side of the ram where the ram housing is located, and driver side of the ram being the shear plate and tie rod flange can now be separated. The driver side of the shock tube can be rolled back on its roller supports to allow access to remove the diaphragms from the driven and driver tube extensions.

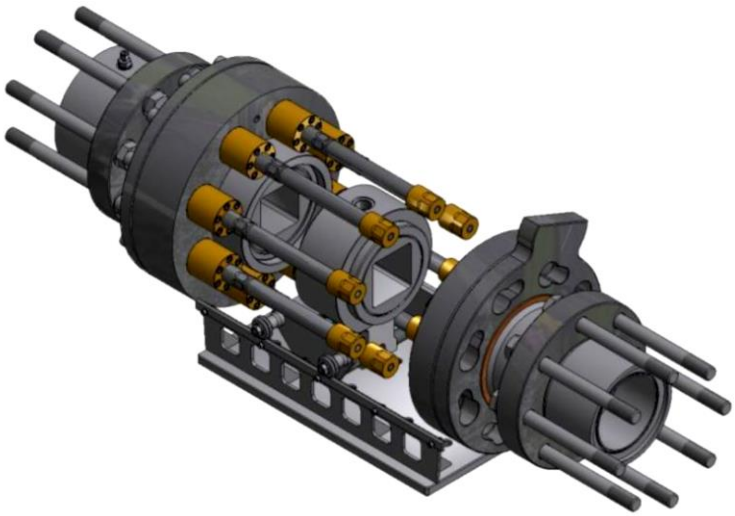

Figure C.3. Movement of the driver section on its support frame as well as the mid-section on its carriage allows removal and replacement of diaphragms

The diaphragm mid-section (see Figure C.3) is supported on a carriage and guide plate for ease of movement of the diaphragm mid-section. Once the driver side of the diaphragm section is sufficiently moved back, the used diaphragms can be removed and replaced. The diaphragms are placed into the registers of the driver and driven tube extensions where the diaphragm mid-section registers. The diaphragm mid-section is then pushed back into the registering face of the driven tube extension, followed by rolling the driver section of the shock tube so that the tie rod nuts are back through the shear plate. The shear plate is then rotated to engage with the tie rods and hydraulic pressure is applied 185 bar. See next section for hydraulic operation of the diaphragm ram.

C.2 Hydraulic System

The hydraulic system can be broken down to four separate sub-systems each with their own specific tasks. The following section explains the task of each sub-section and how it interacts with the connected sub-systems. Simplified schematic of the hydraulic system operation could be seen in Figure C.4.

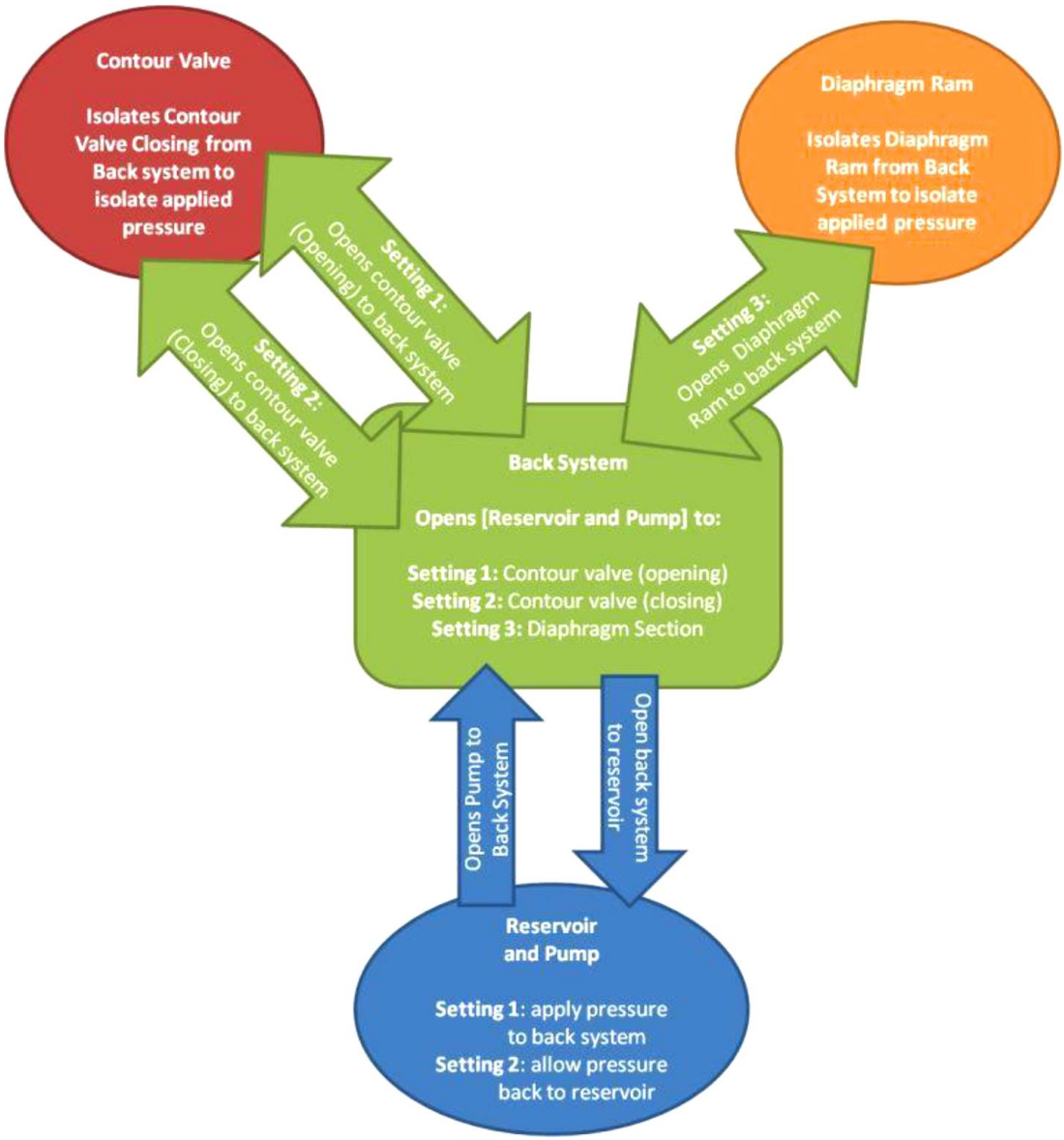

Figure C.4. Simplified schematic of the Hydraulic System

Back system opens the pump and reservoir to allow oil (and hence pressure) to and from either the contour valve rams or the diaphragm section ram. There are three lines (routes) the back system can allow pressure to be applied or released (i.e. allows pump to apply pressure, or allows applied pressure to be dumped back to reservoir): 1) Contour valve opening 2) Contour valve closing and 3) Diaphragm section.

The back system has a pressure gauge to show what pressure is in the back system. The pump and reservoir do the following operations:

1) Applies pressure (by pumping hydraulic oil from the reservoir) to the back system (from where the back system routes to the chosen line)

2) Open back system to reservoir allowing pressure from back system to reservoir

When applying pressure, the pump is open to the back system but the reservoir is closed to back system. The pump has a check valve that only allows hydraulic oil to flow in one direction while pumping and hence pressure can be applied. Opening the reservoir to the back system allows pressure from the back system to return to reservoir.

When the back system has selected the line for contour valve opening, pressure applied by the pump acts on the opening side of the contour valve ram pistons causing the contour valve to open and when the back system has selected the line for contour valve closing, pressure applied by the pump acts on the closing side of the contour valve ram pistons causing the contour valve to close. When closing the contour valve, pressure needs to be retained. A ball valve allows the pressure applied to the contour valve closing line to be isolated from the back system. A pressure gauge specific to this line on the contour valve side of the ball valve shows retained pressure. When opening the contour valve, pressure does not need to be retained. As such there is no need to isolate the opening line from the back system. The back system pressure gauge will show how much pressure is being applied to open. This does not require high positive pressure when opening and any remaining pressure after opening that is witnessed in the back system pressure gauge can

be returned to reservoir by opening the reservoir to the back system via the pump valve as could be seen in Figure C.5.

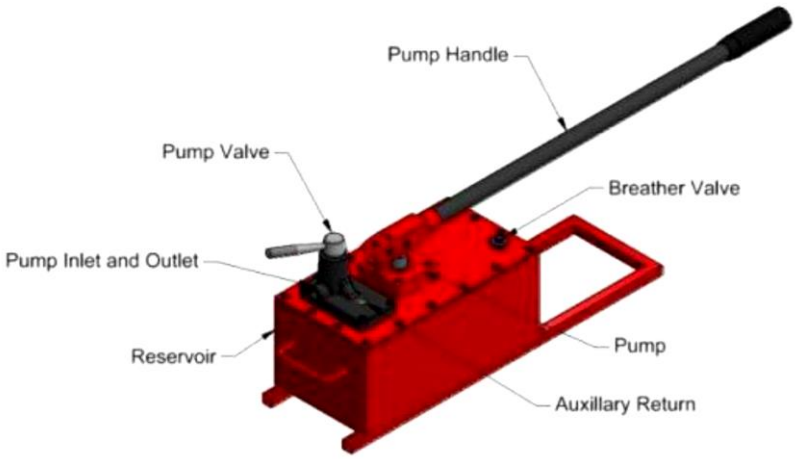

Figure C.5. Pump and Reservoir Components

When the back system has selected the diaphragm ram line, pressure applied by the pump causes the diaphragm ram to close and when the reservoir is open to the back system and the back system has selected the diaphragm ram line, the pressure is routed back to the reservoir. The pump valve selects either the pump or reservoir to be open to the back system, see Figure C.6.

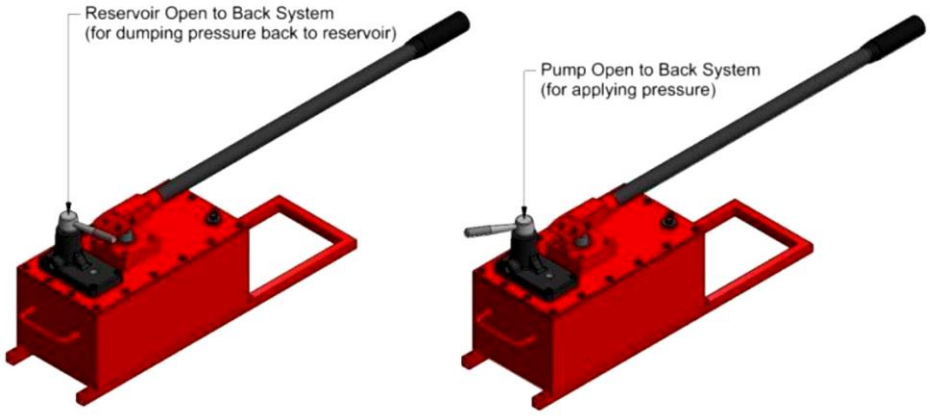

Figure C.6. Reservoir and pump selection

The pump is operated via the pump handle. Pushing the handle down displaces oil from the pump to the back system. Pulling up the pump handle fills the pump with hydraulic oil from the reservoir. The pump has two modes of operation: low pressure (high volume) application and high pressure (low volume) operation. Low pressure application allows for the quick transfer of fluid to for moving the contour valve ram pistons and moving the diaphragm piston. However, it won't be able to apply locking pressure. When the line chosen by the back system does not have applied pressure, the pump will automatically be in high volume low pressure application. As pressure begins to build, it will become difficult to actuate the pump handle. To switch to high pressure mode, apply firm pressure to pump handle downwards. Slowly lift the handle and further actuation downward should now start applying low volumes of oil but high increases in pressure. In low pressure mode, a large piston is actuated to move the fluid. In high pressure mode, a small piston is actuated to move the fluid.

The reservoir can be selected via the pump valve, see Figure C.5. When the reservoir is open to the back system pressure cannot be applied by the pump. When the reservoir is opened to the back system, pressure in the back system is returned/dumped to reservoir. When the pump is open to the back system, pressure in the back system cannot return to reservoir. However, displaced oil when operating the contour valve returns to the reservoir via the auxiliary return, refer to Figure C.5 and Figure C.7.

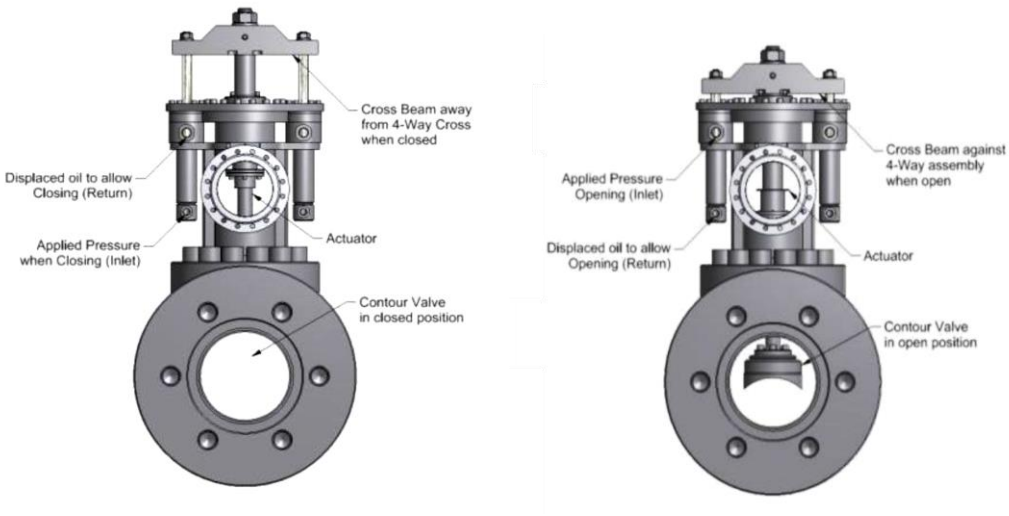

Figure C.7. Contour valve positions and visual identification

When selected via the back system, the contour valve can be opened and closed. As both rams are dual acting, pressure acts on one side of the ram pistons to close and the other to open. This means during operation, oil is displaced by the moving piston and this goes back to the reservoir via the auxiliary return, see Figure C.5 and Figure C.7. The auxiliary line does not need to be opened or closed and is automatically engaged when the back system has chosen opening or closing of the contour valve.

The back system is an arrangement of valves that allows selection of two separate systems - the diaphragm section and the contour valve. The diaphragm section is a single line, where pressure is applied or pressure is released back to the reservoir. The contour valve has two lines, one for opening, and one for closing. In either setting, pressure is applied and released through a single line, but as the rams are dual acting there is an auxiliary return line for displaced oil that is automatically open to the reservoir. Pressure in the back system can be checked at the back system pressure gauge, see Figure C.8.

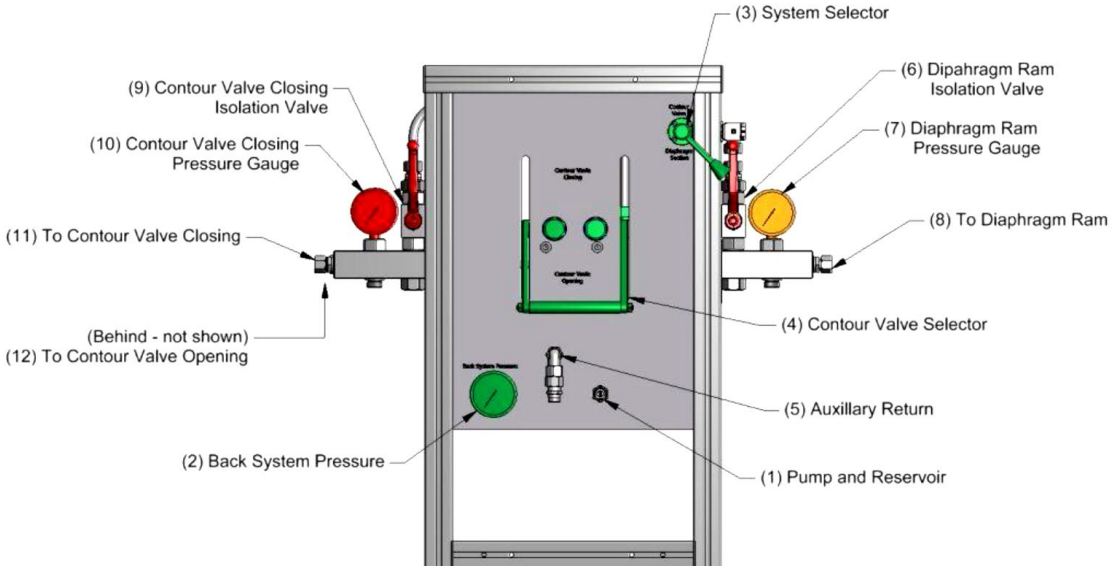

Figure C.8. Back system layout showing main components

Referring to Figure C.8 the following are the main components of the system. (1) Pump and reservoir line: This is the line through which pressure is either applied via the pump or returned to reservoir. (2) Back system pressure gauge: The pressure being applied to the back system or retained in the back system can be witnessed at this gauge. (3) System selector - diaphragm operation or contour valve operation.

The pump and reservoir line (1) is connected to a three-way valve (3) that will either route the pressure to the diaphragm section ram or the contour valve rams. If the handle is up, it will route to the contour valve rams. If the handle is down, it will route to the diaphragm section ram. (4) Contour valve selector: opening and closing the central lever handle (4) is specific to the contour valve operation and does not have any effect on operating the diaphragm section.

When the contour valve is selected via valve (3) in the up the position, and the central lever handle (4) in the down position, this will allow the contour valve to be opened. When the contour valve is selected via valve (3) in the up the position, and the central lever handle (4) in the up position, this will allow the contour valve to be closed. (5) Auxiliary return: the auxiliary return line does not require user selection and is automatically routed to reservoir via the back system when selecting contour valve opening or closing via lever handle (4). This allows displaced oil when operating the contour valve rams to return to reservoir. It has no function when operating the diaphragm section ram. (6) Diaphragm isolation valve: when diaphragm operation is selected via (3) i.e. in the down position, the diaphragm isolation valve (6) when open allows pressure applied via the pump to act on the diaphragm section ram, causing it to close the connection. When open, it can also let pressure from the diaphragm section ram back to the reservoir by opening the back system to the reservoir (refer to Figure C.6) to allow opening of the diaphragm section for diaphragm removal.

When closing the diaphragm section, the pump valve should be in the pump selected position (pressure can be applied), refer to Figure C.6. Pressure can be applied and witnessed via the back system pressure gauge (2) and the diaphragm pressure gauge (7) which both should read the same value when applying pressure. To retain the pressure applied to the diaphragm section after achieving locking pressure (185 bar) the diaphragm isolation valve (6) should be closed (horizontal). After testing and evacuation of the driven and driver Sections, the diaphragm section locking pressure can be released back to the reservoir by having the reservoir open to the back system and the diaphragm ram selected via valve (3). The diaphragm isolation valve (6) can be opened (moved to vertical position)

allowing pressure back to reservoir. Prior to replacement of diaphragms, the diaphragm section pressure gauge should be checked and should read zero.

(7) Diaphragm pressure gauge: The diaphragm pressure gauge is on the diaphragm ram side of the diaphragm isolation valve (6). As such, even when the diaphragm is isolated from the back system (diaphragm isolation valve in a horizontal position) pressure in the diaphragm ram can always be checked. (8) Diaphragm line: The diaphragm ram is supplied with pressure (hydraulic oil) via the line exiting this point. (9) Contour valve closing isolation valve: After performing a test (bursting diaphragms) and after evacuating the shock tube of test media, the contour valve will need to be closed to allow filling of the driver section with the next test media. The contour valve requires positive pressure to compress the valve O-ring and ensure a tight seal prior to application of test media and positive pressure in the driven section. When applying locking pressure (185 bar) to the contour valve rams to close the contour valve, the contour valve closing isolation valve (9) should be open (in the vertical position). To lock pressure applied to the contour valve closing, and to isolate it from the back system, the contour valve closing isolation valve (9) should be moved to a horizontal position.

(10) Contour valve closing pressure gauge: The contour valve closing pressure gauge is on the contour valve side of the contour valve closing isolation valve (9). As such, even when the contour valve closing line is isolated from the back system (contour valve closing isolation valve in a horizontal position) pressure in the contour valve rams can always be checked. (11) Contour valve closing line: the contour valve closing line is supplied with pressure via the line exiting this point. (12) Contour valve opening line: in Figure C.8 the contour valve opening line is directly behind the contour valve closing line.

When opening the contour valve, only movement of hydraulic oil is required with very little application of positive pressure. There is no requirement for locking pressure. However, the pressure locking the contour valve rams closed via the contour valve closing isolation valve must be released back to reservoir. To safely set the back system to contour valve opening, note again that the isolation valves (6) and (9) should be closed and any pressure in the back system is returned to the reservoir via the pump and reservoir line (1) ensuring zero pressure in the back system gauge (2). Then the selector (3) should be moved to the up position (contour valve selection) and the lever handle (4) moved to the down position. Then the contour valve opening isolation valve (9) can be opened to allow displaced oil back to the reservoir via the auxiliary return line (5). Actuating the pump will now open the contour valve. Note pressure does not need to be applied. Confirmation of valve being in the open position can be visually confirmed at the contour valve.

C.3 Maintenance

The maintenance of the shock tube will be driven primarily around cleanliness so as not to contaminate successive experiments. A schedule of cleaning should be provided by the end user based on their experience in shock tube operation and amended as knowledge is gained from initial experimentation. Aside from the cleanliness requirement, the following items should be checked regularly. Suggested times for examination have been provided at a high frequency of examination for the first 6 months of operation to ensure anticipated operation is witnessed and that the rate of deterioration of consumable items (such as O-rings) is identified. The rate at which the items should be checked can be increased as rate of deterioration is learned. While checks are being performed, the quantity of experiments and types of test media should be acknowledged. New test media may have

varying effects on items. Any items that report change in dimensionality or material behavior (hardness of O-rings for example) should be reported immediately to the designers and the main operator and no experiments performed until the designer/the main operator is satisfied–which may include rectification.

REFERENCES

[1] T.N.A.o. Sciences, Fossil Fuels. http://needtoknow.nas.edu/energy/energy-sources/fossil-fuels/.

[2] U.S.E.I. Administration, O.o.E. Analysis, U.S.D.o. Energy, Annual Energy Outlook 2018 with projections to 2050, 2018.

[3] C.F.C.A.E. Solutions, Regulating Power Sector Carbon Emissions. https://www.c2es.org/content/regulating-power-sector-carbon-emissions/.

[4] B. Miller, 8 - Greenhouse gas – carbon dioxide emissions reduction technologies, in: B. Miller (Ed.), Fossil Fuel Emissions Control Technologies, Butterworth-Heinemann2015, pp. 367-438.

[5] E.C.a.E. Protection, Products of Combustion. https://www.e-education.psu.edu/egee102/node/1951.

[6] U.S.E.P. Agency, Inventory of U.S. Greenhouse Gas Emissions and Sinks, 2017.

[7] M.P. Boyce, 1 - Combined cycle power plants, in: A.D. Rao (Ed.), Combined Cycle Systems for Near-Zero Emission Power Generation, Woodhead Publishing2012, pp. 1-43.

[8] J. Miller, 2 - The combined cycle and variations that use HRSGs, in: V.L. Eriksen (Ed.), Heat Recovery Steam Generator Technology, Woodhead Publishing2017, pp. 17-43.

[9] M.J.D. V. Dostal, P. Hejzlar A Supercritical Carbon Dioxide Cycle for Next Generation Nuclear Reactors. http://web.mit.edu/22.33/www/dostal.pdf.

[10] eCourses, Thermodynamics-Theory-Brayton cycle - the Ideal Cycle for Gas-turbine Engine. https://ecourses.ou.edu/cgi-bin/ebook.cgi?doc&topic=th&chap_sec=09.1&page=theory.

[11] C.R. Service, U.S. Carbon Dioxide Emissions in the Electricity Sector: Factors, Trends, and Projections, 2019.

[12] C.C.S. Association, What is CCS? http://www.ccsassociation.org/what-is-ccs/.

[13] S.A. Rackley, 4 - Carbon capture from power generation, in: S.A. Rackley (Ed.), Carbon Capture and Storage (Second Edition), Butterworth-Heinemann, Boston, 2017, pp. 75-101.

[14] S.M. Besarati, D. Goswami, Supercritical CO_2 and other advanced power cycles for concentrating solar thermal (CST) systems, 2017, pp. 157-178.

[15] I.H.B. E.W. Lemmon, M.L. Hubber, M.O. McLinden, NIST Standard Reference Database 23: Reference Fluid Thermodynamic and Transport Properties-REFPROP, National Institute of Standards and Technology, Standard Reference Data Program, Gaithersburg, 2018.

[16] V. Dostál, A supercritical carbon dioxide cycle for next generation nuclear reactors, 2005.

[17] E.T. Dodge, sCO_2 Power Cycles Offer Improved Efficiency Across Power Industry. http://www.edwardtdodge.com/2014/11/20/sco2-power-cycles-offer-improved-efficiency-across-power-industry/.

[18] C. Engineering, Supercritical CO_2: A Green Solvent. https://www.chemengonline.com/supercritical-co2-a-green-solvent/?printmode=1.

[19] C.W. White, N. Weiland, Preliminary Cost and Performance Results for a Natural Gas-Fired Direct sCO_2 Power Plant - Report, ; NETL2018.

[20] N. Weiland, W. Shelton, C.W. White, D. Gray, Performance baseline for direct-fired sCO_2 cycles, 5th International Supercritical CO_2 Power Cycles Symposium, (2016).

[21] N. Weiland, D. Thimsen, A Practical Look at Assumptions and Constraints for Steady State Modeling of sCO_2 Brayton Power Cycles, The 5th International Symposium - Supercritical CO_2 Power Cycles, (2016).

[22] U.S.D.o. Energy, Quadrennial Technology Review 2015 Technology Assessments, 2015.

[23] R.J. Allam, J.E. Fetvedt, B.A. Forrest, D.A. Freed, The Oxy-Fuel, Supercritical CO_2 Allam Cycle: New Cycle Developments to Produce Even Lower-Cost Electricity From Fossil Fuels Without Atmospheric Emissions, doi:10.1115/GT2014-26952(2014) V03BT36A016.

[24] G.P. Smith, D.M. Golden, M. Frenklach, N.W. Moriarty, B. Eiteneer, M. Goldenberg, C.T. Bowman, R.K. Hanson, S. Song, W.C. Gardiner Jr., V.V. Lissianski, Z. Qin, GRI-Mech 3.0. http://www.me.berkeley.edu/gri_mech/.

[25] X.S. X. Yang, J. Santner, H. Zhao, Y. Ju, A high pressure mechanism for H_2, CO, CH_2O, CH_4, CH_3OH, C_2H_2, C_2H_4, C_2H_6 with EGR Effects (CO_2 and H_2O) and HCO prompt reactions. http://engine.princeton.edu/mechanism/HP-Mech.html.

[26] X.Y. H. Wang, A.V. Joshi, S.G. Davis, A. Laskin, F. Egolfopoulos, C.K. Law, High-temperature combustion reaction model of H_2/CO/C_1-C_4 compounds. http://ignis.usc.edu/Mechanisms/USC-Mech%20II/USC_Mech%20II.htm.

[27] Y.T. G.P. Smith, and H. Wang, Foundational fuel chemistry model version 1.0 (FFCM-1). http://nanoenergy.stanford.edu/ffcm1.

[28] A. Kéromnès, W.K. Metcalfe, K.A. Heufer, N. Donohoe, A.K. Das, C.-J. Sung, J. Herzler, C. Naumann, P. Griebel, O. Mathieu, M.C. Krejci, E.L. Petersen, W.J. Pitz, H.J. Curran, An experimental and detailed chemical kinetic modeling study of hydrogen and syngas mixture oxidation at elevated pressures, Combustion and Flame 160 (2013) 995-1011.

[29] W.K. Metcalfe, S.M. Burke, S.S. Ahmed, H.J. Curran, A Hierarchical and Comparative Kinetic Modeling Study of C_1−C_2 Hydrocarbon and Oxygenated Fuels, International Journal of Chemical Kinetics 45 (2013) 638-675.

[30] Y. Li, C.-W. Zhou, K.P. Somers, K. Zhang, H.J. Curran, The oxidation of 2-butene: A high pressure ignition delay, kinetic modeling study and reactivity comparison with isobutene and 1-butene, Proceedings of the Combustion Institute 36 (2017) 403-411.

[31] C.-W. Zhou, Y. Li, E. O'Connor, K.P. Somers, S. Thion, C. Keesee, O. Mathieu, E.L. Petersen, T.A. DeVerter, M.A. Oehlschlaeger, G. Kukkadapu, C.-J. Sung, M. Alrefae, F. Khaled, A. Farooq, P. Dirrenberger, P.-A. Glaude, F. Battin-Leclerc, J. Santner, Y. Ju, T. Held, F.M. Haas, F.L. Dryer, H.J. Curran, A comprehensive experimental and modeling study of isobutene oxidation, Combustion and Flame 167 (2016) 353-379.

[32] U. Burke, W.K. Metcalfe, S.M. Burke, K.A. Heufer, P. Dagaut, H.J. Curran, A detailed chemical kinetic modeling, ignition delay time and jet-stirred reactor study of methanol oxidation, Combustion and Flame 165 (2016) 125-136.

[33] S.M. Burke, U. Burke, R. Mc Donagh, O. Mathieu, I. Osorio, C. Keesee, A. Morones, E.L. Petersen, W. Wang, T.A. DeVerter, M.A. Oehlschlaeger, B. Rhodes, R.K. Hanson, D.F. Davidson, B.W. Weber, C.-J. Sung, J. Santner, Y. Ju, F.M. Haas, F.L. Dryer, E.N. Volkov, E.J.K. Nilsson, A.A. Konnov, M. Alrefae, F. Khaled, A. Farooq, P. Dirrenberger, P.-A. Glaude, F. Battin-Leclerc, H.J. Curran, An experimental and modeling study of propene oxidation. Part 2: Ignition delay time and flame speed measurements, Combustion and Flame 162 (2015) 296-314.

[34] S.M. Burke, W. Metcalfe, O. Herbinet, F. Battin-Leclerc, F.M. Haas, J. Santner, F.L. Dryer, H.J. Curran, An experimental and modeling study of propene oxidation. Part 1: Speciation measurements in jet-stirred and flow reactors, Combustion and Flame 161 (2014) 2765-2784.

[35] S. Gudiyella, K. Brezinsky, The high pressure study of n-propylbenzene pyrolysis, Proceedings of the Combustion Institute 34 (2013) 1767-1774.

[36] W. Wang, S. Gowdagiri, M.A. Oehlschlaeger, The high-temperature autoignition of biodiesels and biodiesel components, Combustion and Flame 161 (2014) 3014-3021.

[37] S. Park, O. Mannaa, F. Khaled, R. Bougacha, M.S. Mansour, A. Farooq, S.H. Chung, S.M. Sarathy, A comprehensive experimental and modeling study of 2-methylbutanol combustion, Combustion and Flame 162 (2015) 2166-2176.

[38] M.V. Johnson, S.S. Goldsborough, Z. Serinyel, P. O'Toole, E. Larkin, G. O'Malley, H.J. Curran, A Shock Tube Study of n- and iso-Propanol Ignition, Energy & Fuels 23 (2009) 5886-5898.

[39] Y. Uygun, S. Ishihara, H. Olivier, A high pressure ignition delay time study of 2-methylfuran and tetrahydrofuran in shock tubes, Combustion and Flame 161 (2014) 2519-2530.

[40] W. Ren, D.F. Davidson, R.K. Hanson, IR laser absorption diagnostic for C_2H_4 in shock tube kinetics studies, International Journal of Chemical Kinetics 44 (2012) 423-432.

[41] S. Li, Y. Zhu, D.F. Davidson, R.K. Hanson, Pyrolysis study of conventional and alternative fuels behind reflected shock waves, Fuel 132 (2014) 170-177.

[42] A. Fridlyand, P.T. Lynch, R.S. Tranter, K. Brezinsky, Single Pulse Shock Tube Study of Allyl Radical Recombination, The Journal of Physical Chemistry A 117 (2013) 4762-4776.

[43] A. Lifshitz, K. Scheller, A. Burcat, G.B. Skinner, Shock-tube investigation of ignition in methane-oxygen-argon mixtures, Combustion and Flame 16 (1971) 311-321.

[44] R.M.R. Higgin, A. Williams, A shock-tube investigation of the ignition of lean methane and n-butane mixtures with oxygen, Symposium (International) on Combustion 12 (1969) 579-590.

[45] S. Jouzdani, M.A. Eldeeb, L. Zhang, B. Akih-Kumgeh, High-Temperature Study of 2-Methyl Furan and 2-Methyl Tetrahydrofuran Combustion, International Journal of Chemical Kinetics 48 (2016) 491-503.

[46] E.L. Petersen., M. Röhrig., D.F. Davidson., R.K. Hanson., C. T.Bowman., High-pressure methane oxidation behind reflected shock waves, Symposium (International) on Combustion 26 (1996) 799-806.

[47] G.B. Skinner, R.A. Ruehrwein, Shock Tube studies on the Pyrolysis and Oxidation of Methane, The Journal of Physical Chemistry 63 (1959) 1736-1742.

[48] T. Asaba, K. Yoneda, N. Kakihara, T. Hikita, A shock tube study of ignition of methane-oxygen mixtures, Symposium (International) on Combustion 9 (1963) 193-200.

[49] H. Miyama, T. Takeyama, Mechanism of Methane Oxidation in Shock Waves, The Journal of Chemical Physics 40 (1964) 2049-2050.

[50] D.J. Seery, C.T. Bowman, An experimental and analytical study of methane oxidation behind shock waves, Combustion and Flame 14 (1970) 37-47.

[51] A. Grillo, M.W. Slack, Shock tube study of ignition delay times in methane-oxygen-nitrogen-argon mixtures, Combustion and Flame 27 (1976) 377-381.

[52] R. Zellner, K.J. Niemilz, J. Warnatz, W.C. Gardiner, C.S. Eubank, J.M. Simmie, Hydrocarbon Induced Acceleration of Ignition of Methane-Air Ignition, Flames, Lasers and Reactive Systems, American Institute of Aeronautics and Astronautics1983, pp. 252-272.

[53] C. Treviño, F. Méndez, Reduced kinetic mechanism for methane ignition, Symposium (International) on Combustion 24 (1992) 121-127.

[54] L.J. Spadaccini, M.B. Colket, Ignition delay characteristics of methane fuels, Progress in Energy and Combustion Science 20 (1994) 431-460.

[55] V.I. Golovitchev, M.L. Pilia, C. Bruno, Autoignition of methane mixtures - The effect of hydrogen peroxide, Journal of Propulsion and Power 12 (1996) 699-707.

[56] M. Frenklach, H. Wang, M.J. Rabinowitz, Optimization and analysis of large chemical kinetic mechanisms using the solution mapping method—combustion of methane, Progress in Energy and Combustion Science 18 (1992) 47-73.

[57] T. Tsuboi, H.G. Wagner, Homogeneous thermal oxidation of methane in reflected shock waves, Symposium (International) on Combustion 15 (1975) 883-890.

[58] J. Huang, P.G. Hill, W.K. Bushe, S.R. Munshi, Shock-tube study of methane ignition under engine-relevant conditions: experiments and modeling, Combustion and Flame 136 (2004) 25-42.

[59] U. Burke, K.P. Somers, P. O'Toole, C.M. Zinner, N. Marquet, G. Bourque, E.L. Petersen, W.K. Metcalfe, Z. Serinyel, H.J. Curran, An ignition delay and kinetic modeling study of methane, dimethyl ether, and their mixtures at high pressures, Combustion and Flame 162 (2015) 315-330.

[60] H. El Merhubi, A. Kéromnès, G. Catalano, B. Lefort, L. Le Moyne, A high pressure experimental and numerical study of methane ignition, Fuel 177 (2016) 164-172.

[61] H. Hashemi, J.M. Christensen, S. Gersen, H. Levinsky, S.J. Klippenstein, P. Glarborg, High-pressure oxidation of methane, Combustion and Flame 172 (2016) 349-364.

[62] E.L. Petersen, D.F. Davidson, R.K. Hanson, Kinetics modeling of shock-induced ignition in low-dilution CH_4/O_2 mixtures at high pressures and intermediate temperatures, Combustion and Flame 117 (1999) 272-290.

[63] H.W. M. Frenklach, C.-L. Yu, M. Goldenberg, C.T. Bowman, R.K. Hanson, D.F. Davidson, E.J. Chang, G.P. Smith, D.M. Golden, W.C. Gardiner and V. Lissianski, An optimized detailed chemical reaction mechanism for methane combustion, Report No. GRI-95/0058,

[64] V.P. Zhukov, V.A. Sechenov, A.Y. Starikovskii, Spontaneous Ignition of Methane–Air Mixtures in a Wide Range of Pressures, Combustion, Explosion and Shock Waves 39 (2003) 487-495.

[65] O. Pryor, S. Barak, B. Koroglu, E. Ninnemann, S.S. Vasu, Measurements and interpretation of shock tube ignition delay times in highly CO_2 diluted mixtures using multiple diagnostics, Combustion and Flame 180 (2017) 63-76.

[66] O. Pryor, S. Barak, J. Lopez, E. Ninnemann, B. Koroglu, L. Nash, S. Vasu, High Pressure Shock Tube Ignition Delay Time Measurements During Oxy-Methane Combustion With High Levels of CO_2 Dilution, Journal of Energy Resources Technology 139 (2017) 042208-042208-042206.

[67] W. Zeng, H. Ma, Y. Liang, E. Hu, Experimental and modeling study on effects of N_2 and CO_2 on ignition characteristics of methane/air mixture, Journal of Advanced Research 6 (2015) 189-201.

[68] B. Koroglu, O.M. Pryor, J. Lopez, L. Nash, S.S. Vasu, Shock tube ignition delay times and methane time-histories measurements during excess CO_2 diluted oxy-methane combustion, Combustion and Flame 164 (2016) 152-163.

[69] J.W. Hargis, E.L. Petersen, Methane Ignition in a Shock Tube with High Levels of CO_2 Dilution: Consideration of the Reflected-Shock Bifurcation, Energy & Fuels 29 (2015) 7712-7726.

[70] J. Shao, R. Choudhary, D.F. Davidson, R.K. Hanson, S. Barak, S. Vasu, Ignition delay times of methane and hydrogen highly diluted in carbon dioxide at high pressures up to 300 atm, Proceedings of the Combustion Institute 37 (2019) 4555-4562.

[71] K.G.P. Sulzmann, B.F. Myers, E.R. Bartle, CO Oxidation. I. Induction Period Preceding CO_2 Formation in Shock-Heated CO–O_2–Ar Mixtures, The Journal of Chemical Physics 42 (1965) 3969-3979.

[72] B.F. Myers, K.G.P. Sulzmann, E.R. Bartle, Oxidation of CO. II. Influence of H_2 on the Induction Period Preceding Rapid CO_2 Formation in Shock-Heated CO–O_2–Ar Mixtures, The Journal of Chemical Physics 43 (1965) 1220-1228.

[73] W.C. Gardiner, M. McFarland, K. Morinaga, T. Takeyama, B.F. Walker, Initiation rate for shock-heated hydrogen-oxygen-carbon monoxide-argon mixtures as determined by OH induction time measurements, The Journal of Physical Chemistry 75 (1971) 1504-1509.

[74] A.M. Dean, D.C. Steiner, E.E. Wang, A shock tube study of the $H_2/O_2/CO/Ar$ and $H_2/N_2O/CO/Ar$ Systems: Measurement of the rate constant for $H + N_2O = N_2 + OH$, Combustion and Flame 32 (1978) 73-83.

[75] D.M. Kalitan, J.D. Mertens, M.W. Crofton, E.L. Petersen, Ignition and Oxidation of Lean CO/H_2 Fuel Blends in Air, Journal of Propulsion and Power 23 (2007) 1291-1301.

[76] S.G. Davis, A.V. Joshi, H. Wang, F. Egolfopoulos, An optimized kinetic model of H_2/CO combustion, Proceedings of the Combustion Institute 30 (2005) 1283-1292.

[77] P. Saxena, F.A. Williams, Testing a small detailed chemical-kinetic mechanism for the combustion of hydrogen and carbon monoxide, Combustion and Flame 145 (2006) 316-323.

[78] J. Li, Z. Zhao, A. Kazakov, M. Chaos, F.L. Dryer, J.J. Scire Jr., A comprehensive kinetic mechanism for CO, CH_2O, and CH_3OH combustion, International Journal of Chemical Kinetics 39 (2007) 109-136.

[79] H. Sun, S.I. Yang, G. Jomaas, C.K. Law, High-pressure laminar flame speeds and kinetic modeling of carbon monoxide/hydrogen combustion, Proceedings of the Combustion Institute 31 (2007) 439-446.

[80] J. Herzler, C. Naumann, Shock Tube Study of the Ignition of Lean CO/H_2 Fuel Blends at Intermediate Temperatures and High Pressure, Combustion Science and Technology 180 (2008) 2015-2028.

[81] K.J. Hughes, Turanyi, T., and Pilling, M.J, The Leeds Methane Oxidation Mechanism Version 1.5. http://www.chem.leeds.ac.uk/.

[82] A.B. Mansfield, M.S. Wooldridge, High-pressure low-temperature ignition behavior of syngas mixtures, Combustion and Flame 161 (2014) 2242-2251.

[83] L.D. Thi, Y. Zhang, Z. Huang, Shock tube study on ignition delay of multi-component syngas mixtures – Effect of equivalence ratio, International Journal of Hydrogen Energy 39 (2014) 6034-6043.

[84] S.M. Walton, X. He, B.T. Zigler, M.S. Wooldridge, An experimental investigation of the ignition properties of hydrogen and carbon monoxide mixtures for syngas turbine applications, Proceedings of the Combustion Institute 31 (2007) 3147-3154.

[85] O. Mathieu, M.M. Kopp, E.L. Petersen, Shock-tube study of the ignition of multi-component syngas mixtures with and without ammonia impurities, Proceedings of the Combustion Institute 34 (2013) 3211-3218.

[86] N. Donohoe, K.A. Heufer, C.J. Aul, E.L. Petersen, G. Bourque, R. Gordon, H.J. Curran, Influence of steam dilution on the ignition of hydrogen, syngas and natural gas blends at elevated pressures, Combustion and Flame 162 (2015) 1126-1135.

[87] M.C. Krejci, O. Mathieu, A.J. Vissotski, S. Ravi, T.G. Sikes, E.L. Petersen, A. Keromnes, W. Metcalfe, H.J. Curran, Laminar Flame Speed and Ignition Delay Time Data for the Kinetic Modeling of Hydrogen and Syngas Fuel Blends, doi:10.1115/GT2012-69290(2012) 931-948.

[88] G. Mittal, C.-J. Sung, R.A. Yetter, Autoignition of H_2/CO at elevated pressures in a rapid compression machine, International Journal of Chemical Kinetics 38 (2006) 516-529.

[89] R. Sivaramakrishnan, A. Comandini, R.S. Tranter, K. Brezinsky, S.G. Davis, H. Wang, Combustion of CO/H_2 mixtures at elevated pressures, Proceedings of the Combustion Institute 31 (2007) 429-437.

[90] A.M. Starik, N.S. Titova, A.S. Sharipov, V.E. Kozlov, Syngas Oxidation Mechanism, Combustion, Explosion, and Shock Waves 46 (2010) 491-506.

[91] A. Frassoldati, T. Faravelli, E. Ranzi, The ignition, combustion and flame structure of carbon monoxide/hydrogen mixtures. Note 1: Detailed kinetic modeling of syngas combustion also in presence of nitrogen compounds, International Journal of Hydrogen Energy 32 (2007) 3471-3485.

[92] D.E. Cavaliere, M.d. Joannon, P. Sabia, M. Sirignano, A. D'Anna, A Comprehensive Kinetic Modeling of Ignition of Syngas–Air Mixtures at Low Temperatures and High Pressures, Combustion Science and Technology 182 (2010) 692-701.

[93] M. Chaos, F.L. Dryer, Syngas Combustion Kinetics and Applications, Combustion Science and Technology 180 (2008) 1053-1096.

[94] U. Maas, J. Warnatz, Ignition processes in carbon-monoxide-hydrogen-oxygen mixtures, Symposium (International) on Combustion 22 (1989) 1695-1704.

[95] F.L. Dryer, M. Chaos, Ignition of syngas/air and hydrogen/air mixtures at low temperatures and high pressures: Experimental data interpretation and kinetic modeling implications, Combustion and Flame 152 (2008) 293-299.

[96] E.L. Petersen, D.M. Kalitan, A.B. Barrett, S.C. Reehal, J.D. Mertens, D.J. Beerer, R.L. Hack, V.G. McDonell, New syngas/air ignition data at lower temperature and elevated pressure and comparison to current kinetics models, Combustion and Flame 149 (2007) 244-247.

[97] M.P. Burke, M. Chaos, Y. Ju, F.L. Dryer, S.J. Klippenstein, Comprehensive H_2/O_2 kinetic model for high-pressure combustion, International Journal of Chemical Kinetics 44 (2012) 444-474.

[98] Z. Hong, D.F. Davidson, R.K. Hanson, An improved H_2/O_2 mechanism based on recent shock tube/laser absorption measurements, Combustion and Flame 158 (2011) 633-644.

[99] A.A. Konnov, Remaining uncertainties in the kinetic mechanism of hydrogen combustion, Combustion and Flame 152 (2008) 507-528.

[100] M. Ó Conaire, H.J. Curran, J.M. Simmie, W.J. Pitz, C.K. Westbrook, A comprehensive modeling study of hydrogen oxidation, International Journal of Chemical Kinetics 36 (2004) 603-622.

[101] D. Lee, S. Hochgreb, Hydrogen autoignition at pressures above the second explosion limit (0.6–4.0 MPa), International Journal of Chemical Kinetics 30 (1998) 385-406.

[102] E. Hu, L. Pan, Z. Gao, X. Lu, X. Meng, Z. Huang, Shock tube study on ignition delay of hydrogen and evaluation of various kinetic models, International Journal of Hydrogen Energy 41 (2016) 13261-13280.

[103] M. Chaos, F.L. Dryer, Chemical-kinetic modeling of ignition delay: Considerations in interpreting shock tube data, International Journal of Chemical Kinetics 42 (2010) 143-150.

[104] G.A. Pang, D.F. Davidson, R.K. Hanson, Experimental study and modeling of shock tube ignition delay times for hydrogen–oxygen–argon mixtures at low temperatures, Proceedings of the Combustion Institute 32 (2009) 181-188.

[105] M.W. Slack, Rate coefficient for $H + O_2 + M = HO_2 + M$ evaluated from shock tube measurements of induction times, Combustion and Flame 28 (1977) 241-249.

[106] D.F. Davidson, E.L. Petersen, M. Röhrig, R.K. Hanson, C.T. Bowman, Measurement of the rate coefficient of $H+O_2+M \rightarrow HO_2+M$ for M=Ar and N_2 at high pressures, Symposium (International) on Combustion 26 (1996) 481-488.

[107] M.A. Mueller, R.A. Yetter, F.L. Dryer, Measurement of the rate constant for $H+O_2+M \rightarrow HO_2+M$ (M=N_2, Ar) using kinetic modeling of the high-pressure $H_2/O_2/NO_x$ reaction, Symposium (International) on Combustion 27 (1998) 177-184.

[108] J. Troe, Detailed modeling of the temperature and pressure dependence of the reaction $H+O_2$ (+M)$\rightarrow HO_2$ (+M), Proceedings of the Combustion Institute 28 (2000) 1463-1469.

[109] R.X. Fernandes, K. Luther, J. Troe, V.G. Ushakov, Experimental and modelling study of the recombination reaction $H + O_2$ (+M) $\rightarrow HO_2$ (+M) between 300 and 900 K, 1.5 and 950 bar, and in the bath gases M = He, Ar, and N_2, Physical Chemistry Chemical Physics 10 (2008) 4313-4321.

[110] P.J. Ashman, B.S. Haynes, Rate coefficient of $H+O_2+M \rightarrow HO_2+M$ (M=H_2O, N_2, Ar, CO_2), Symposium (International) on Combustion 27 (1998) 185-191.

[111] R.W. Bates, D.M. Golden, R.K. Hanson, C.T. Bowman, Experimental study and modeling of the reaction $H + O_2 + M \rightarrow HO_2 + M$ (M = Ar, N_2 , H_2O) at elevated pressures and temperatures between 1050 and 1250 K, Physical Chemistry Chemical Physics 3 (2001) 2337-2342.

[112] J.V. Michael, M.C. Su, J.W. Sutherland, J.J. Carroll, A.F. Wagner, Rate Constants For $H + O_2 + M \rightarrow HO_2 + M$ in Seven Bath Gases, The Journal of Physical Chemistry A 106 (2002) 5297-5313.

[113] S.S. Vasu, D.F. Davidson, R.K. Hanson, Shock Tube Study of Syngas Ignition in Rich CO_2 Mixtures and Determination of the Rate of $H + O_2 + CO_2 \rightarrow HO_2 + CO_2$, Energy & Fuels 25 (2011) 990-997.

[114] S. Barak, O. Pryor, J. Lopez, E. Ninnemann, S. Vasu, B. Koroglu, High-Speed Imaging and Measurements of Ignition Delay Times in Oxy-Syngas Mixtures With High CO_2 Dilution in a Shock Tube, Journal of Engineering for Gas Turbines and Power 139 (2017).

[115] M.F. Campbell, A.M. Tulgestke, D.F. Davidson, R.K. Hanson, A second-generation constrained reaction volume shock tube, Review of Scientific Instruments 85 (2014) 055108.

[116] D.F. Davidson, R.K. Hanson, Recent advances in shock tube/laser diagnostic methods for improved chemical kinetics measurements, Shock Waves 19 (2009) 271-283.

[117] D.F. Davidson, R.K. Hanson, Interpreting shock tube ignition data, International Journal of Chemical Kinetics 36 (2004) 510-523.

[118] A. Lifshitz, S.H. Bauer, E.L.R. Jr., Studies with a Single-Pulse Shock Tube. I. The Cis—Trans Isomerization of Butene-2, The Journal of Chemical Physics 38 (1963) 2056-2063.

[119] R.S. Tranter, K. Brezinsky, D. Fulle, Design of a high-pressure single pulse shock tube for chemical kinetic investigations, Review of Scientific Instruments 72 (2001) 3046-3054.

[120] R.S. Tranter, R. Sivaramakrishnan, K. Brezinsky, M.D. Allendorf, High pressure, high temperature shock tube studies of ethane pyrolysis and oxidation, Physical Chemistry Chemical Physics 4 (2002) 2001-2010.

[121] R.A. Alpher, D.R. White, Flow in shock tubes with area change at the diaphragm section, Journal of Fluid Mechanics 3 (1958) 457-470.

[122] A. Bar-Nun, A. Lifshitz, Kinetics of the Homogeneous Exchange Reaction: $^{14-}{}^{14}N_2+{}^{15-}{}^{15}N_2 \leftrightharpoons {}^{214-}{}^{15}N_2$. Single-Pulse Shock-Tube Studies, The Journal of Chemical Physics 47 (1967) 2878-2888.

[123] Z. Hong, G.A. Pang, S.S. Vasu, D.F. Davidson, R.K. Hanson, The use of driver inserts to reduce non-ideal pressure variations behind reflected shock waves, Shock Waves 19 (2009) 113-123.

[124] E.-S. Lee, C. Park, K.-S. Chang, Shock-Tube Determination of CN Formation Rate in a CO-N_2 Mixture, Journal of Thermophysics and Heat Transfer 21 (2007) 50-56.

[125] E.L. Petersen, R.K. Hanson, Measurement of Reflected-shock Bifurcation Over a Wide Range of Gas Composition and Pressure, Shock Waves 15 (2006) 333-340.

[126] E.L. Petersen, M.J.A. Rickard, M.W. Crofton, E.D. Abbey, M.J. Traum, D.M. Kalitan, A facility for gas- and condensed-phase measurements behind shock waves, Measurement Science and Technology 16 (2005) 1716-1729.

[127] I. Stotz, G. Lamanna, H. Hettrich, B. Weigand, J. Steelant, Design of a double diaphragm shock tube for fluid disintegration studies, Review of Scientific Instruments 79 (2008) 125106.

[128] R.K. Hanson, D.F. Davidson, Recent advances in laser absorption and shock tube methods for studies of combustion chemistry, Progress in Energy and Combustion Science 44 (2014) 103-114.

[129] R. Bonazza., Wisconsin Shock Tube Laboratory (WiSTL). http://silver.neep.wisc.edu/~shock/.

[130] MATLAB.

[131] J.E.A. John., T.G. Keith., Gas Dynamics, Pearson Prentice Hall2006.

[132] Kistler 6045A. https://www.kistler.com/en/product/type-6045a/.

[133] Kistler 603CAA. https://www.kistler.com/en/product/type-603caa/.

[134] PCB 113B22. http://www.pcb.com/Products.aspx?m=113B22.

[135] D.F. Davidson, R.K. Hanson, Fundamental Kinetics Database Utilizing Shock Tube Measurements 2014.

[136] E.L. Petersen, A Shock Tube and Diagnostics for Chemistry Measurement at Elevated Pressures with Application to Methane Ignition, Mechanical Engineering, Stanford, 1998.

[137] D.F. Davidson, R.K. Hanson, Real Gas Corrections in Shock Tube Studies at High Pressures, Israel Journal of Chemistry 36 (1996) 321-326.

[138] E.L. Petersen, R.K. Hanson, Nonideal effects behind reflected shock waves in a high-pressure shock tube, Shock Waves 10 (2001) 405-420.

[139] J.W. Hargis, E.L. Petersen, Shock-Tube Boundary-Layer Effects on Reflected-Shock Conditions with and Without CO_2, AIAA Journal 55 (2017) 902-912.

[140] C.-P. 15131, Reaction Design, San Diego, 2013.

[141] J.M. Hall, E.L. Petersen, An optimized kinetics model for OH chemiluminescence at high temperatures and atmospheric pressures, International Journal of Chemical Kinetics 38 (2006) 714-724.

[142] J.M. Hall, M.J.A. Rickard, E.L. Petersen, Comparison of characteristic time diagnostics for ignition and oxidation of fuel/oxidizer mixtures behind reflected shock waves, Combustion Science and Technology 177 (2005) 455-483.

[143] J. de Vries, J.M. Hall, S.L. Simmons, M.J.A. Rickard, D.M. Kalitan, E.L. Petersen, Ethane ignition and oxidation behind reflected shock waves, Combustion and Flame 150 (2007) 137-150.

[144] E.L. Petersen, J.M. Hall, S.D. Smith, J. de Vries, A.R. Amadio, M.W. Crofton, Ignition of Lean Methane-Based Fuel Blends at Gas Turbine Pressures, Journal of Engineering for Gas Turbines and Power 129 (2007) 937-944.

[145] E.L. Petersen, Interpreting Endwall and Sidewall Measurements in Shock-Tube Ignition Studies, Combustion Science and Technology 181 (2009) 1123-1144.

[146] K.P. Grogan, M. Ihme, Weak and strong ignition of hydrogen/oxygen mixtures in shock-tube systems, Proceedings of the Combustion Institute 35 (2015) 2181-2189.

[147] H. Yamashita, J. Kasahara, Y. Sugiyama, A. Matsuo, Visualization study of ignition modes behind bifurcated-reflected shock waves, Combustion and Flame 159 (2012) 2954-2966.

[148] N. Donohoe, A. Heufer, W.K. Metcalfe, H.J. Curran, M.L. Davis, O. Mathieu, D. Plichta, A. Morones, E.L. Petersen, F. Güthe, Ignition delay times, laminar flame speeds, and mechanism validation for natural gas/hydrogen blends at elevated pressures, Combustion and Flame 161 (2014) 1432-1443.

[149] M. Karimi, B. Ochs, Z. Liu, D. Ranjan, W. Sun, Measurement of methane autoignition delays in carbon dioxide and argon diluents at high pressure conditions, Combustion and Flame 204 (2019) 304-319.

[150] G. Kogekar, C. Karakaya, G.J. Liskovich, M.A. Oehlschlaeger, S.C. DeCaluwe, R.J. Kee, Impact of non-ideal behavior on ignition delay and chemical kinetics in high-pressure shock tube reactors, Combustion and Flame 189 (2018) 1-11.

[151] O. Redlich, J.N.S. Kwong, On the Thermodynamics of Solutions. V. An Equation of State. Fugacities of Gaseous Solutions, Chemical Reviews 44 (1949) 233-244.

[152] D.G. Goodwin, H.K.M., R.L. Speth, Cantera: An object- oriented software toolkit for chemical kinetics, thermodynamics, and transport processes. https://cantera.org/.

[153] X. Gao, S. Yang, W. Sun, A global pathway selection algorithm for the reduction of detailed chemical kinetic mechanisms, Combustion and Flame 167 (2016) 238-247.

[154] H. Wang, 2017.